ISSN 0021-3438 (Print)
ISSN 2412-8783 (Online)

IZVESTIYA

NON-FERROUS METALLURGY

Vol. 29, No. 4, 2023

Scientific and Technical Journal
Founded in 1958
6 Issues per year

ИЗВЕСТИЯ ВУЗОВ

ЦВЕТНАЯ МЕТАЛЛУРГИЯ

Том 29, № 4, 2023

Научно-технический журнал
Основан в 1958 г.
Выходит 6 раз в год

ISSN 0021-3438 (Print)
ISSN 2412-8783 (Online)

IZVESTIYA NON-FERROUS METALLURGY

Vol. 29, No. 4
2023

Scientific and Technical Journal Founded in 1958 6 Issues per year http://cvmet.misis.ru

Journal is included into the List of the peer-reviewed scientific publications recommended by the Highest Attestation Commission of the Ministry of Education and Science of the Russian Federation for publishing the results of doctoral and candidate dissertations

Abstracting/Indexing: Russian Science Citation Index (RSCI), Chemical Abstracts (Online), INIS, OCLC ArticleFirst, Ulrich's Periodicals Directory, VINITI Database (Abstract Journal)

Founder

National University of Science and Technology "MISIS"
Address: 4 build. 1 Leninskiy Prosp., Moscow 119049, Russia
http://www.misis.ru

Editorial Staff

Address: NUST MISIS, 4 build. 1 Leninskiy Prosp., Moscow 119049, Russia
Phone: +7 (495) 638-45-35
E-mail: izv.vuz@misis.ru

Leading Editor – O.V. Sosnina
Executive Editor – A.A. Kudinova
Layout Designer – E.A. Legkaya

Certificate of registration No. 015842 (13.03.1997)
Re-registration PI No. ФС77-79229 (25.09.2020)

Signed print 21.08.2023. Format 60×90 1/8.
Offset paper No. 1. Digital printing. Quires 10.75
Order 17948. Free price

Subscription: Ural-Press Agency

Printed in the printing house of the MISIS Publish House
4 build. 1 Leninskiy Prosp., Moscow 119049, Russia. Phone/fax: +7 (499) 236-76-17

ISSN 0021-3438 (Print)
ISSN 2412-8783 (Online)

ИЗВЕСТИЯ ВУЗОВ
ЦВЕТНАЯ МЕТАЛЛУРГИЯ

Том 29, № 4
2023

Научно-технический журнал Основан в 1958 г. Выходит 6 раз в год http://cvmet.misis.ru

Журнал включен в Перечень рецензируемых научных изданий, рекомендованных ВАК Минобрнауки РФ для публикации результатов диссертаций на соискание ученых степеней

Журнал включен в базы данных: Russian Science Citation Index (RSCI), Chemical Abstracts (Online), INIS, OCLC ArticleFirst, Ulrich's Periodicals Directory, РИНЦ, БД/РЖ ВИНИТИ

Учредитель

ФГАОУ ВО Национальный исследовательский технологический университет «МИСИС»
Адрес: 119049, г. Москва, Ленинский пр-т, 4, стр. 1
http://www.misis.ru

Редакция журнала

Адрес: 119049, г. Москва, Ленинский пр-т, 4, стр. 1, НИТУ МИСИС
Тел.: +7 (495) 638-45-35
E-mail: izv.vuz@misis.ru

Свидетельство о регистрации № 015842 от 13.03.1997 г.
Перерегистрация ПИ № ФС77-79229 от 25.09.2020 г.

Подписка: Агентство «Урал-пресс»

Ведущий редактор – О.В. Соснина
Выпускающий редактор – А.А. Кудинова
Дизайн и верстка – Е.А. Легкая

Подписано в печать 21.08.2023. Формат 60×90 1/8.
Бум. офсетная № 1. Печать цифровая. Усл. печ. л. 10,75
Заказ 17948. Цена свободная

Отпечатано в типографии Издательского Дома МИСИС
119049, г. Москва, Ленинский пр-т, 4, стр. 1. Тел./факс: +7 (499) 236-76-17

CONTENTS

СОДЕРЖАНИЕ

Foundry

Литейное производство

Pressure treatment of metals

Обработка металлов давлением

Physical metallurgy and heat treatment

Металловедение и термическая обработка

FOUNDRY / ЛИТЕЙНОЕ ПРОИЗВОДСТВО

UDC 621.74
https://doi.org/10.17073/0021-3438-2023-4-5-14

Research article
Научная статья

Consumable additive FDM models in the production of aluminum alloy castings

M.S. Varfolomeev, I.A. Petrov

Moscow Aviation Institute (National Research University)
4 Volokolamskoe shosse, Moscow 125993, Russia

✉ Maksim S. Varfolomeev (varfolom2a@yandex.ru, varfolom2a@rambler.ru)

Abstract: This article describes the results of a study aimed at improving production technology of experimental castings from aluminum alloys by investment casting using models produced by 3D printing. The consumable models were produced using fused deposition modeling (FDM). Biodegradable polylactide (PLA) was used as a material for the models. In order to decrease the surface roughness of consumable PLA model. chemical post-treatment by dichloromethane needs to be performed. After immersion of the model into the solvent for 10s, its surface becomes smooth and glossy. Three-point static bending tests of PLA plates demonstrated a mechanical strength of average ~45.1 MPa. A thermomechanical analysis of polylactide demonstrated that in the course of heating of ceramic shell in excess of 150 °C, the polylactide model begins to expand intensively by exerting significant pressure on the ceramic shell. In order to decrease stress during the removal of polylactide model from ceramic mold, the heating time in the range of 150–300 °C needs to be heated to a maximum. The use of hollow consumable casting models with a cellular structure not higher than 30 % is also sensible. The stresses on the shell will not exceed its strength. Characteristic temperature properties of PLA plastic thermal destruction were detected using thermogravimetric analysis. Polylactide was established to completely burn out upon heating to 500 °C leaving no ash residue. Analysis of the results identified the burning modes of polylactide models from ceramic molds. Using a Picaso 3D Designer printer (Russia), the PLA models were printed used for production of experimental castings from aluminum alloys. It was revealed that the surface roughness (R_a) of a casting produced using a consumable model treated by dichloromethane decreases by 81.75 %: from 13.7 to 2.5 μm.

Keywords: investment casting, polylactide, 3D printing, fused deposition modeling (FDM), aluminum alloys, surface roughness.

For citation: Varfolomeev M.S., Petrov I.A. Consumable additive FDM models in the production of aluminum alloy castings. *Izvestiya. Non-Ferrous Metallurgy*. 2023;29(4):5–14. https://doi.org/10.17073/0021-3438-2023-4-5-14

Особенности изготовления отливок из алюминиевых сплавов по выжигаемым аддитивным FDM-моделям

М.С. Варфоломеев, И.А. Петров

Московский авиационный институт (Национальный исследовательский университет)
125993, Россия, г. Москва, Волоколамское шоссе, 4

✉ Максим Сергеевич Варфоломеев (varfolom2a@yandex.ru, varfolom2a@rambler.ru)

Аннотация: Приведены результаты исследований, направленные на совершенствование литейной технологии получения опытно-экспериментальных отливок из алюминиевых сплавов методом литья по выжигаемым моделям, изготовленным с применением 3D-печати. Для создания выжигаемых моделей использовали метод осаждения расплавленной нити (FDM – fused

deposition modeling), а в качестве материала моделей был выбран биоразлагаемый материал – полилактид (PLA – polylactide). Установлено, что для уменьшения шероховатости выжигаемой PLA-модели необходимо проводить химическую постобработку ее поверхности дихлорметаном. В результате окунания модели в растворитель на 10 с она приобретает гладкую и глянцевую поверхность. Испытания механической прочности PLA-пластин на трехточечный статический изгиб показали, что данный показатель составляет в среднем ~ 45,1 МПа. Термомеханический анализ полилактида выявил, что в процессе нагрева керамической оболочки выше 150 °С полилактидная модель начинает интенсивно расширяться, оказывая существенное давление на керамическую оболочку. Для уменьшения напряжений в процессе удаления полилактидной модели из керамической формы необходимо максимально увеличить время нагрева в интервале температур 150–300 °С, а также целесообразно использовать пустотелые выжигаемые модели отливки со степенью заполнения ячеистой структуры не более 30 %. При этом напряжения в оболочке не будут превышать ее прочность. С помощью термогравиметрического анализа выявлены характерные температурные характеристики термодеструкции PLA-пластика. Установлено, что материал из полилактида полностью выгорает при нагреве до температуры 500 °С, не оставляя после себя остатков золы. Анализ результатов позволил определить технологические режимы выжигания полилактидных моделей из керамических форм. На принтере Picaso 3D Designer (Россия) были напечатаны PLA-модели, которые использовали для получения опытно-экспериментальных отливок из алюминиевых сплавов. Выявлено, что шероховатость поверхности (R_a) отливки, полученной по выжигаемой модели, обработанной дихлорметаном, уменьшается на 81,75 % – с 13,7 до 2,5 мкм.

Ключевые слова: литье по выжигаемым моделям, полилактид, 3D-печать, метод осаждения расплавленной нити, алюминиевые сплавы, шероховатость поверхности.

Для цитирования: Варфоломеев М.С., Петров И.А. Особенности изготовления отливок из алюминиевых сплавов по выжигаемым аддитивным FDM-моделям. *Известия вузов. Цветная металлургия*. 2023;29(4):5–14.
https://doi.org/10.17073/0021-3438-2023-4-5-14

Introduction

Investment/lost-wax casting is a traditional technology for the production of high-precision products. This casting method enables the production of parts of the most complex shapes with thin walls and a high surface finish. The quality of investment/lost-wax castings is markedly superior to other casting methods, therefore this method is used in various fields.

The main problem in single and small batch production of products is the high cost of tooling. Traditional ceramic mold making requires the use of a melted/fired model produced in molds. This production process of making a mold is very complicated, and the cost of making such tooling is extremely high. This problem is resolved by integrating modern additive 3D printing methods into foundries [1; 2]. It is a relatively new production technology intensively developed and applied in various fields, including foundries [3—5]. The direct development of lost-wax models is not only cost-effective for small-scale and pilot production, but is also capable of creating very complex geometries that would be extremely difficult or too expensive to produce in the traditional way [6].

The process of making a lost-wax model using 3D printing allows the cost and time of casting production to be reduced. It also enabled the production of products of complex geometry in comparison to the conventional investment/lost-wax casting process [7—9]. These advantages are offset by the stepped surface of the model associated with the feature of 3D printing which can negatively affect the surface roughness and dimensional tolerances of castings.

Today, the most affordable and widespread 3D printing method is the technology of Fused Deposition Manufacturing (FDM) [10]. This method is comprised of layer-by-layer application of the molten polymer using an extruder. When compared to other additive manufacturing processes for lost-wax models, such as stereolithography (SLA), direct light processing (DLP), FDM 3D printing is one of the cheapest due to the low price of equipment and consumables, which makes it more widely available [11].

The main materials used in FDM 3D printing are thermoplastics: acrylonitrile butadiene styrene (ABS) [12; 13]; polylactide (PLA) [13,14]; polyamide (PA) [15]; polyethylene terephthalate-glycol (PETG) [16]; polyether ether ketone (PEEK) [17]; polycarbonate (PC) [18] and others.

As an alternative to petroleum-based polymers (ABS, PA, PETG, PEEK, PC), polylactide, a biodegradable biopolymer, is widely applied in numerous industries. PLA is based on starch and polylactic acid, made from completely renewable natural materials.

Polylactide is a fully biodegradable thermoplastic polyester. It is a polymer of lactic acid derived from the processing of corn, starch, cellulose, and sugarcane. The non-toxicity of the material allows the printing process to be carried out even in poorly ventilated areas. The products of thermal degradation of polylactide are con-

sidered harmless, and it burns quite slowly. Due to its environmental friendliness, biocompatibility, biodegradability, renewability, high stiffness and tensile strength, and ease of processing, the use of PLA in the world is growing. In this regard, a number of authors are considering the possibility of using it for the manufacture of burnt models [19—22].

The main goal of the work was to study the technological possibilities of 3D printing for the rapid production of lost-wax models from polylactide with the subsequent production of experimental cast products from aluminum alloys.

Experimental

The lost-wax models were fabricated by the FDM method using polylactide (PLA) as the material of the models. A spool of PLA filament with a diameter of 1.75 mm was supplied by Bestfilament (Russia), a commercial manufacturer of filaments for 3D printing. Pilot lost-wax models of castings and models for mechanical testing were fabricated using a Picaso 3D Designer X printer (Russia) at a cellular structure filling rate of 30 %. A printer nozzle with a diameter of 0.5 mm was used. The thickness of the applied layer was 0.2 mm. The print and platform temperatures during the process were maintained at 200 °C and 75 °C, respectively. Print speed was 20 mm/s. Dichloromethane was used to polish the surface of the PLA models. The casting models were dipped for 5, 10, and 15 s directly into the solvent.

Three-point bending tests of PLA samples with sizes of 40×20×5 mm were performed using an Instron 5982 machine (USA). The traverse speed was 1 mm/min. The distance between supports was 30 mm, and the number of tested samples: 10 pieces.

Ceramic molds were made according to the traditional lost-wax casting technology using layer-by-layer application of a ceramic suspension consisting of an ETS-40 ethyl silicate binder and a filler (pulverized quartz) onto a model block. This was followed by sprinkling each layer with granular quartz with a particle size of 0.2 mm. A total of 5 layers were applied.

The calcination of ceramic experimental molds was carried out in a support filler in an electric resistance furnace at t = 900°C, in an air atmosphere (heating duration 5 h) and exposure for 2 h. The ceramic molds were filled with aluminum alloy AK7ch with the following chemical composition: wt.%: Al — the base; Si — 7.21; Mg — 0.36; Fe — 0.147; Cu — 0.011; Mn — 0.0026. This corresponds to State standard GOST 1583-93.

800 g of the AK7ch alloy was melted in a SNOL-1,6.2,5.1/11-I3 muffle electric furnace. Preliminary degassing of the melt was carried out by purging it with an inert gas (argon).

The melt was modified with a standard 25%NaF + + 62.5%NaCl + 12.5%KCl flux at 740—750 °C. On the surface of the melt, it was applied as an even layer in the amount of 1.5 wt % of the melt. After holding at this temperature for 10 min, the flux was thoroughly kneaded deep into the melt. After 15 min after the melt holding, it was poured at t = 710÷720 °C into calcined ceramic molds heated to 350 °C.

Experimental castings from AK7h alloy were subjected to thermal processing according to State standard GOST 1583-93 under T5 regime (quenching in water at 535±5 °C for 4 h, then aging for 3 h at 415±5 °C).

Thermogravimetric (TGA) and differential thermal (SDTA) analyses were performed using a TGA/SDTA 851 instrument (Mettler Toledo, Switzerland), at a heating rate of 10 °C/min to 1100 °C in an air atmosphere.

Thermomechanical analysis (TMA) of plastic was performed using TMA/SDTA 840 analyzer (Mettler Toledo) in the range t = 20÷350 °C.

The surface roughness (R_a) of the castings in the area of 50×50 μm was analyzed using a MicroXAM-100 optical profilometer (KLA-Tencor Corp., USA). In order to evaluate the surface roughness of the products, 2 castings were selected (with and without dichloromethane treatment), and 3 areas were examined on each sample: each with 4 measurements. Statistical analysis of the obtained results was performed using Statistica 10 software.

Results and discussion

The main areas of work were to study of the possibility of using PLA plastic as a material for the manufacture of experimental models in investment casting, as well as establishing the temperature characteristics of the model material.

Thermochemical transformations of polylactide up to 1100 °C were studied using TGA and SDTA methods. The results are presented in Fig. 1. The TGA curve at t = 30÷300 °C shows no recorded changes and the weight of the sample practically did not change (the loss was only 1.09 %).

Thermogravimetric studies demonstrated that the main weight loss of the substance occurs when the temperature rises to 390 °C and amounts to 96.98 %. An exothermic effect is observed on the SDTA curve. At t = 300÷390 °C, active thermal degradation of the

polymer occurs (sample weight drops from 98.91 to 3.02 %). Complete burn-out of polylactide occurs at t ~ 500 °C, until it burns out completely, leaving no ash residue. Its further heating to 1100 °C practically does not cause any changes. The weight of the sample goes into minus. This is primarily due to the removal of residual moisture from the porous ceramic crucible as a result of heating to 1100 °C.

Based on the results of the thermogravimetric study, it can be concluded that when heated above 500 °C, PLA plastic samples have zero ash content. It should be noted that the ash content (solid residue) of the lost-wax model during the calcination of ceramic molds is a very important parameter which should be minimal or completely absent. Increased ash content leads to the formation of ash residues after calcination in the body of the shell, reducing the quality of the cast products obtained in them.

The study of the thermal destruction of the model material enabled the temperature and time parameters of the process of removing (burning out) polylactide from the ceramic mold to be defined. Burning temperature is more than 500 °C, the duration is at least 1 hour.

The main reason for the destruction of the ceramic mold during the burning of the polymer model is the difference in the expansion coefficients of ceramics and polylactide. The thermomechanical properties of the plastic were determined by TMA of polylactide in the temperature range of 20—350 °C (Fig. 2). As demonstrated by the data, in the range t = 20÷150 °C no significant changes were detected. Active expansion of polylactide begins at temperatures above 150 °C, indicating the beginning of the melting of the PLA plastic.

In the course of heating the ceramic shell above 150 °C, the polylactide model begins to expand rapidly, exerting significant pressure on the ceramic shell. Therefore, in order to reduce stresses in the process of removing the polylactide model from the ceramic mold, the heating time interval in the range t = = 150÷300 °C needs to be maximized. It is also advisable to use hollow lost-wax casting models with a cellular structure filling degree not more than 30 %. In this case, the stresses in the shell will not exceed its strength.

The use of polymer filament layer-by-layer deposition for the manufacture of accurate lost-wax models is limited due to the high surface roughness and inaccurate dimensions. This is due to the characteristics of their manufacturing technology. When 3D printing a product vertically, a corrugated structure is formed on its surface (the so-called staircase effect) [23; 24].

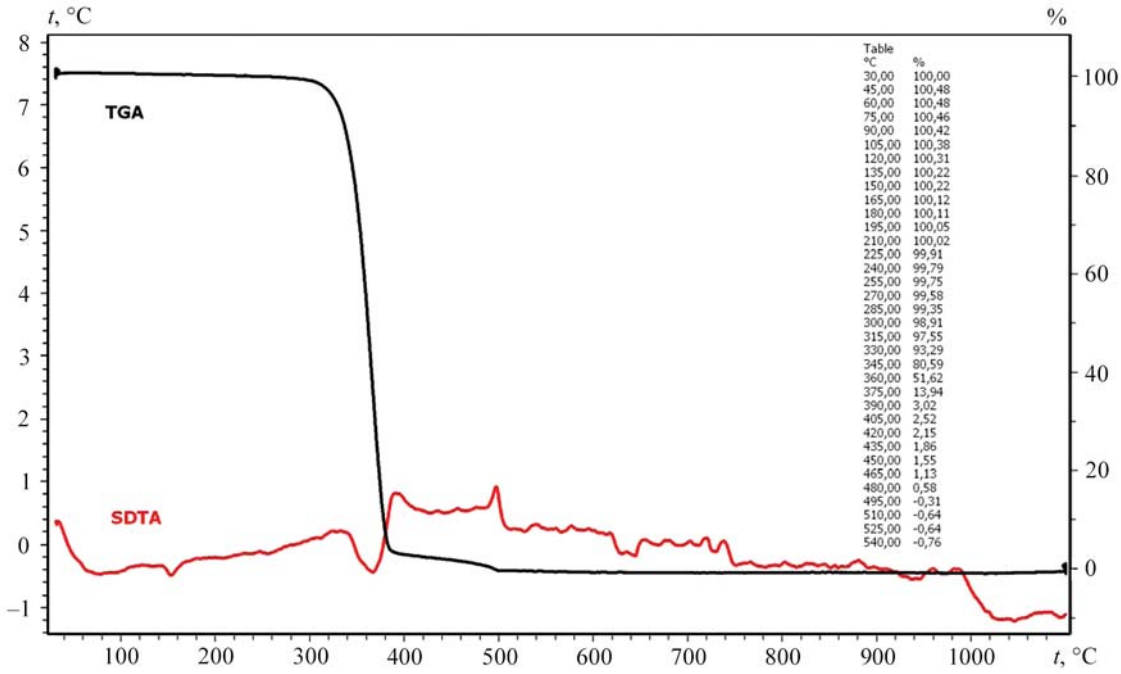

Fig. 1. TGA (black) and SDTA (red) curves of polylactide

Рис. 1. Кривые TGA (черная) и SDTA (красная) полилактида

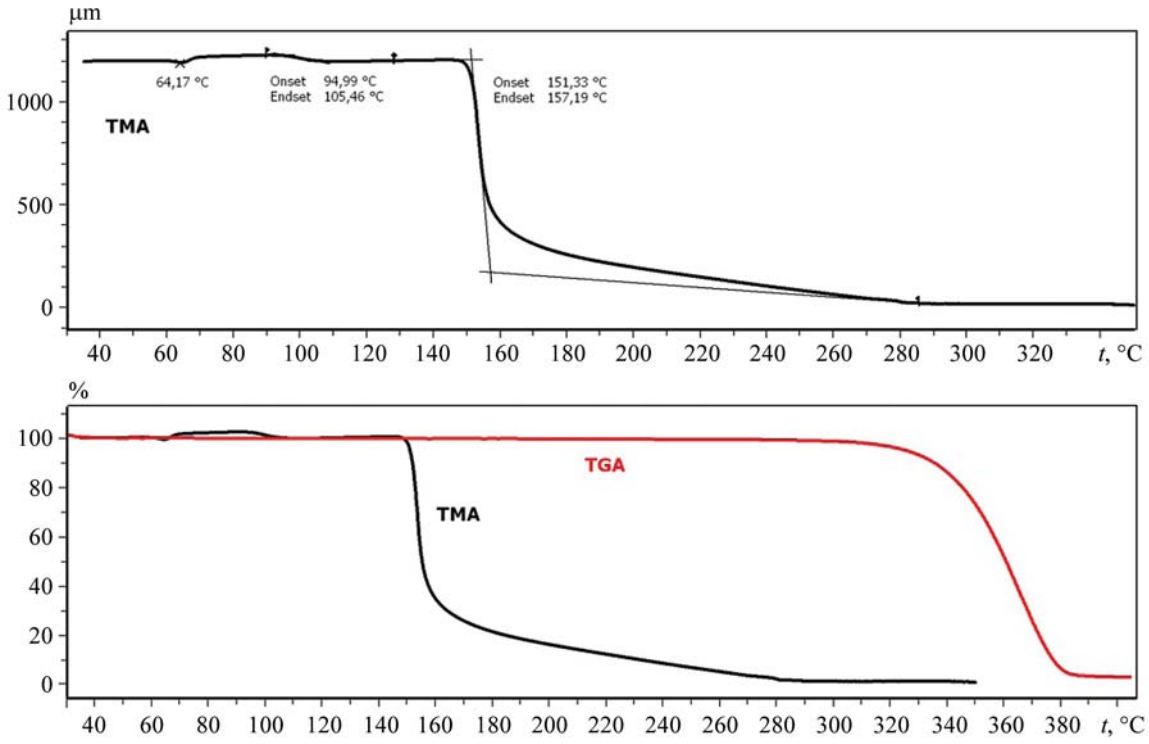

Fig. 2. TMA and TGA curves of polylactide

Рис. 2. Кривые TMA и TGA полилактида

Thus, certain subsequent post-processing procedures are required to improve surface quality [25—27]. At present, two main approaches are used to achieve a smooth surface of products: chemical or mechanical smoothing [28—30]. The latter method is inefficient in obtaining models with a complex geometric surface and a developed structure. The chemical method of smoothing the surface with volatile solvents is more effective.

In this work, dichloromethane (CH_2Cl_2) was used to reduce the surface roughness of the PLA lost-wax models (Fig. 3, *a*) [31]. According to the studies, holding the model in dichloromethane for 10s results in its surface being smoothed (Fig. 3, *c*). With a shorter exposure time in the solvent, the staircase effect is partially preserved (Fig. 3, *b*), and with a longer duration, the model surface swells (Fig. 3, *d*).

This simple, fast and cost-efficient chemical treatment gives the model a smooth and glossy finish, reducing labor and cutting tool costs.

Three-point static bending tests of PLA plates demonstrated a mechanical strength of an average ~45.1 MPa. This result is quite high for casting lost-wax models. Accordingly, during operation (for example, at the site of application of the suspension or during the transportation of model blocks), there is a low probability of their accidental breakage or the formation of dents.

Based on the results of the studies carried out on the Picaso 3D Designer X printer (Picaso 3D, Russia), experimental models were made from PLA polymer (Fig. 4, *a*). Quartz ceramics on a hydrolyzed ethyl silicate binder were used to form a ceramic shell (Fig. 4, *b*). A casting of the "bracket" type manufactured from AK7ch alloy demonstrates the possibility of obtaining suitable aluminum cast products (Fig. 4, *c*).

A comparative analysis of the surface of the experimental castings shows that the cast product acquires a smooth surface (Fig. 5) due to the chemical treatment of the lost-wax model with dichloromethane.

In order to assess the surface quality of castings, their roughness was measured using a laser optical profilometer and they were compared with each other. Figure 6 shows micrographs, as well as 2D and 3D relief of the surface of the castings. Images of castings are made in the same scale. The roughness (R_a) of the castings was measured in several places indicated in Fig. 5.

As illustrated in Fig. 6, the roughness of the samples was significantly reduced by the use of chemical post-processing of the lost-wax models with dichloromethane vapor. There are no surface lines between ad-

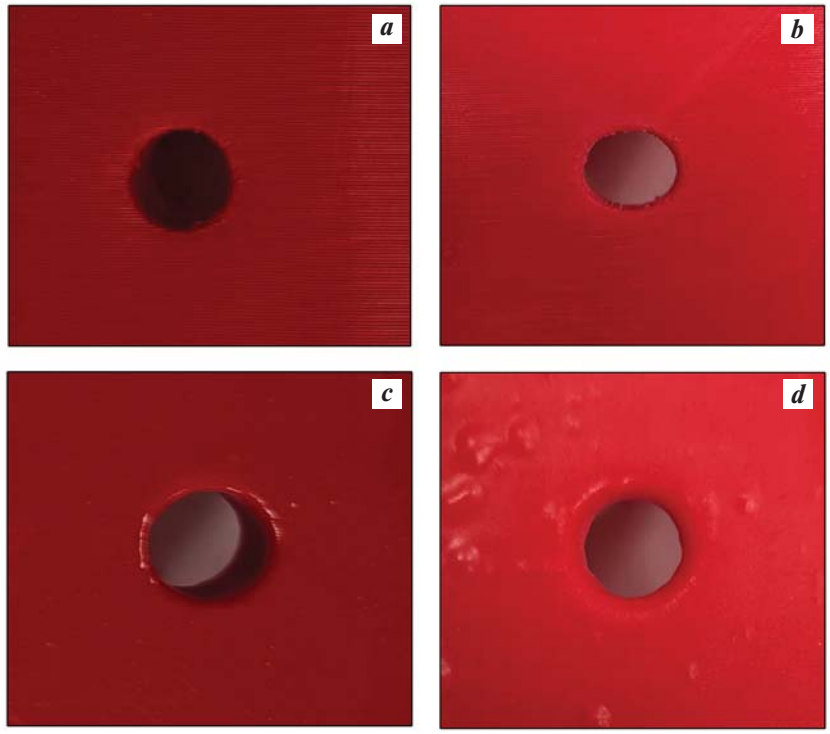

Fig. 3. External view of surface of consumable PLA model
a – after 3D printing; ***b–d*** – after processing by dichloromethane for 5 s (***b***), 10 s (***c***) and 15 s (***d***)

Рис. 3. Внешний вид поверхности выжигаемой PLA-модели
a – после 3D-печати; ***b–d*** – после обработки дихлорметаном в течение 5 с (***b***), 10 с (***c***) и 15 с (***d***)

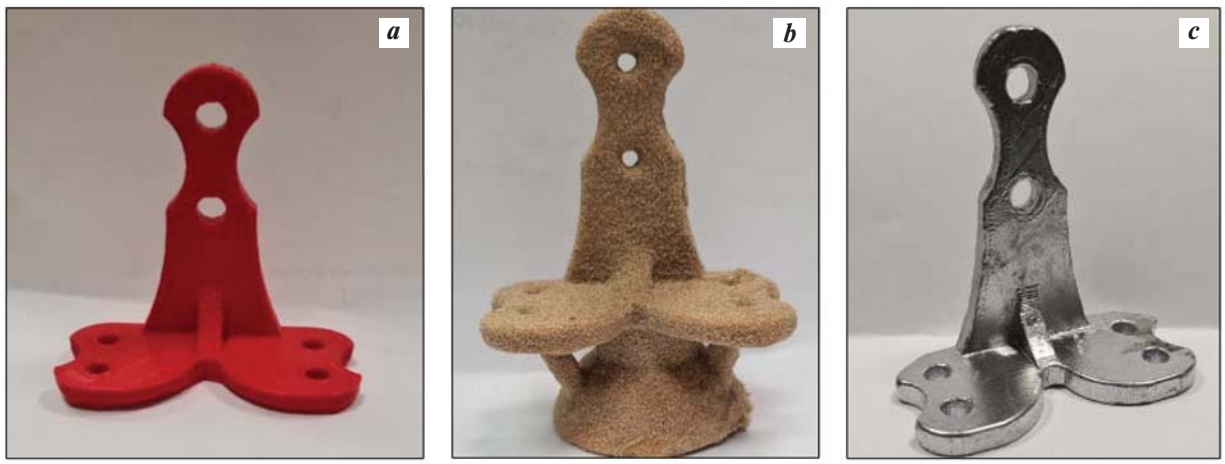

Fig. 4. Experimental PLA model (***a***), applied ceramic layer (***b***), and final aluminum casting (***c***)

Рис. 4. Опытная PLA-модель (***a***), она же с нанесенным слоем керамики (***b***) и готовая алюминиевая отливка (***c***)

jacent layers on the images of the surface of the castings, obtained by PLA lost-wax models and processed with dichloromethane (see Fig. 6, *b*). A noticeable reduction in roughness is observed and the effect of stairs is eliminated.

The surface roughness of castings produced using models before and after chemical processing is illustrated in Fig. 7. The distribution of Kolmogorov—Smirnov and Shapiro—Wilk quantitative indicators showed adequate results. Average values of R_a

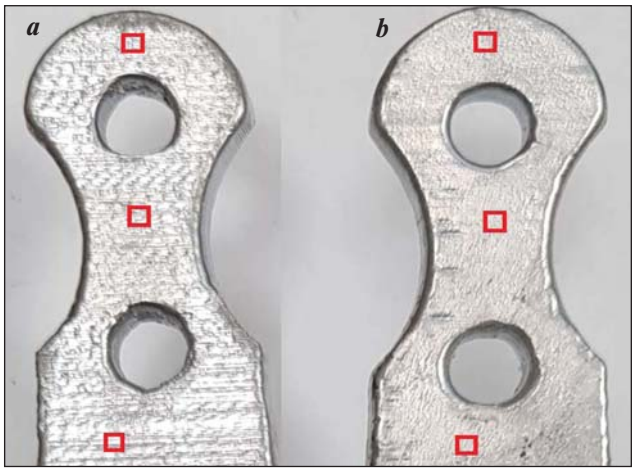

Fig. 5. External view of casting produced using non-processed model (***a***) and after its holding in dichloromethane (***b***)

Рис. 5. Внешний вид отливки, полученной по выжигаемой необработанной модели (***a***) и после ее выдержки в дихлорметане (***b***)

decrease from 13.7 to 2.5 μm. The roughness R_a of a casting produced using a consumable model processed by dichloromethane varies from 1.8 to 3.5 μm. Thus, the surface quality was improved significantly and the roughness decreased by 81.75 %.

Conclusions

This work focused on studying process variables of 3D printing for the rapid production of consumable models from PLA plastic, and subsequent fabrication of experimental cast items from aluminum alloys. The mechanical properties and ash content of burnt samples from polylactide were studied. Thermomechanical and thermogravimetric analyses of the polymer were conducted, resulting in the following main conclusions:

1. The static bending strength of 3D printed consumable PLA models was ~45.1 MPa.

2. The characteristic temperature properties of PLA plastic thermal destruction were detected using thermo-

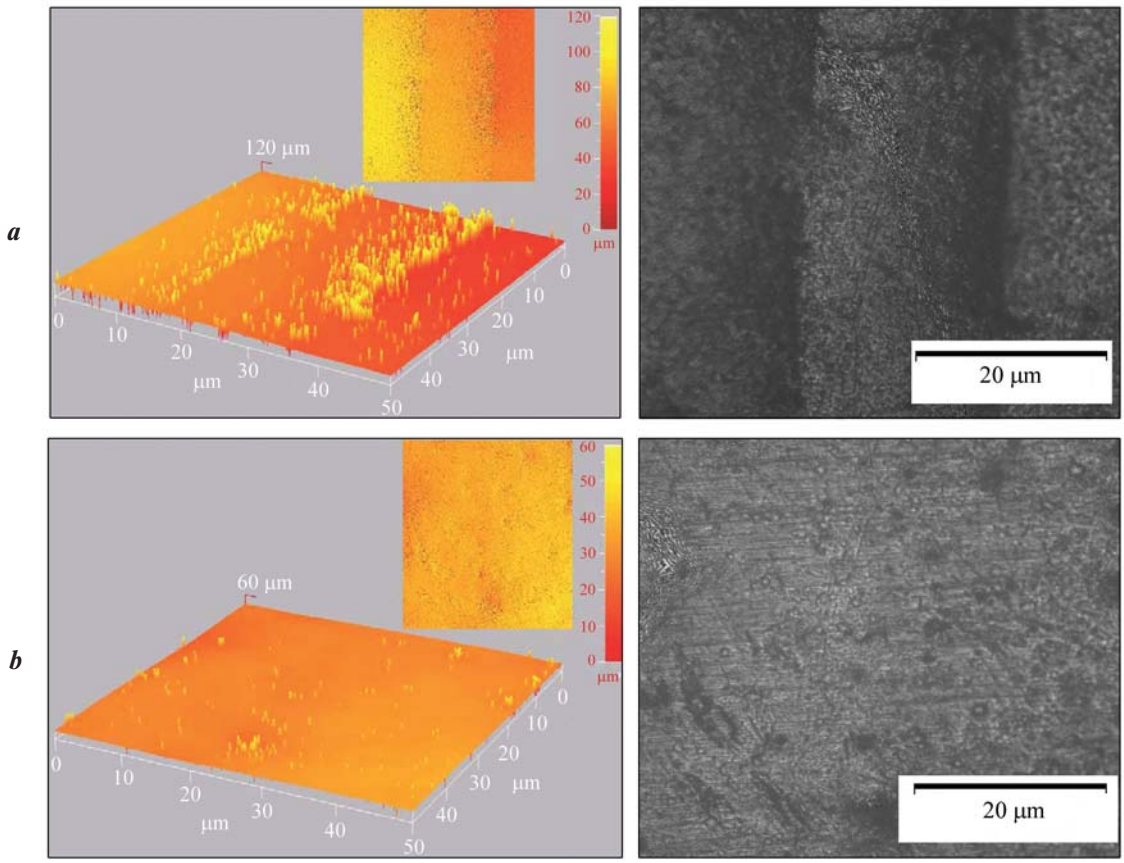

Fig. 6. Micro images 2D (on the right) and 3D (on the left), of surface of castings produced using consumable PLA models, without processing (***a***) and after holding in dichloromethane (***b***)

Рис. 6. Микрофотографии 2D- (справа) и 3D-изображения (слева) поверхности отливок, полученных по выжигаемым PLA-моделям, без обработки (***a***) и после выдержки в дихлорметане (***b***)

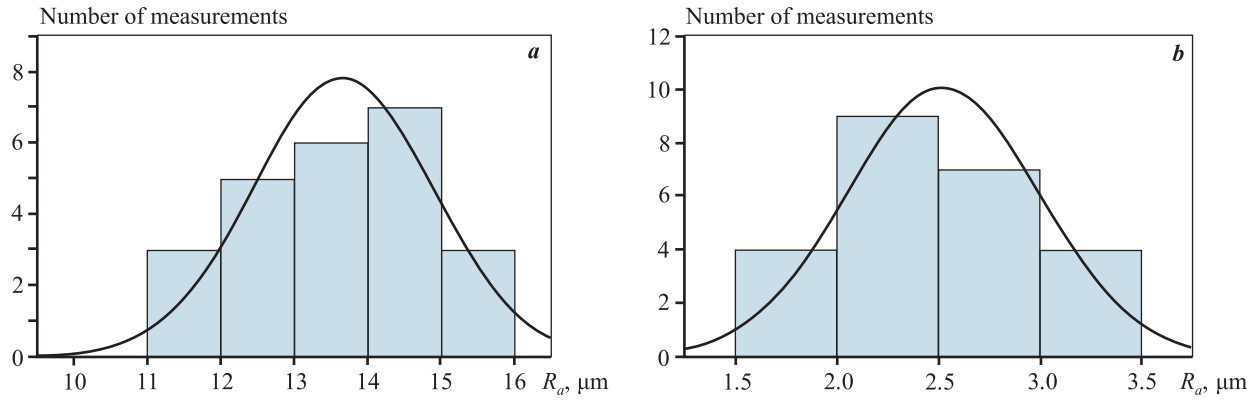

Fig. 7. Distribution histograms of surface roughness (R_a) of casting produced using non-processed model (***a***) and after its processing by dichloromethane (***b***)

Рис. 7. Гистограммы распределения значений шероховатости (R_a) поверхности отливки, полученной по необработанной модели (***a***) и после ее обработки дихлорметаном (***b***)

gravimetric analysis. It was established that polylactide completely burns out upon heating to 500 °C leaving no ash residue.

3. In the course of heating of ceramic shell in excess of 150 °C, the polylactide model begins to expand intensively. In order to decrease stresses during the removal of polylactide model from ceramic mold, the heating time must be increased to the range of 150—300 °C. In addition, the use of hollow consumable casting models with the filling extent of cellular structure not higher than 30 % would be sensible. The stress on the shell will not exceed its strength.

4. In order to decrease the surface roughness of consumable PLA model, chemical post-treatment by dichloromethane must be performed. The best solvent for smoothing model surface layers is dichloromethane. After immersion of the model into the solvent for 10 s, its surface becomes smooth and glossy.

5. The experimental results of the process variables were used. They were then verified under laboratory conditions allowing a good experimental casting of bracket type from aluminum alloys to be obtained. Castings produced on the basis of consumable models processed by dichloromethane show a decrease in the roughness R_a from 13.7 to 2.5 μm. Thus, the ladder effect is eliminated.

References

1. Rosochowski A., Matuszak A. Rapid tooling: The state of the art. *Journal of Materials Processing Technology.* 2000;106(1-3):191—198. https://doi.org/10.1016/S0924-0136(00)00613-0
2. Harun W. S. W., Safian S., Idris M. H. Evaluation of ABS patterns produced from FDM for investment casting process. *WIT Transactions on Engineering Sciences.* 2009;64(3):319—328. https://doi.org/10.2495/MC090301
3. Bassoli E., Gatto A., Iuliano L., Violante M. 3D Printing technique applied to rapid casting. *Rapid Prototyping Journal.* 2007;13(3):148—155. https://doi.org/10.1108/13552540710750898
4. Choe C.M., Yang W.C., Kim U.H., Ri B.G., Om M.S. Manufacture of centrifugal compressor impeller using FDM and investment casting. *The International Journal of Advanced Manufacturing Technology.* 2022;118:173—181. https://doi.org/10.1007/s00170-021-07894-7
5. Gao M., Li L., Wang Q., Ma Z., Li X., Liu Z. Integration of additive manufacturing in casting: Advances, challenges, and prospects. *International Journal of Precision Engineering and Manufacturing-Green Technology.* 2022;9:305—322. https://doi.org/10.1007/s40684-021-00323-w
6. Kumar P., Ahuja I.P.S., Singh R. Application of fusion deposition modelling for rapid investment casting. A review. *International Journal of Materials Engineering Innovation.* 2012;3(3—4):204—227. https://doi.org/10.1504/IJMATEI.2012.049254
7. Kumar P., Singh R., Ahuja I.P.S. Investigations for mechanical properties of hybrid investment casting: A case study. *Materials Science Forum.* 2015;808:89—95. https://doi.org/10.4028/www.scientific.net/MSF.808.89
8. Kumar P, Singh R, Ahuja I.P.S. A framework for developing a hybrid investment casting process. *Asian Review of Mechanical Engineering.* 2013;2(2):49—55. https://doi.org/10.51983/arme-2013.2.2.2346

9. Badanova N., Perveen A., Talamona D. Concise review on pattern making process in rapid investment casting: Technology, materials & numerical modelling aspect. *Advances in Materials and Processing Technologies*. 2022;8:966—978. https://doi.org/ 10.1080/2374068X.2021.1959113
10. Vyavahare S., Teraiya S., Panghal D., Kumar S. Fused deposition modelling: a review. *Rapid Prototyping Journal*. 2020; 26(1):176—201. https://doi.org/10.1108/RPJ-04-2019-0106
11. Bakar N.S.A., Alkahari M.R., Boejang H. Analysis on fused deposition modelling performance. *Journal of Zhejiang University: Science A*. 2010;11(12):972—977. https://doi.org/10.1631/jzus.A1001365
12. Raney K., Lani E., Kalla D.K. Experimental characterization of the tensile strength of ABS parts manufactured by fused deposition modeling process. *Materials Today: Proceedings*. 2017;4:7956—7961. https://doi.org/10.1016/j.matpr.2017.07.132
13. Milde J., Hrušecký R., Zaujec R., Morovic L., Görög A. Research of ABS and PLA materials in the process of fused deposition modeling method. In: *28th DAAAM International Symposium on Intelligent Manufacturing and Automation*. Vienna, Austria, 2017. Vol. 28. P. 812—820. https://doi.org/10.2507/28th.daaam.proceedings.114
14. Hanon M.M., Marczis R., Zsidai L. Influence of the 3D printing process settings on tensile strength of PLA and HT-PLA. *Periodica Polytechnica Mechanical Engineering*. 2020; 65(1): 38—46. https://doi.org/10.3311/PPme.13683
15. Knoop F., Schoeppner V. Mechanical and thermal properties of FDM parts manufactured with Polyamide 12. In: *26th Annual International Solid Freeform Fabrication Symposium*. University of Texas at Austin, 2015. P. 935—948.
16. Szykiedans K., Credo W., Osiński D. Selected mechanical properties of PETG 3-D prints. Procedia Engineering. 2017;177:455—461. https://doi.org/10.1016/j.proeng.2017.02.245
17. Xiaoyong S., Liangcheng C., Honglin M., Peng G., Zhanwei B., Cheng L. Experimental analysis of high temperature PEEK materials on 3D printing test. In: *9th International Conference on Measuring Technology and Mechatronics Automation (ICMTMA)* (14—15 Jan. 2017). Changsha, China, 2017. P. 13—16. https://doi.org/10.1109/ICMTMA.2017.0012
18. Domingo-Espin M., Puigoriol-Forcada J.M., Garcia-Granada A.A., Llumà J., Borros S., Reyes G. Mechanical property characterization and simulation of fused deposition modeling polycarbonate parts. *Materials & Design*. 2015;83:670—677. https://doi.org/10.1016/j.matdes.2015.06.074
19. Nguyen T.T., Tran V.T., Pham T.H.N., Nguyen V.-T., Thanh N.C., Thi H.M.N., Duy N.V.A., Thanh D.N., Nguyen V.T.T. Influences of material selection, infill ratio, and layer height in the 3D printing cavity process on the surface roughness of printed patterns and casted products in investment casting. *Micromachines*. 2023;14:395. https://doi.org/10.3390/mi14020395
20. Gallien F., Gass V., Mortensen A. Investment casting of periodic aluminum cellular structures using slurry-cast table salt moulds. *Materials & Design*. 2022;215:110488. https://doi.org/10.1016/j.matdes.2022.110488
21. Ukey K., Hiremath S., Majumder H. Investigation of investment casting pattern using fused deposition modeling. *Engineering Science & Technology*. 2021;2:201—207. https://doi.org/10.37256/est.222021904
22. Nikitin K.V., Tukabayov B.N., D'yachkov V.N., Nikitin V.I., Deev V.B., Barinov A.Y. Improving the casting process in ceramic forms using additive technologies in manufacturing model kits. *Russian Journal of Non-Ferrous Metals*. 2021;62(6):675—681. https://doi.org/10.3103/S106782122106016X
Никитин К.В., Тукабайов Б.Н., Дьячков В.Н., Никитин В.И., Деев В.Б., Баринов А.Ю. Совершенствование процесса литья в керамические формы за счет применения аддитивных технологий при изготовлении модельных комплектов. *Известия вузов. Цветная металлургия*. 2021;27(5):58—66. https://doi.org/10.17073/0021-3438-2021-5-58-66
23. Alsoufi M.S., Abdulrhman E.E. How surface roughness performance of printed parts manufactured by desktop FDM 3D printer with PLA+ Is influenced by measuring direction. *American Journal of Mechanical Engineering*. 2017;5(5):211—23. https://doi.org/10.12691/ajme-5-5-4
24. Caputo M., Rashwan O., Waryoba D., McDade K. Surface texture and thermo-mechanical properties of material extruded and ironed polylactic acid. *Additive Manufacturing*. 2022;59:103084. https://doi.org/10.1016/j.addma.2022.103084
25. Kumar P., Ahuja I.S., Singh, R. Effect of process parameters on surface roughness of hybrid investment casting. *Progress in Additive Manufacturing*. 2016;1:45—53. https://doi.org/10.1007/s40964-016-0004-9
26. Taşcıoğlu E., Kıtay Ö., Keskin A.Ö., Kaynak Y. Effect of printing parameters and post-process on surface roughness and dimensional deviation of PLA parts fabricated by extrusion-based 3D printing. *Journal of the Brazilian Society of Mechanical Sciences and Engineering*. 2022;44(139). https://doi.org/10.1007/s40430-022-03429-7
27. Garg P.K., Singh R., Ahuja I., Multi-objective optimization of dimensional accuracy, surface roughness and hardness of hybrid investment cast components. *Rapid Prototyping Journal*. 2017;23(5):845—857. https://doi.org/10.1108/RPJ-10-2015-0149

28. Panda S.S., Chabra R., Kapil S., Patel V. Chemical vapour treatment for enhancing the surface finish of PLA object produced by fused deposition method using the Taguchi optimization method. *SN Applied Sciences.* 2020; 2(916):1—13. https://doi.org/10.1007/s42452-020-2740-1
29. Tiwary V.K., Arunkumar P., Deshpande A.S., Rangaswamy N. Surface enhancement of FDM patterns to be used in rapid investment casting for making medical implants. *Rapid Prototyping Journal.* 2019;25(5):904—914. https://doi.org/10.1108/RPJ-07-2018-0176
30. Hashmi A.W., Mali H.S., Meena A. A comprehensive review on surface quality improvement methods for additively manufactured parts. *Rapid Prototyping Journal.* 2022;29(3):504—557. https://doi.org/10.1108/RPJ-06-2021-0133
31. Jin Y., Wan Y., Liu Z. Surface polish of PLA parts in FDM using dichloromethane vapour. In: *The 3rd International Conference on Mechatronics and Mechanical Engineering (ICMME 2016)* (MATEC Web of Conferences). 2016. Vol. 95. P. 05001. https://doi.org/10.1051/matecconf/20179505001

Information about the authors

Maksim S. Varfolomeev – Cand. Sci. (Eng.), Assistant Professor, Department 1101, Moscow Aviation Institute (National Research University) (MAI (NRU)).
http://orcid.org/0000-0003-2164-6428
E-mail: varfolom2a@yandex.ru, varfolom2a@rambler.ru

Igor' A. Petrov – Cand. Sci. (Eng.), Assistant Professor, Department 1101, MAI (NRU).
http://orcid.org/0000-0001-6393-1900
E-mail: petrovia2@mai.ru

Информация об авторах

Максим Сергеевич Варфоломеев – к.т.н., доцент кафедры 1101, Московский авиационный институт (Национальный исследовательский университет) (МАИ (НИУ)).
http://orcid.org/0000-0003-2164-6428
E-mail: varfolom2a@yandex.ru, varfolom2a@rambler.ru

Игорь Алексеевич Петров – к.т.н., доцент кафедры 1101, МАИ (НИУ).
http://orcid.org/0000-0001-6393-1900
E-mail: petrovia2@mai.ru

Contribution of the authors

M.S. Varfolomeev – determined the research objectives, conducted experiments, wrote the manuscript.

I.A. Petrov – tested the samples for strength, measured the surface roughness, participated in the discussion of the results.

Вклад авторов

М.С. Варфоломеев – определение цели работы, проведение экспериментов, написание текста статьи.

И.А. Петров – испытания образцов на прочность, измерение шероховатости поверхности, участие в обсуждении результатов.

The article was submitted 21.03.2023, revised 23.05.2023, accepted for publication 25.05.2023

Статья поступила в редакцию 21.03.2023, доработана 23.05.2023, подписана в печать 25.05.2023

UDC 621.983.3
https://doi.org/10.17073/0021-3438-2023-4-15-23
Research article
Научная статья

Improving shape formation under conditions of plane tensile stress

E.G. Demyanenko, I.P. Popov, A.A. Levagina

Samara National Research University
34 Moscowskoe shosse, Samara 443086, Russia

✉ Alina A. Levagina (aline.levagina@yandex.ru)

Abstract: Thin-walled axisymmetric truncated parts made of sheet billets are actively used in rocket and aerospace engineering. Improvement to their shape formation, based on directed material thickness change will ensure the production of parts with minimum thickness variation. This will also enable aviation and space industry enterprises to attain leading positions, as well as reduce labor costs. This work studies the possibility of obtaining thin-walled axisymmetric parts of truncated tapered shape using one of the methods of sheet metal stamping under flat tensile stress conditions (flanging). The mechanism was identified and the analysis of the stress-strain state of the billet during deformation was carried out. This takes into account the minimizing of the difference between the specified and technologically possible thicknesses. A mathematical model was developed to consider the shaping method based on the process of flanging. Theoretical studies were based on the principles of the plastic deformation theory of sheet materials. This was achieved by the following factors: approximate differential equations of force equilibrium; equations of constraint; plasticity conditions; and fundamental constitutive relations under given initial and boundary conditions. The process of flanging was simulated using the LS-DYNA software package with the following initial data of a conical billet made of 12Kh18N10T steel: cone angle 16.4°, thickness $S_{billet} = 0.3$ mm. The aim was to eliminate errors in designing a tool for future implementation of the method on a manufactured die tooling, as well as to confirm the theoretical conclusions on the selection of technological parameters and achieve minimal thickness variation. The steps of computer modeling are presented, indicating the main process parameters such as material model, mechanical characteristics of the workpiece material, type of elements, kinematic loads, conditions of contact interaction of elements with each other, etc.

Keywords: flanging, thickness, thin-walled, minimization, shape formation, process, engineering method, stresses, LS-DYNA, simulation.

For citation: Demyanenko E.G., Popov I.P., Levagina A.A. Improving shape formation under conditions of plane tensile stress. *Izvestiya. Non-Ferrous Metallurgy.* 2023;29(4):15–23. https://doi.org/10.17073/0021-3438-2023-4-15-23

Совершенствование процесса формообразования в условиях плоского напряженного состояния растяжения

Е.Г. Демьяненко, И.П. Попов, А.А. Левагина

Самарский национальный исследовательский университет имени академика С.П. Королёва
443086, Россия, г. Самара, Московское шоссе, 34

✉ Алина Александровна Левагина (aline.levagina@yandex.ru)

Аннотация: В ракетно-космической и авиационной технике активно применяются тонкостенные осесимметричные детали усеченной сужающейся формы, изготовленные из листовых заготовок. Совершенствование процессов их формообразования, в основе которых направленное изменение толщины материала с целью получения деталей с минимальной разнотолщинностью, позволит обеспечить ведущие позиции предприятий авиационной и космической отраслей промышленности, а также гарантирует снижение трудозатрат. Данная работа посвящена исследованию возможности получения тонкостенных осесим-

метричных деталей усеченной сужающейся формы одним из способов листовой штамповки в условиях плоского напряженного состояния растяжения (отбортовкой). Выявлен механизм и проведен анализ напряженно-деформированного состояния заготовки в процессе формоизменения с учетом выражения минимизации между заданной и технологически возможной толщинами. Разработана математическая модель рассматриваемого способа формообразования, основанного на процессе отбортовки. Теоретические исследования основывались на положениях теории пластического деформирования листовых материалов путем совместного решения приближенных дифференциальных уравнений равновесия сил, уравнений связи, условия пластичности и основных определяющих соотношений при заданных начальных и граничных условиях. С целью исключения ошибок при проектировании инструмента для перспективной реализации способа на изготовленной штамповой оснастке, а также для подтверждения теоретических выводов по выбору технологических параметров и достижения минимальной разнотолщинности проведено моделирование процесса отбортовки в программном комплексе LS-DYNA с исходными данными конической заготовки из стали 12Х18Н10Т: угол конусности 16,4°, толщина $S_{заг}$ = 0,3 мм. Представлены этапы компьютерного моделирования с указанием основных параметров процесса, таких как модель материала, механические характеристики материала заготовки, тип элементов, кинематические нагрузки, условия контактного взаимодействия элементов между собой и т.д.

Ключевые слова: отбортовка, толщина, тонкостенная, минимизация, формообразование, процесс, инженерный метод, напряжения, LS-DYNA, моделирование.

Для цитирования: Демьяненко Е.Г., Попов И.П., Левагина А.А. Совершенствование процесса формообразования в условиях плоского напряженного состояния растяжения. *Известия вузов. Цветная металлургия*. 2023;29(4):15–23.
https://doi.org/10.17073/0021-3438-2023-4-15-23

Introduction

Components such as compartment shells, fairings, fuel tanks of various shapes and sizes, gas storage cylinders, nozzle shells, engine combustion chamber shells and other parts used in the rocket, space and aviation industry must fulfill preset performance characteristics. They must also meet design requirements that determine the technological feasibility of their manufacture [1—4]. The known methods of shape formation [5—7] of such parts do not fully provide the necessary and uniformly distributed thickness (for example, at multiple drawing the thickness variability can reach 80 %). This entails an increase in the number of technological transitions, a decrease in the material utilization rate due to subsequent machining and a general increase in production costs. Associated problems are corrugation (local loss of deformation stability) and deterioration of surface quality.

In order to avoid defects [8—10] in thin-walled parts with a ratio of the preset billet thickness to its major diameter at $S_{preset}/D < 0.08$, shape formation is carried out under conditions of stress state close to the plane tensile stress state. This can be achieved, for example, using processes of flanging and forming. In addition, it is important to design the process in such a way that the thickness of the workpiece varies in the direction associated with a preset part thickness. For this purpose, in real deformation processes, it is important to ensure the minimum thickness variation of the part, defined as a minimization equation in the form of an integral quadratic difference between the preset and technologically possible thicknesses.

The aim of this work was, therefore, to develop a technique for obtaining parts with a preset thickness from a conical billet by flanging.

Theoretical studies of the flanging process to obtain thin-walled axisymmetric parts of a truncated tapering shape

This paper presents the results of the study only for relatively low parts (the ratio of height to major diameter $H/D \approx 1$ and diameter to relative curvature $D/R_p < 0.045$). Let us consider a method for manufacturing thin-walled axisymmetric parts of a truncated tapering shape with a minimum thickness difference from a conical billet using the flanging process. In this case, we use the theory of plastic deformation of sheet materials, taking into account the anisotropy of the mechanical properties of the initial billet and the assessment of the conditions for stable shape formation upon plane tensile stress state. By minimizing the equation for the difference between the preset and technically possible thicknesses, the possibilities of process analysis are expanded. Figure 1 illustrates a schematic view of the method of part flanging from a conic billet.

The tapered billet *4* is clamped between die *3* and clamp *2*, providing a stationary portion of the billet flange under the clamp during shape formation. For example, when punch *1* is lowered, due to the different configuration of the punch and billet geometry, the billet is at first contacted and deformed in the elements of

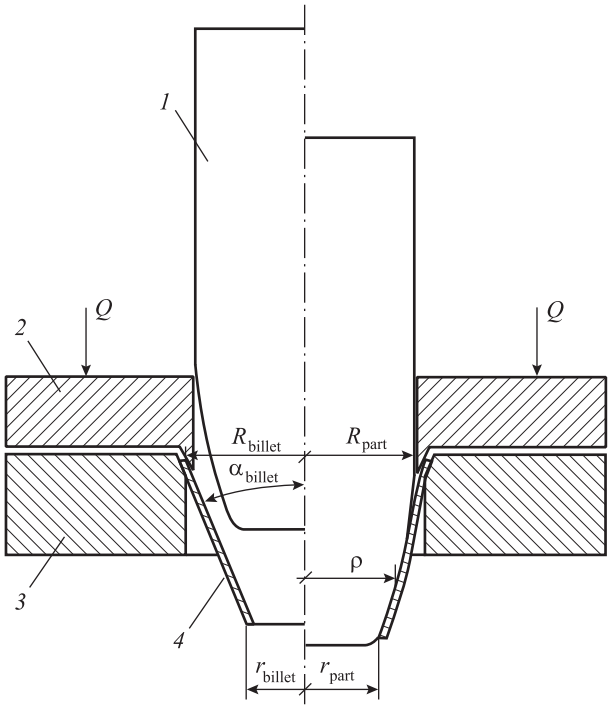

Fig. 1. Geometric layout of shape formation

1 – punch, ***2*** – blank holder, ***3*** – mold, ***4*** – workpiece/part
R_{billet} and R_{part} are the major radii of billet and part, mm;
α_{billet} is the billet cone angle, deg.; r_{billet} and r_{part} are the minor radii of billet and part, mm; Q is the force and direction of clamping, N;
ρ – is the current radius of part, mm

Рис. 1. Геометрическая схема формообразования

1 – пуансон, ***2*** – прижим, ***3*** – матрица, ***4*** – заготовка/деталь
$R_{заг}$ и $R_{дет}$ – наибольшие радиусы заготовки и детали, мм;
$\alpha_{заг}$ – угол конусности заготовки, град; $r_{заг}$ и $r_{дет}$ – наименьшие радиусы заготовки и детали, мм; Q – усилие и направление прижима, Н; ρ – текущий радиус детали, мм

minor diameter. As the punch is lowered, the billet elements with major diameter coordinates enter the zone of deformation center. The process stops when the plastic deformation of the billet edge begins.

Due to the size and geometry of the punch and the workpiece, it is possible to adjust the thickness of the latter along the generatrix length. As a result, the part obtained has a thickness either close to constant, with minimal thickness variation, or with a variable (monotonic) thickness that is close to the preset thickness. It has a minimal thickness variation (with its decrease from the minor diameter edge elements to the elements with the major diameter, and vice versa). The main factors affecting the above-described distribution of part wall thickness are the inclination angle of the tapered billet face, friction, and the mechanical properties of the billet (e.g., anisotropy coefficient of a transversal isotropic body) [11].

Directed change in billet thickness with regard to preset thickness is possible by varying the constants in the process of technological parameters [12] (billet size, tool geometry, coefficient of friction, boundary conditions, mechanical property indicators, etc.). It also requires an analytically [13—15] presented and resolved expression of minimum thickness difference [16—18]:

$$\iint_F (S_{preset} - S_{Th})^2 dF \to \min, \qquad (1)$$

where S_{preset} is the preset part thickness, mm; S_{Th} is the technologically possible thickness, obtained after the shape formation of the billet, mm; F is the area of the part across the median surface, mm^2.

The mathematical condition for achieving a given distribution of the constant wall thickness of the part for implementation of the proposed method is written as follows:

$$\int_{\bar{r}_{part}}^{1} \int \left[(\bar{S}_{preset} - 1) - Q\left(1 - \frac{\bar{r}_{billet}}{\bar{\rho}}\right) \right]^2 d\rho \to \min, \qquad (2)$$

where $\bar{S}_{preset} = S_{preset}/S_{billet}$, $\bar{r}_{billet} = r_{billet}/R_{part}$ and $\bar{\rho} = \rho/R_{part}$.

Let us denote Q:

$$Q = (1-\mu)[(1+\bar{\sigma}_{\rho k})/(\mu\bar{\sigma}_{\rho k} - 1)] = \text{const}, \qquad (3)$$

where $\sigma_{\rho k} = \sigma_\rho/\sigma_\theta$ is the ratio of stresses determined by the engineering method using the equation of equilibrium in polar coordinates [19]. In the case of billet shape formation, assuming that the additional pressure $q = 0$, it will take the following form:

$$\rho\frac{d\sigma_\rho}{d\rho} + d\sigma_\rho - d\sigma_\theta - \frac{f\rho}{\sin\alpha_0}\left(\frac{\sigma_\rho}{R_\rho} + \frac{\sigma_\theta}{R_\theta}\right) = 0,$$

where R_ρ and R_θ are the radii of the part in the meridional and tangential directions; σ_ρ and σ_θ are the stresses in meridional and tangential directions, Pa; f is the coefficient of friction on the inner surface of the workpiece; α_0 is the angle of generatrix inclination of the part to the axis, deg.

Let us write the plasticity condition for flanging:

$$\beta\sigma_s = \sigma_\theta, \qquad (4)$$

where $\beta = 2/\sqrt{7-6\mu}$ is the coefficient determining the stress-strain state of the process taking into account the anisotropy of mechanical properties of the initial billet [20].

With the geometrical ratio $\rho = R_\theta \cos\alpha$ and assumption that $\sigma_\rho / R_\rho = 0$ the equilibrium equation is written as:

$$\bar{\rho}\frac{d\sigma_\rho}{d\bar{\rho}} + \sigma_\rho - \beta\sigma_s(1 + f\mathrm{ctg}\,\alpha) = 0, \quad (5)$$

where α is the angle of inclination of the tangent to the axis of the part, drawn in the middle part of the deformation zone, deg.

Assuming that the stress ratio $\sigma_\rho/\sigma_\theta$, as shown in [19], is not affected by hardening [21—23] and thickness variation, we can find the stresses σ_ρ in the billet under boundary conditions: $\sigma_\rho = 0$, $\bar{\rho} = \bar{r}_{\text{part}}$ and $\bar{\rho} = \rho/R_{\text{part}}$.

We will assume that the stress in the deformation center is constant and equals the average integral value. Its value is determined by the known formula [19] taking into account that the meridional stress is equal to:

$$\sigma_\rho = \beta(1 + f\mathrm{ctg}\alpha)(1 - \bar{r}_{\text{part}}/\bar{\rho}), \quad (6)$$

then the average integral value is:

$$\bar{\sigma}_{\rho k} = \frac{\sigma_{\rho k}}{\sigma_\theta} = \frac{(1 + f\mathrm{ctg}\,\alpha)\int_{\bar{r}_{\text{part}}}^{1}(1 - \bar{r}_{\text{part}}/\bar{\rho})\,d\bar{\rho}}{1 - \bar{r}_{\text{part}}}. \quad (7)$$

After algebraic transformations we obtain:

$$\bar{\sigma}_{\rho k} = (1 + f\mathrm{ctg}\,\alpha)\frac{1 - \bar{r}_{\text{part}}(1 - \ln\bar{r}_{\text{part}})}{1 - \bar{r}_{\text{part}}}. \quad (8)$$

Next, it is necessary to determine the ratio $\bar{r}_{\text{billet}}/\bar{\rho}$. Let us make the following assumption:

$$\bar{r}_{\text{billet}} = a + b\bar{\rho}. \quad (9)$$

At $\rho = \rho/R_{\text{part}}$ and $\bar{r}_{\text{billet}} = r_{\text{billet}}/R_{\text{part}} = 1$ Eq. (7) is rewritten as follows:

$$\bar{b} = 1 - \bar{a}. \quad (10)$$

Taking into account Eq. (10), Eq. (9) will be presented in the following form:

$$\bar{r}_{\text{billet}} = \bar{a} + (1 - \bar{a})\bar{\rho} = \bar{a}(1 - \bar{\rho}) + \bar{\rho}. \quad (11)$$

Let us carry out a minimization for the case of changing the preset thickness of the part: decrease from the major diameter. With such a flanging scheme (Fig. 1), the defining function of a given thickness is described by the following equation:

$$\bar{S}_{\text{preset}} = 1 - [m/(1 - \bar{r}_{\text{part}})](1 - \bar{\rho}), \quad (12)$$

where $m = 1 - S_{\text{preset}}/S_{\text{billet}} < 1$.

Let us write the minimization condition (2), taking into account Eq. (12):

$$\int_{\bar{r}_{\text{part}}}^{1}\left[-\frac{m}{1 - \bar{r}_{\text{part}}}(1 - \bar{\rho}) + Q\left(1 - \frac{\bar{r}_{\text{billet}}}{\bar{\rho}}\right)\right]^2 d\rho \to \min. \quad (13)$$

Equation (14) with consideration for Eq. (11) will be rewritten as follows:

$$\int_{\bar{r}_{\text{part}}}^{1}\left[-\frac{m}{1 - \bar{r}_{\text{part}}}(1 - \bar{\rho}) + Q\bar{a}\left(\frac{1}{\bar{\rho}} - 1\right)\right]^2 d\rho \to \min. \quad (14)$$

Varying $\bar{a}$ and taking the derivative, we obtain the following equation:

$$\bar{a} = \frac{\frac{m}{1 - \bar{r}_{\text{part}}}\int_{\bar{r}_{\text{part}}}^{1}\left[(1 - \bar{\rho})\left(\frac{1}{\bar{\rho}} - 1\right)\right]d\rho}{\left[Q\int_{\bar{r}_{\text{part}}}^{1}\left(\frac{1}{\bar{\rho}} - 1\right)^2\right]d\bar{\rho}}. \quad (15)$$

After integration, it will take the following form:

$$\bar{a} = \frac{-\frac{m}{1 - \bar{r}_{\text{part}}}\left[-\ln\bar{r}_{\text{part}} - 2(1 - \bar{r}_{\text{part}}) + 0{,}5 - \frac{\bar{r}_{\text{part}}^2}{2}\right]}{Q(1/\bar{r}_{\text{part}} + 2\ln\bar{r}_{\text{part}} - \bar{r}_{\text{part}})}. \quad (16)$$

Let us determine the relative technologically possible thickness of the part according to the following equation:

$$\bar{S}_{\text{Th}} = 1 + Q(1 - \bar{r}_{\text{billet}}/\rho). \quad (17)$$

Using Eqs. (3), (9), (12) and (16), $m = 0.1$, $\sigma_{\rho k} = 0.3311$, $Q = -0.7976$, $a = -0.1497$ are obtained, and the distribution of the technologically possible and specified thicknesses of the convex part is plotted with the following parameters: major radius $R_{\text{part}} = 22.35$ mm; minor radius $r_{\text{part}} = 11.05$ mm; radius of curvature of the part in the meridional direction $R_\rho = 1000$ mm. The part was obtained from a billet with a taper angle $\alpha_{\text{billet}} = 16.4°$ during shape formation with a coefficient of friction on the inner surface of the workpiece $f = 0.05$ and taking into account the anisotropy coefficient of the transversely isotropic body $\mu = 0.5$.

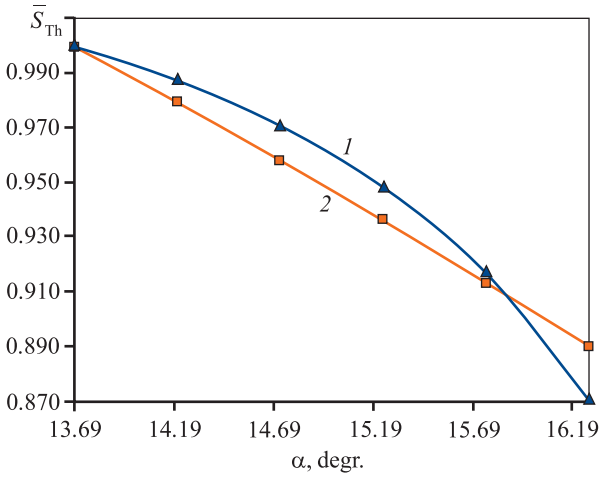

Fig. 2. Distribution of relative technologically possible at $f = 0.05$ and $\mu = 0.5$ (***1***) and relative preset (***2***) thickness of a thin-walled convex part

Рис. 2. Распределение относительной технологически возможной при $f = 0{,}05$ и $\mu = 0{,}5$ (***1***) и относительной заданной (***2***) толщин тонкостенной выпуклой детали

The data obtained made it possible to plot the distribution of the relative technologically possible thickness of the part along the deformation zone, according to the proposed method (Fig. 2).

Simulation of shape formation in LS-DYNA software

In order to eliminate errors in the design of a tool for the future implementation of the method on manufactured die tooling [24], we applied the method of simulating shape formation in specialized finite element software systems. A variety of programs, such as LS-DYNA, ANSYS, Abaqus, QFORM, DEFORM, etc., are used for calculation of process variables. Despite the fact that much scientific literature is devoted to the study of plastic flow, theoretical equations can be derived only for relatively simple processes (bending, drawing, precipitation), and with significant assumptions for billets of simple shape (round, cylindrical, square). However, when using billets of a complex shape and developing more advanced metal forming technologies (MPT), such equations give significant errors, and it is difficult to obtain a solution with approximate methods.

The solution to this problem can be to use programs based on the finite element method, such as ANSYS / LS-DYNA, which is one of the best in its field. It is intended for calculations of high-speed and dynamic processes and ideal for solving problems of mechanical engineering, including cold sheet stamping. The software enables dangerous zones and segments of the model in which destruction is possible to be identified. It can also determine all the necessary parameters:

— stress-strain state of the billet and tool at any point and at any time;

— energy parameters of the process;

— values of efforts and torques, normal and tangential forces;

— contact parameters;

— many other factors necessary for an understanding of the processes occurring in the billet.

Nowadays, there is a wide choice of programs for simulating various scenarios [25—31], successfully used in various fields of mechanical engineering.

The need to resolve these problems in LS-DYNA system can be explained, among other things, by the possibility of calculating thin-walled shells. The kinematic diagram of the simulation process is shown in Fig. 3.

The billet and tool geometry (clamp, die, punch) were designed using ASCON Compass-3D 3D modeling system [32] and exported in a common data exchange format between CAD/CAE applications: Iges. Directly using ANSYS/LS-DYNA, the punch, mold, and billet were assigned the element type - Shell, a shell element. The BOUNDARY_SPC constraint was set on the billet flange nodes to prevent movement along

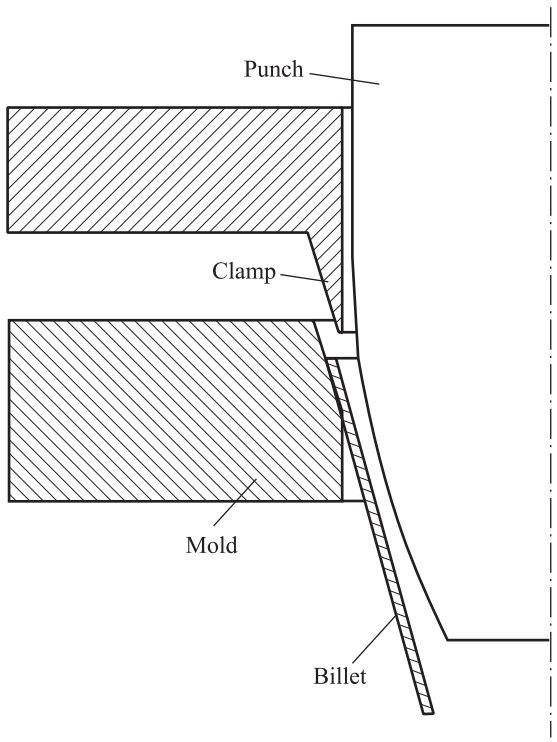

Fig. 3. Kinematic diagram of flanging

Рис. 3. Кинематическая схема процесса отбортовки

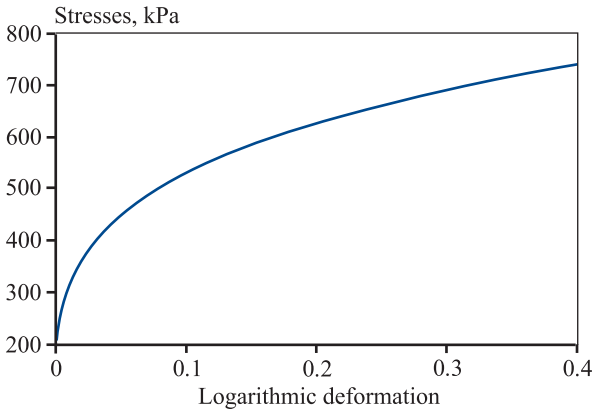

Fig. 4. Experimental hardening curve of 12Kh18N10T steel

Рис. 4. Экспериментальная кривая упрочнения стали 12Х18Н10Т

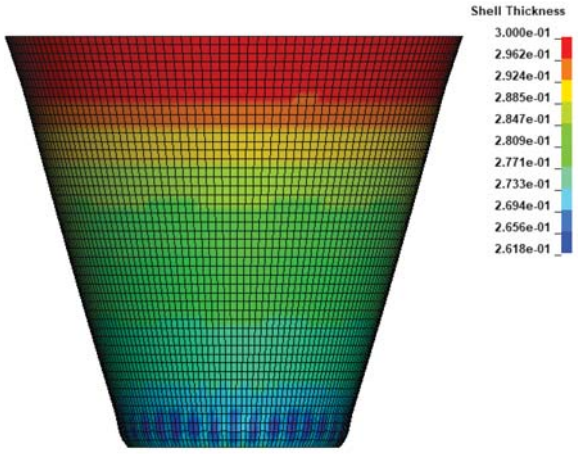

Fig. 5. Distribution of wall thickness (mm) of an axisymmetric part

Рис. 5. Распределение толщины (мм) стенки осесимметричной детали

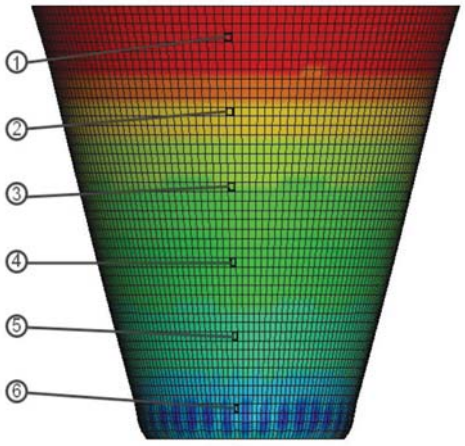

Fig. 6. Selection of points along the generatrix of an axisymmetric part

Рис. 6. Выбор точек по образующей осесимметричной детали

and rotation around axes. The command performs the clamping and mold functions. The boundary conditions and constraints on the degrees of freedom of the punch are set in such a way that the tool moves only along the *OZ* axis. The coefficient of friction between the punch and the billet was 0.05. After positioning the objects along the *OZ* axis, a regular (quadrilateral) finite element mesh with an edge length of 1 mm for the workpiece and a mixed mesh with an edge length of 2 mm for the punch were plotted for them. A rigid model was chosen as the material model of the punch and workpiece: MAT_RIGID and transversely anisotropic: MAT_TRANSVERSELY_ANISOTROPIC_ELASTIC_PLASTIC, respectively.

In order to specify the properties [33] of the material of the billet (12Kh18N10T), an experimental hardening curve for this structural steel was introduced, obtained during a simple tensile test (Fig. 4).

Results and discussion

To describe the properties of the material of a thin-walled billet with a thickness of S_{billet} = 0.3 mm from steel 12Kh18N10T, the following parameters were introduced:

— steel density: 7920 kg/mm2;
— elasticity modulus: 198 GPa;
— Poisson's ratio: 0.29;
— coefficient taking into account the anisotropy of a transversely isotropic billet: 0.5.

The simulation results are illustrated in Fig. 5.

For a comparative analysis of the simulation results, we selected points along the generatrix of the axisymmetric part (Fig. 6) and plotted the function reflecting the thickness at these points (Fig. 7). For illustration, let us add the relative specified thickness of the part to the plot, which will enable a conclusion about the minimum deviation obtained of the thickness of the part from a given value, not exceeding 2.0 %.

Conclusions

The following conclusions were drawn from the study.

1. The maximum discrepancy between the simulation and theoretical data does not exceed 1.5 %. The minimum variation in thickness is observed at a punch angle of 15.36°, and the maximum at 16.79° (see Fig. 7).

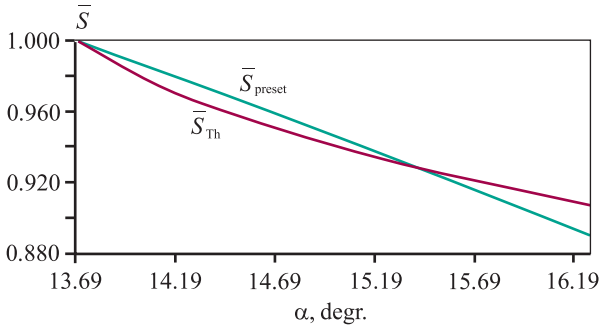

Fig. 7. Distribution of relative technologically possible thickness according to the results of simulation and relative preset thickness of a thin-walled convex part

Рис. 7. Распределение относительных значений технологически возможной толщины (по результатам моделирования) и заданной толщины тонкостенной выпуклой детали

2. A comparison of simulation results and theoretical studies using the proposed method indicates their satisfactory agreement.

3. The required thickness distribution was achieved (see Fig. 6): it decreases from major to minor radii with a minimum deviation from the specified value.

References

1. Shanmuganatan S.P., Kumar V.S.S. Experimental investigation and finite element modeling on profile forming of conical component using Al 3003 (O) alloy. *Materials & Design*. 2012;36:564—569. https://doi.org/10.1016/j.matdes.2011.11.066
2. Bambach M., Voswinckel H., Hirt G. A new process design for performing hole-flanging operations by incremental sheet forming. *Procedia Engineering*. 2014;81:2305—2310. https://doi.org/10.1016/j.proeng.2014.10.325
3. Popov V.G., Iaroslavtsev N.L. Liquid propellant rocket engines. Moscow: Russian State Technological University, 2001. 171 p. (In Russ.).
   Попов В.Г., Ярославцев Н.Л. Жидкостные ракетные двигатели. М.: МАТИ, 2001. 171 с.
4. Rezchikov A.F., Kochetkov A.V., Zakharov O.V. Mathematical models for estimating the degree of influence of major factors on performance and accuracy of coordinate measuring machines. *MATEC Web Conf*. 2017;129:01054. https://doi.org/10.1051/matecconf/201712901054
5. Cao T., Lu B., Ou H., Long H., Chen J. Investigation on a new hole-flanging approach by incremental sheet forming through a featured tool. *International Journal of Machine Tools and Manufacture*. 2016;110:1—17. https://doi.org/10.1016/j.ijmachtools.2016.08.003
6. Grigor'ev A.V., Karachunskii A.D., Shingel' E.G., Mikhailov A.A. Method for manufacturing hollow axisymmetric products with a flange: Author's certificate 1636089 (USSR). 1991. (In Russ.).
   Григорьев А.В., Карачунский А.Д., Шингель Е.Г., Михайлов А.А. Способ изготовления полых осесимметричных изделий с фланцем: Авт. св-во 1636089 (СССР). 1991.
7. Romanovsky V.P. Handbook of cold forging. Leningrad.: Mashinostroenie, 1979. 520 p. (In Russ.).
   Романовский В.П. Справочник по холодной штамповке. 6-е изд. Л.: Машиностроение, 1979. 520 с.
8. You D., Cai D., Wang Y., Zhou F., Ruan Z. Novel hydromechanical reverse drawing method for thin-walled aluminum alloy sheet forming. *The International Journal of Advanced Manufacturing Technology*. 2022;120(5):3741—3756. https://doi.org/ 10.1007/s00170-022-08936-4
9. Chumadin A.S., Ershov V.I., Kovalev A.D., Deberdeev E.M. Method of manufacturing thin-walled shells: Author's certificate 1465152 (USSR). 1989. (In Russ.).
   Чумадин А.С., Ершов В.И., Ковалев А.Д., Дебердеев Е.М. Способ изготовления тонкостенных оболочек: Авт. св-во 1465152 (СССР). 1989.
10. Yakovlev S.S., Remnev K.S. Folding when drawing axisymmetric parts from anisotropic material. *Izvestiya vysshikh uchebnykh zavedenii. Mashinostroenie*. 2014;9:39—47. (In Russ.). https://doi.org/10.18698/0536-1044-2014-9-39-47
    Яковлев С.С., Ремнев К.С. Складкообразование при вытяжке осесимметричных деталей из анизотропного материал. *Известия высших учебных заведений. Машиностроение*. 2014;9:39—47. https://doi.org/10.18698/0536-1044-2014-9-39-47
11. Song Y., Dai D., Geng P., Hua L. Formability of aluminum alloy thin-walled cylinder parts by servo hot stamping. *Procedia Engineering*. 2017;207:741—746. https://doi.org/10.1016/j.proeng.2017.10.822
12. Frącz W., Stachowicz F., Trzepieciński T. Investigations of thickness distribution in hole expanding of thin steel sheets. *Archives of Civil and Mechanical Engineering*. 2012;3:279—283. https://doi.org/10.1016/j.acme.2012.06.006
13. Nepershin R.I. Thin-walled conical shell drawing from a plane blank. *Mechanics of solids*. 2010;45:111—122. https://doi.org/10.3103/S0025654410010140
    Непершин Р.И. Вытяжка тонкостенной конической оболочки из плоской заготовки. *Механика твердого тела*. 2010;1:139—153.
14. Wankhede P., Narayanaswamy N. G., Suresh K., Priyadarshini A. A portable device for single point strain

analysis in sheet metal forming processes. *HardwareX*. 2022: e00371.
https://doi.org/10.1016/j.ohx.2022.e00371

15. Dou W., Xu Z., Han Y., Huang F. A ductile fracture model incorporating stress state effect. *International Journal of Mechanical Sciences*. 2022: 107965.
https://doi.org/10.1016/j.ijmecsci.2022.107965
16. Dem'ianenko E.G., Popov I.P. Design of technological processes shaping of thin-walled axisymmetric parts of aircraft: Textbook. Samara: Samara State Aerospace University, 2014. 144 p. (In Russ.).
Демьяненко Е.Г., Попов И.П. Проектирование технологических процессов формообразования тонкостенных осесимметричных деталей летательных аппаратов: Учебное пособие. Самара: Изд-во СГАУ, 2014. 144 с.
17. Dem'ianenko E.G., Popov I.P. Sheet metal stamping technology. Pt. 1. Deformation methods based on the processes of forming, flanging and drawing thin-walled axisymmetric parts. Samara: Samara State Aerospace University, 2013. 112 p. (In Russ.).
Демьяненко Е.Г., Попов И.П. Технология листовой штамповки. Часть 1. Способы деформирования, основанные на процессах формовки, отбортовки и вытяжки тонкостенных осесимметричных деталей. Самара: Изд-во СГАУ, 2013. 112 с.
18. Popov I.P. Directional change in the thickness of the sheet blank in plastic deformation processes: A tutorial. Samara: Samara State Aerospace University, 2006. 74 p. (In Russ.).
Попов И.П. Направленное изменение толщины листовой заготовки в процессах пластического деформирования: Учебное пособие. Самара: Изд-во СГАУ, 2006. 74 с.
19. Storozhev M.V., Popov E.A. Theory of metal forming. Moscow: Mashinostroenie, 1971. 424 p. (In Russ.).
Сторожев М.В., Попов Е.А. Теория обработки металлов давлением. М.: Машиностроение, 1971. 424 с.
20. Grechnikov F.V. Deformation of anisotropic materials. Moscow: Mashinostroenie, 1998, 448 p. (In Russ.).
Гречников Ф.В. Деформирование анизотропных материалов. М.: Машиностроение, 1998. 448 с.
21. Dmitriev A.M., Vorontsov A.L. Approximation of metal hardening curves. *Kuznechno-shtampovochnoe proizvodstvo. Obrabotka materialov davleniem*. 2004;(1):23—26. (In Russ.).
Дмитриев А.М., Воронцов А.Л. Аппроксимация кривых упрочнения металлов. *Кузнечно-штамповочное производство. Обработка материалов давлением*. 2004;(1):23—26.
22. Lysov M.I., Zakirov I.M. Plastic shaping of thin-walled aircraft parts. Moscow: Mashinostroenie, 1983, 176 p. (In Russ.).
Лысов М.И., Закиров И.М. Пластическое формообразование тонкостенных деталей авиатехники. М.: Машиностроение, 1983. 176 с.
23. Lysov M.I., Sosnov N.V. Shaping parts by bending. Moscow: Mashinostroenie, 2001. 388 p. (In Russ.).
Лысов М.И., Соснов Н.В. Формообразование деталей гибкой. М.: Машиностроение, 2001. 388 с.
24. Takuda H., Tanaka Y., Hatta N. Finite element analysis of forming limit in bore expanding of aluminium alloy sheets. *Archive of Applied Mechanics*. 1998;68(7): 566—576.
https://doi.org/10.1007/s004190050187
25. Gun G.Ya. Mathematical modeling of metal forming processes, 1983. 352 p. (In Russ.).
Гун Г.Я. Математическое моделирование процессов обработки металлов давлением. М.: Металлургия, 1983. 352 с.
26. Radonjic R., Liewald M. New process design for reduction of springback by forming with alternating blank draw-in. *Procedia Manufacturing*. 2019;29:217—224.
https://doi.org/10.1016/j.promfg.2019.02.129
27. Guan Y., Li C., Guo S., Lin P. A novel combined process of flaring-upsetting for forming end flanges on thin-walled tubes. *Journal of Manufacturing Processes*. 2022;84:927—936. https://doi.org/10.1016/j.jmapro.2022.10.051
28. Dewang Y., Purohit R., Tenguria N. A study on sheet metal hole-flanging process. *Materials Today: Proceedings*. 2017;4(4):5421—5428.
https://doi.org/10.1016/j.matpr.2017.05.053
29. Sin' L., Evsiukov S.A., Zhongqi Yu. Studies of the process of drawing into a conical matrix. *Izvestiia Tul'skogo gosudarstvennogo universiteta. Tekhnicheskie nauki*. 2019; 9:513—520. (In Russ.).
Синь Л., Евсюков С.А., Чжунци Ю. Исследования процесса вытяжки в коническую матрицу. *Известия Тульского государственного университета. Технические науки*. 2019;9:513—520.
30. Kukhar' V.D., Malyshev A.N., Bessmertnaia Yu.V. Extraction of low rectangular boxes from profile blanks. *Chernye metally*. 2019;1:39—42. (In Russ.).
Кухарь В.Д., Малышев А.Н., Бессмертная Ю.В. Вытяжка низких прямоугольных коробок из профильных заготовок. *Черные металлы*. 2019;1:39—42.
31. Sosenushkin E.N., Kadymov V.A., Ianovskaia E.A., Tatarintsev A.A., Sosenushkin A.E. On the issue of modeling the stress-strain state in the processing of materials by pressure. *Izvestiia TulGU. Tekhnicheskie nauki*. 2017;11(1):82—100. (In Russ.).
Сосенушкин Е.Н., Кадымов В.А., Яновская Е.А., Татаринцев А.А., Сосенушкин А.Е. К вопросу о

моделировании напряженно-деформированного состояния при обработке материалов давлением. *Известия ТулГУ. Технические науки.* 2017;11(1): 82—100.

32. Bol'shakov V.P., Chagina A.V. 3D modeling in KOMPAS-3D versions V17 and higher: Textbook for universities. Saint Petersburg: Piter, 2021, 256 p. (In Russ.).
Большаков В.П., Чагина А.В. 3D-моделирование в КОМПАС-3D версий V17 и выше: Учебное пособие для вузов. СПб: Питер, 2021. 256 с.
33. Shinkin V.N. Direct and inverse nonlinear approximation of the hardening zone of steel. *Chernye metally*: 2019;(3): 32—37.
Шинкин В.Н. Прямая и обратная нелинейная аппроксимация зоны упрочнения стали. *Черные металлы*. 2019; (3): 32—37.

Information about the authors

Elena G. Demyanenko – Dr. Sci. (Eng.), Professor, Department of Metal Forming, Leading Researcher of the Research Laboratory of Plastic Deformation of Special Material (RL-37), Samara National Research University.
https://orcid.org/0000-0003-2518-9762
E-mail: e-dem@mail.ru

Igor P. Popov – Dr. Sci. (Eng.), Professor, Department of Metal Forming, Leading Researcher of RL-37, Samara National Research University.
https://orcid.org/0000-0001-6497-0004
E-mail: igr_popov@mail.ru

Alina A. Levagina – Laboratory Assistant of RL-37, Samara National Research University.
https://orcid.org/0000-0002-7270-6008
E-mail: aline.levagina@yandex.ru

Информация об авторах

Елена Геннадьевна Демьяненко – д.т.н., профессор кафедры обработки металлов давлением, вед. науч. сотрудник научно-исследовательской лаборатории пластического деформирования специальных материалов (НИЛ-37), Самарский национальный исследовательский университет имени академика С.П. Королёва.
https://orcid.org/0000-0003-2518-9762
E-mail: e-dem@mail.ru

Игорь Петрович Попов – д.т.н., профессор кафедры обработки металлов давлением, вед. науч. сотрудник НИЛ-37, Самарский национальный исследовательский университет имени академика С.П. Королёва.
https://orcid.org/0000-0001-6497-0004
E-mail: igr_popov@mail.ru

Алина Александровна Левагина – лаборант НИЛ-37, Самарский национальный исследовательский университет имени академика С.П. Королёва.
https://orcid.org/0000-0002-7270-6008
E-mail: aline.levagina@yandex.ru

Contribution of the authors

E.G. Demyanenko – scientific guidance, wrote the manuscript, conducted experiments, formulated the conclusions.

I.P. Popov – formulated the main concept, set the goal and objectives of the study, revised the conclusions, performed the calculations.

A.A. Levagina – mathematical simulation, tooling design, wrote the manuscript.

Вклад авторов

Е.Г. Демьяненко – научное руководство, подготовка текста, проведение экспериментов, формулировка выводов.

И.П. Попов – формирование основной концепции, постановка цели и задачи исследования, корректировка выводов, проведение расчетов.

А.А. Левагина – проведение математического моделирования, проектирование оснастки, подготовка текста статьи.

The article was submitted 14.04.2023, revised 12.05.2023, accepted for publication 15.05.2023

Статья поступила в редакцию 14.04.2023, доработана 12.05.2023, подписана в печать 15.05.2023

UDC 669.1
https://doi.org/10.17073/0021-3438-2023-4-24-34

Research article
Научная статья

Features of formation of the Al–Ni–Zr system alloy structure obtained by reducing oxide compounds by aluminothermy using SHS metallurgy

Kh. Ri, E.Kh. Ri, M.A. Ermakov, E.D. Kim

Pacific National University
136 Tikhookeanskaya Str., Khabarovsk 680035, Russia

✉ Evgeniy D. Kim (jenya_1992g@mail.ru)

Abstract: This work is focused on establishing the regularity of the effect of zirconium (2.21; 3.29; 3.69 and 6.92 wt.% Zr) on structure formation, the nature of distribution of elements and the microhardness of structural components in the Al–Ni–Zr system alloys obtained by aluminothermy using the SHS metallurgy. Regularities of the formation of structural components and their microhardness depending on the content of zirconium in Al–Ni alloys (50 wt.%) have been identified and scientifically substantiated. Structural components were identified by the methods of electromicroscopic studies and *X*-ray microanalysis of elements. The structure of the initial alloy consists of Al_3Ni_2 (β′-phase) and Al_3Ni nickel aluminides. Zirconium doping of the alloy in the amount of 2.21 wt.% leads to crystallization of zirconium nickel aluminide $Al_2(Ni,Zr)$. With further increase in the content of zirconium (more than 2.21 wt.% Zr), complex alloyed intermetallic compounds crystallize – Zr, W, Si aluminides and Ni zirconides. A regularity was established in the decrease of the solubility of nickel in nickel aluminides Al_3Ni_2 and Al_3Ni and their microhardness as the zirconium content increases in the Al–Ni–Zr alloys from 2.21 to 6.92 wt.%. In nickel aluminide with zirconium $Al_2(Ni,Zr)$, this contributes to a decrease in the solubility of Ni, Al and increase in the concentration of Si and Zr. Zirconium doping of the Al–Ni alloy in the amount over 2.21 wt.% contributes to an increase in hardness (*HRA*), despite a decrease in the microhardness of the metal base (Al_3Ni_2, Al_3Ni and $Al_2(Ni,Zr)$). The main reason for increasing the hardness of the Al–Ni–Zr alloys is the crystallization of complex-alloyed intermetallides – Zr, W, Si aluminides and nickel zirconide, which probably have an increased microhardness. Thus, zirconium doping of the Al–Ni alloy makes it possible to obtain a plastic metal base from nickel aluminides Al_3Ni_2, Al_3Ni and $Al_2(Ni,Zr)$ and complex-alloyed intermetallides with high hardness.

Keywords: Al–Ni alloy, Al–Ni–Zr alloy, structure formation, *X*-ray spectral microanalysis, microhardness, hardness, nickel aluminides, SHS metallurgy.

Acknowledgments: The research was carried out at the Center for Collective Use "Applied Materials Science" of the Federal State Budgetary Educational Institution of Higher Education "Pacific National University" with the financial support of the Ministry of Science and Education of the Russian Federation within the framework of research work No. AAAA-A20-120021490002-1 state registration of the state task.

For citation: Ri Kh., Ri E.Kh., Ermakov M.A., Kim E.D. Features of formation of the Al–Ni–Zr system alloy structure obtained by reducing oxide compounds by aluminothermy using SHS metallurgy. *Izvestiya. Non-Ferrous Metallurgy.* 2023;29(4):24–34.
https://doi.org/10.17073/0021-3438-2023-4-24-34

Особенности формирования структуры сплавов системы Al–Ni–Zr, полученных при восстановлении оксидных соединений алюмотермией с применением СВС-металлургии

Х. Ри, Э.Х. Ри, М.А. Ермаков, Е.Д. Ким

Тихоокеанский государственный университет
680035, Россия, г. Хабаровск, ул. Тихоокеанская, 136

✉ Евгений Давидович Ким (jenya_1992g@mail.ru)

Аннотация: Настоящая работа посвящена установлению закономерности влияния добавки циркония в количестве 2,21, 3,29, 3,69 и 6,92 мас.% на структурообразование, характер распределения элементов и микротвердость структурных составляющих

в сплавах системы Al–Ni–Zr, полученных алюмотермией с применением СВС-металлургии. Установлены и научно обоснованы закономерности формирования структурных составляющих и их микротвердости от содержания циркония в сплавах Al–Ni (50 мас.% Ni). Методами электронной микроскопии и микрорентгеноспектрального анализа элементов идентифицированы структурные составляющие. Структура исходного сплава состоит из алюминидов никеля Al_3Ni_2 (β′-фаза) и Al_3Ni. Легирование сплава цирконием в количестве 2,21 мас.% приводит к кристаллизации циркониевого алюминида никеля $Al_2(Ni,Zr)$. При дальнейшем увеличении содержания циркония (более 2,21 мас.%) кристаллизуются комплексно-легированные интерметаллидные соединения – алюминиды Zr, W, Si и цирконида Ni. Установлена закономерность снижения растворимости Ni в алюминидах никеля Al_3Ni_2 и Al_3Ni и их микротвердости по мере увеличения содержания циркония от 2,21 до 6,92 мас.% в сплавах Al–Ni–Zr. В алюминиде никеля с цирконием $Al_2(Ni,Zr)$ это способствует уменьшению растворимости Ni, Al и повышению концентраций Si и Zr. Легирование сплава Al–Ni цирконием в количестве более 2,21 мас.% способствует повышению твердости (*HRA*), несмотря на снижение микротвердости металлической основы (Al_3Ni_2, Al_3Ni и $Al_2(Ni,Zr)$). Основной причиной повышения твердости сплавов Al–Ni–Zr является кристаллизация комплексно-легированных интерметаллидов – алюминидов Zr, W, Si и цирконида никеля, обладающих, вероятно, повышенной микротвердостью. Таким образом, легирование сплава Al–Ni цирконием позволяет получить пластичную металлическую основу из алюминидов никеля Al_3Ni_2, Al_3Ni и $Al_2(Ni,Zr)$ и высокотвердые комплексно-легированные интерметаллиды.

Ключевые слова: сплав Al–Ni, сплав Al–Ni–Zr, структурообразование, микрорентгеноспектральный анализ, микротвердость, твердость, алюминиды никеля, СВС-металлургия.

Благодарности: Исследования проводились в ЦКП «Прикладное материаловедение» ФГБОУ ВО «Тихоокеанский государственный университет» при финансовой поддержке Министерства науки и образования Российской Федерации в рамках НИР № АААА-А20-120021490002-1 государственной регистарции государственного задания.

Для цитирования: Ри Х., Ри Э.Х., Ермаков М.А., Ким Е.Д. Особенности формирования структуры сплавов системы Al–Ni–Zr, полученных при восстановлении оксидных соединений алюмотермией с применением СВС-металлургии. *Известия вузов. Цветная металлургия*. 2023;29(4):24–34. https://doi.org/10.17073/0021-3438-2023-4-24-34

Introduction

The high oxidation resistance and thermal conductivity of nickel aluminide played a role in its selection as a material for high-temperature applications, especially in the aerospace, automotive and energy industries [1; 2]. In connection with recent research on fuel economy, the low density of this intermetallide is a huge added benefit. The intermetallic structure of NiAl promotes structural stability even at critically higher temperatures, which are of important engineering value. This is possible due to the special phase of the B2 structure which persists even to the melting point, making it ideal for high-temperature structural applications [3]. Unfortunately, a major obstacle to the versatile applicability of this intermetallide is its poor mechanical properties at room temperature, especially its ductility and fracture toughness. The lack of slip systems and the complexity of transferring them across grain boundaries have been identified as single "contributors" to the NiAl brittleness [4].

Various approaches to improve the restrictions of this intermetallide have been studied over the years. They are still being studied, in order to make the most of its versatility. Researchers have included ductile phases in the brittle system. They have also applied directional solidification pathways, refined grain sizes, studied heat treatment, added rare earth metals, and even recently integrated nanostructures into the NiAl matrices [5—10]. However, in the papers analyzed here, there is no information regarding doping of the Ni—Al system alloys with rare metals, such as Sc and Zr.

Meanwhile, the formation of coherent precipitates $L1_2$ was observed during aging in aluminum alloys with Sc [11; 12]. This showed high thermal stability, allowing the use of Al alloys with Sc at higher temperatures. The undesirable coarsening of phases was not identified in the structure which has a beneficial effect on strength increase at room temperature and heat treatment temperatures. Zirconium, while having a lower diffusion coefficient than scandium, also forms metastable coherent precipitate $L1_2$. The disadvantage of using Zr is in its even lower maximum solubility in Al than in Sc — only 0.078 at. % [12]. This limits the use of these alloying elements when implementing the traditional NiAl production technology.

The promising technology of self-propagating high-temperature synthesis (SHS), which has a number of economic advantages, can be a solution to the problem of obtaining NiAl [13]. This process allows the formation of reinforcing phases in the matrix alloy. The method is used to synthesize nickel aluminides which are the metal matrix in modern functional materials. A high temperature of endogenous processes makes it possible to obtain cast composite alloys according to a short flow diagram [14—21].

The use of high-temperature reduction processes for refractory metal oxides seems economically feasible [21—24]. The present study is a continuation of work [22] in which the Zr content in the Al—Ni—Zr alloy ranged from 0 to 3.52 wt.%.

Thus, the objective of this work was to obtain zirconium-doped nickel aluminides by their synthesis from nickel oxide compounds and baddeleyite concentrate from the Far East region by the SHS metallurgy method. Another objective was to study the effect of zirconium on structure formation, liquation processes and microhardness of structural components of the Al—Ni—Zr system alloy.

Methods and materials

The initial substances for the charge were:
— NiO (99.5 wt.%, TU 6-09-3642-74, OSCH 10-2);
— baddeleyite concentrate (Table 1);
— calcium fluoride CaF_2 (98.0 wt.%, TU 2621-007-69886968-2015 with amendment 1);
— $NaNO_3$ (C.P., GOST 4168-79);
— aluminum powder (98.0 wt.%, PA-4, GOST 6058-73).

The composition of the charge in fractional parts was as follows: Al : NiO : CaF_2 : $NaNO_3$: $ZrSiO_4$ = = 10 : 10 : 12 : 6 : X, where X = 1.5, 2.0, 2.5, 5.0 and 8.0 of $ZrSiO_4$ fractional parts.

Metallothermic smelting was carried out in heat-resistant metal crucibles lined with refractory material. The charge was prepared by mixing a 50 g weighed portion with ∅ 40 mm grinding balls in a Pulverisette3 planetary mill (Fritch, Germany). This is a sealed 0.5 L container, at a speed of 500 rpm for 15—20 min. The experiment was carried out in the open air. The charge was ignited at a bulk mass after vibration compaction. The reaction was initiated with an electric igniter from above. Then the reaction proceeded without external heating. As a result of smelting, 2 layers of products in the form of metallic and slag phases were formed. They were separated due to gravity separation and the presence of calcium fluoride in the charge, acting as a flux.

In order to determine the regularity and average the results obtained, 5 melts were carried out for each concentration of the baddeleyite concentrate.

Within the context of this work, samples with the size of the studied surface of about 1.5 cm^2 and 5 to 10 mm high were used. Marking was done with a permanent marker. In order to study the uniformity of element distribution in volume, the surface of the cross section was treated. The samples were fixed by hot pouring into the Rose's alloy. Abrasive grinding with abrasive paper on a rotating wheel was used with decreasing the grain size after each treatment.

In order to ensure a higher quality of the examined surface, abrasive polishing with a felt cloth on a rotating wheel and chromium oxide-based abrasive pastes with different abrasive particle sizes ranging from 9 to 1 μm were used. Ultrasonic cleaning in acetone medium was applied, in order to remove polishing products and other contaminants from the surface of the samples.

The following modern methods of research were used:

— *X*-ray phase analysis of alloys using a DRON-7 diffractometer;

— *X*-ray spectral microanalysis to determine the content of elements in different structural components of the alloys — on an analytical research complex based on FE-SEM SU-70 (Hitachi, Japan) with energy dispersive (Thermo Scientific Ultra Dry) and wave (Thermo Scientific Magna Ray) attachments;

— microhardness tests (H_{50}) by the standard method on the HMV-G21DT device (Shimadzu, Japan);

— assessment of porosity by hydrostatic weighing on AUW-220D analytical scales (Shimadzu, Japan);

— hardness tests by the standard *HRA* method on a Metolab 100 hardness tester (Russia).

Main results and their discussion

The alloy synthesis proceeds through the stage of reduction of the initial zirconium and nickel oxides, accompanied by the formation of intermetallides and can be summarized, with a certain degree of approximation, by the following equations of chemical reactions [13]:

$$^3/_4\,ZrO_2 + Al = {}^3/_4\,Zr + {}^1/_2\,Al_2O_3, \quad (1)$$

$$3Al + Zr = Al_3Zr, \quad (2)$$

Table 1. **Composition of baddeleyite concentrate, wt.%**
Таблица 1. Состав бадделеитового концентрата, мас.%

ZrO_2	CaO	SiO_2	Fe_2O_3	P_2O_5	TiO_2	WO_3	Impurities
72.83	0.86	10.28	0.89	10.19	0.25	2.35	1.35

$$3NiO + 2Al = 3Ni + Al_2O_3, \quad (3)$$

$$4Al + W = Al_4W. \quad (4)$$

The values of the Gibbs energy are ΔG_{1000K} = = –39 kJ/mol for reaction (1), –28 kJ/mol (2), –105 kJ/mol (3) and –254 kJ/mol (4).

The effect of variable zirconium content on structure formation and the nature of element distribution in structural components of the Al—Ni alloy (50 wt.% Ni) obtained by the SHS metallurgy method was studied. In all synthesized ingots, the vertical sections in the lower half showed a dense structure without pores, and in the upper half the porosity was about 20 %.

The diffraction patterns of all alloys (Fig. 1) have the same character and set of peaks. The difference is noticeable in the relative intensity of reflexes. This probably indicates unequal crystallization processes and the preferential growth along certain atomic planes. The $NiAl_3$ phase was identified. No compounds with zirconium were detected, due to the low concentrations of this metal in the initial mixture.

The following structural components are formed in the initial alloy during crystallization in the SHS process (Fig. 2). Nickel aluminide Al_3Ni_2 represents a β′-phase — solid solution of Ni in AlNi, located in the area to the left of the singular crystallization point of AlNi. Its crystals have a lighter hue and are multifaceted in the form of grains. The Al_3Ni crystals have a gray hue and occupy the main area in the thin section.

Figure 3 presents the microstructure and points of analysis in structural components of the Al—Ni—Zr alloy samples which contain 2.21, 3.29, 3.69 and 6.92 wt.% of zirconium. As its content increases, the alloy structure becomes more complex with a decrease in the total volume ratio of the Al_3Ni matrix alloy, and an increase in the density of reinforcing intermetallide phases with zirconium.

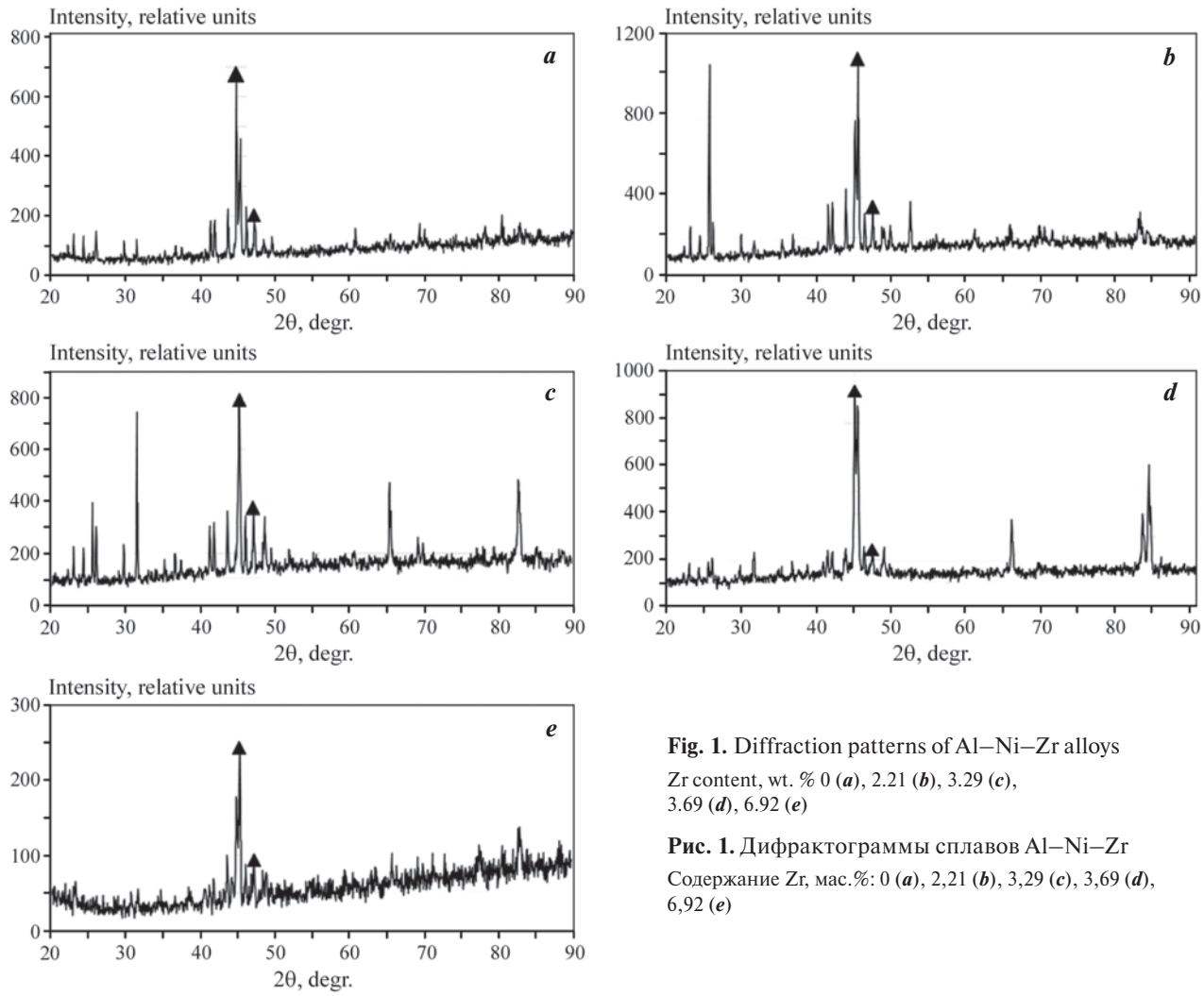

Fig. 1. Diffraction patterns of Al–Ni–Zr alloys
Zr content, wt. % 0 (***a***), 2.21 (***b***), 3.29 (***c***), 3.69 (***d***), 6.92 (***e***)

Рис. 1. Дифрактограммы сплавов Al–Ni–Zr
Содержание Zr, мас.%: 0 (***a***), 2,21 (***b***), 3,29 (***c***), 3,69 (***d***), 6,92 (***e***)

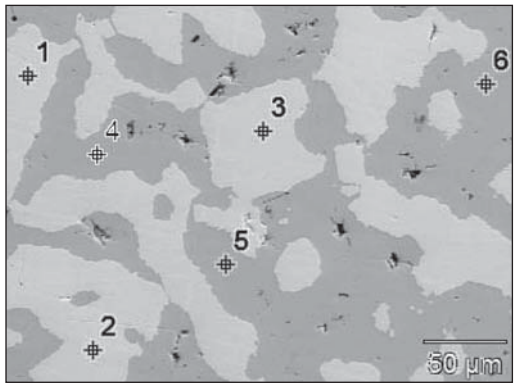

Points of analysis of the elements	Structural components	Content, at.%	
		Al	Ni
1–3	Al_3Ni_2	61.15	38.85
		$Al_{61.15}Ni_{38.95} = Al_{1.57}Ni = Al_{3.14}Ni_2 \approx Al_3Ni_2$	
4–6	Al_3Ni	74.56	25.44
		$Al_{74.56}Ni_{25.44} = Al_{2.43}Ni \approx Al_3Ni$	

Fig. 2. Microstructure and element distribution in structural components of the Al–Ni alloy

Рис. 2. Микроструктура и распределение элементов в структурных составляющих сплава Al–Ni

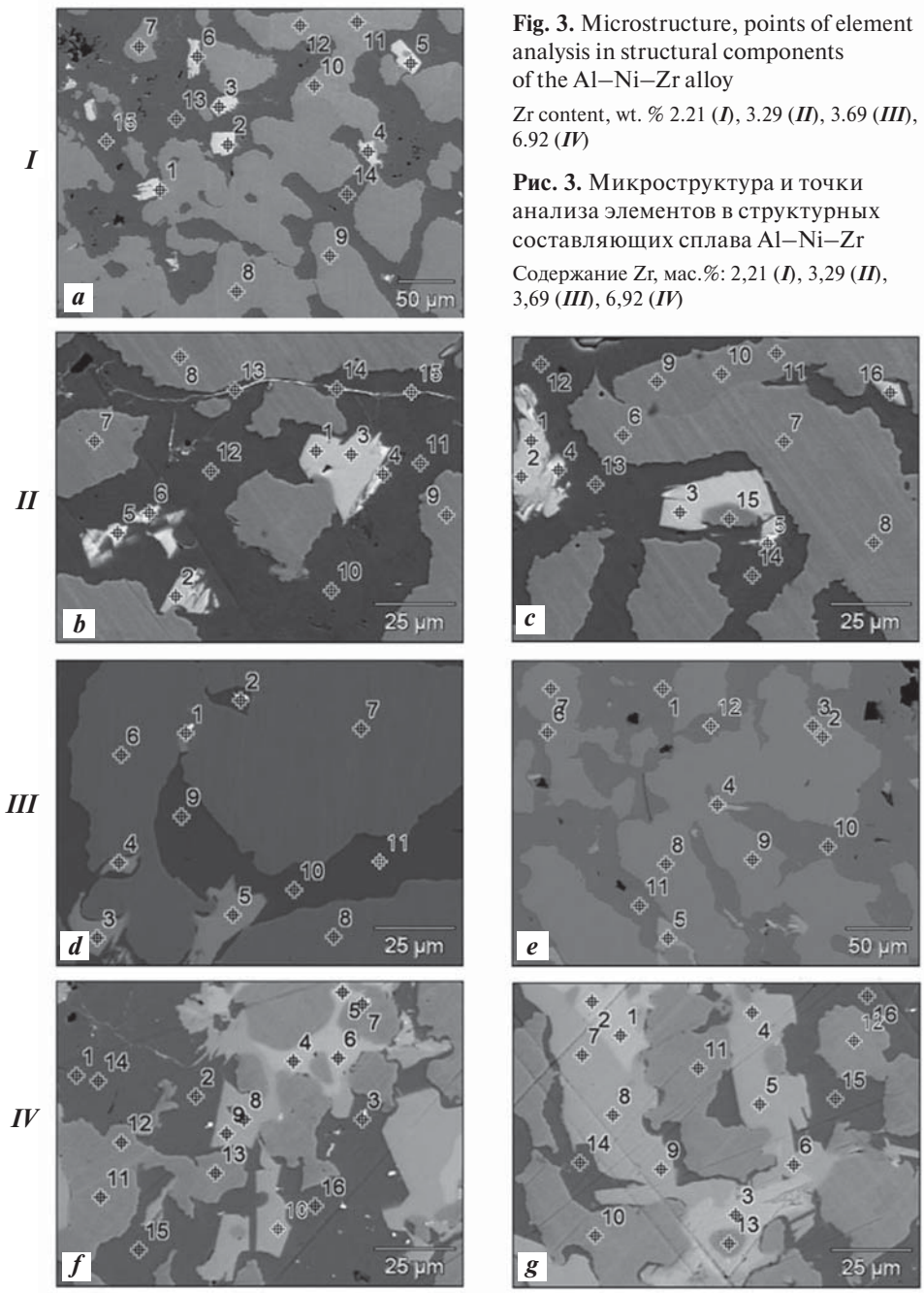

Fig. 3. Microstructure, points of element analysis in structural components of the Al–Ni–Zr alloy

Zr content, wt. % 2.21 (***I***), 3.29 (***II***), 3.69 (***III***), 6.92 (***IV***)

Рис. 3. Микроструктура и точки анализа элементов в структурных составляющих сплава Al–Ni–Zr

Содержание Zr, мас.%: 2,21 (***I***), 3,29 (***II***), 3,69 (***III***), 6,92 (***IV***)

Table 2. **Effect of zirconium additive on the content of elements (at.%) in structural components of the Al–Ni alloy and their distribution**

Таблица 2. Влияние добавки циркония на содержание элементов (ат.%) в структурных составляющих сплава Al–Ni и их распределение

Figure	Zr, wt.%	Al_3Ni_2 or β′-phase	Al_3Ni	Al_2(Ni, Zr)	Al_2(Ni, Zr, V, Hf, Ti)	Al_3(Zr, Ni, W, V, Ti, Fe)	Zr_4(Al, Ni, Hf, Ti)	Zr_3(Al, Ni, Hf, Ti)	Al(Si, Ni, V, Mn, Cr, W)
2	0	61.15 Al 38.85 Ni (*1–3*)	74.56 Al 25.44 Ni (*4–6*)	–	–	–	–	–	–
3, *I*	2.21	61.68 Al 38.3 Ni (*7–12*, *a*)	75.23 Al 24.77 Ni (*13–15*, *a*)	67.78 Al 19.46 Ni 12.76 Zr (*1–6*, *a*)	–	–	–	–	–
3, *II*	3.29	61.0 Al 39.0 Ni (*7–9*, *b* and *6–11*, *c*)	74.4 Al 25.6 Ni (*10–12*, *b* and *12–14*, *c*)	66.85 Al 21.79 Ni 13.3 Zr (*1–3*, *b* and *c*)	64.6 Al 21.79 Ni 0.6 Ti, 0.75 V 0.7 Hf (*13–15*, *b*)	72.6 Al 4.05 Ni 0.28 Ti 0.835 V 21.19 Zr 0.32 Fe 1.0 W (*4–6*, *b* and *4–5*, *c*)	–	–	–
3, *III*	3.69	62.37 Al 37.63 Ni (*6–8*, *d* and *7–9*, *e*)	75.53 Al 24.47 Ni (*9–11*, *d* and *10–12*, *e*)	66.7 Al 19.3 Ni 13.24 Zr 0.78 Ti (*3–5*, *d* and *4–6*, *e*)	–	–	9.01 Al 7.92 Ni 0.94 Ti 79.27 Zr 2.93 Hf (*1*, *d* and *2–3*, *e*)	25.6 Al 11.45 Ni 0.56 Ti 59.76 Zr 2.63 Hf (*2*, *d* and *1*, *e*)	–
3, *IV*	6.92	62.5 Al 35.63 Ni 1.83 Si (*11–13*, *f* and *10–13*, *g*)	76.85 Al 22.87 Ni 0.25 Si (*14–16*, *f* and *g*)	65.0 Al 18.62 Ni 13.49, 2.87 Si (*4–6*, *f* and *1–3*, *g*)	–	52.56 Al 17.34 Ni 28.41 Zr 1.43 Hf 0.26 Ti (*1*, *f*)	–	–	39.06 Al 9.37 Ni 0.97 Cr 3.85 V 30.5 Si 0.75 Fe 1.0 Mn 12.95 W (*2–3*, *f*)

Note. The analysis points shown in Fig. 2 and 3 are given in brackets.

Table 2 shows the elementary and phase compositions of structural components of the synthesized alloys. As can be seen, the $NiAl_3$ and Ni_2Al_3 phases have been identified in all samples. Zirconium alloying complicates the phase composition of the alloy: the Al_2(Ni, Zr) phase is formed in all the samples, and with an increase in the zirconium additive over 2.21 wt.% — Al_2(Ni, Zr, V, Hf, Ti), Al_3(Zr, Ni, W, V, Ti, Fe), Zr_4(Al, Ni, Hf, Ti), Zr_3(Al, Ni, Hf, Ti) and Al(Si, Ni, V, Mn, Cr, W) are formed.

Figure 4, *a* shows that the increasing zirconium content in the Al—Ni alloy contributes to the extreme change in hardness with its minimum value at 2.21 wt.% Zr. In order to identify the reasons for this, the effect of zirconium on the microhardness of the Al_3Ni_2, Al_3Ni and Al_2(Ni,Zr) structural components was studied.

It was found that the Al_3Ni_2 (β′-phase) and Al_3Ni microhardness monotonically decreases to 6.92 wt.% Zr (see Fig, 4, *b*). This is due to the reduction of nickel solubility as the zirconium concentration increases (Fig. 4, *c—d*). The Al_2(Ni,Zr) compound has an increased zirconium content in addition to the low nickel content (Fig. 4, *e*). Moreover, their total Ni + Zr amount

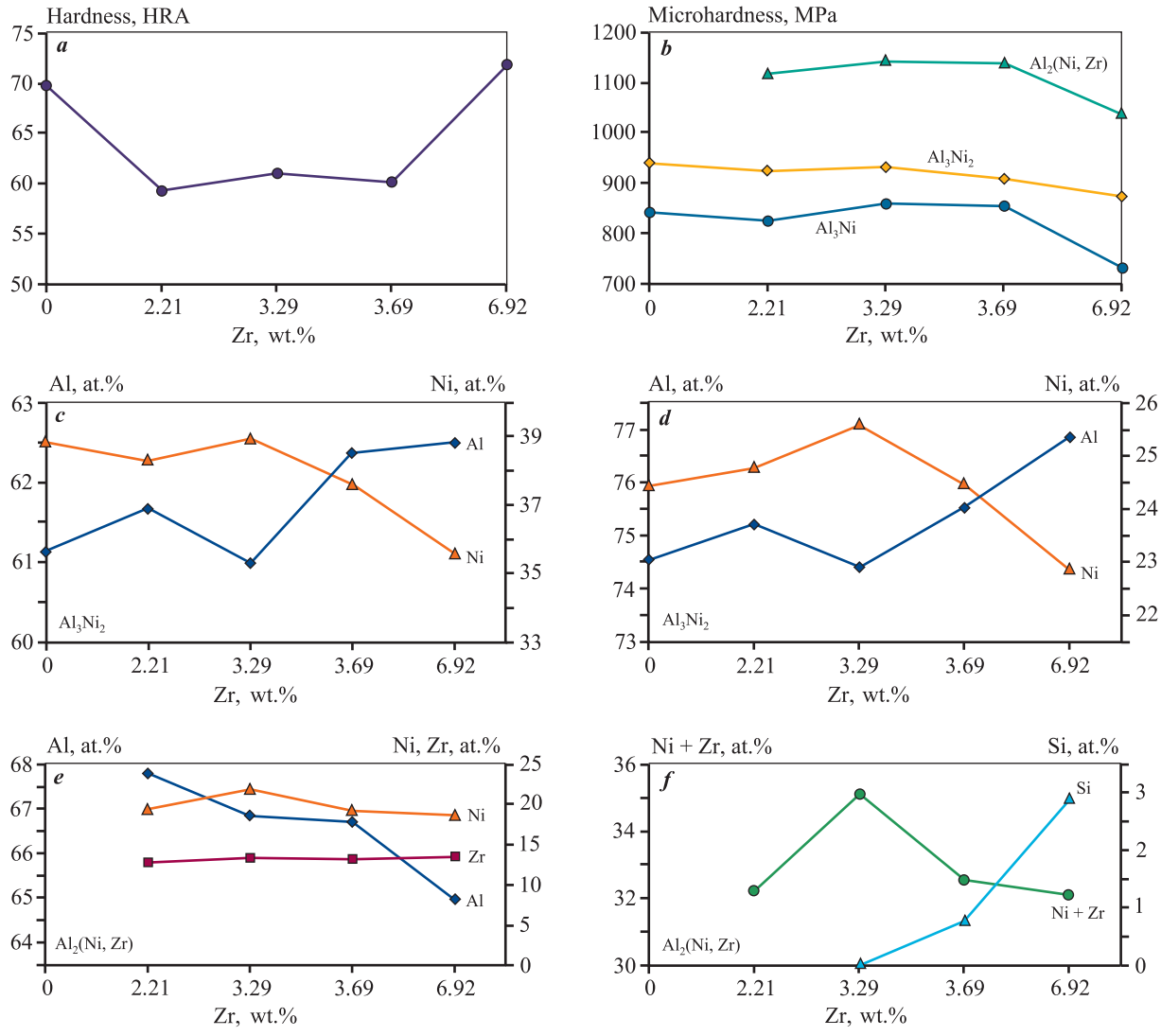

Fig. 4. Effect of zirconium on the composition and microhardness of nickel aluminides in Al–Ni alloys

a – hardness, ***b*** – microhardness of matrix phases, ***c*** – Al and Ni in Al_3Ni_2, ***d*** – Al and Ni in Al_3Ni_2, ***e*** – Al, Ni, Si in Al_2(Ni,Zr), ***f*** – Ni + Zr and Si in Al_2(Ni,Zr)

Рис. 4. Влияние циркония на состав и микротвердость алюминидов никеля в сплавах Al–Ni

a – твердость, ***b*** – микротвердость матричных фаз, ***c*** – Al и Ni в Al_3Ni_2, ***d*** – Al и Ni в Al_3Ni_2, ***e*** – Al, Ni, Si в Al_2(Ni, Zr), ***f*** – Ni + Zr и Si в Al_2(Ni, Zr)

decreases, and the concentration of silicon in $Al_2(Ni,Zr)$ increases significantly (Fig. 4, *f*).

Thus, the microhardness of Al_3Ni_2, Al_3Ni and $Al_2(Ni,Zr)$ decreases as the zirconium content in the Al—Ni alloy increases because the solubility of Ni and Ni+Zr decreases.

The main reason for increasing the hardness of the Al—Ni—Zr system alloys during alloying with 2.21—6.92 wt.% Zr is the crystallization of additional intermetallide compounds (Zr, W, Si aluminides and nickel zirconides) possessing high microhardness (Table 3).

Table 3. **Crystallization of intermetallide compounds depending on the content of zirconium in Al–Ni–Zr alloys**

Таблица 3. Кристаллизация интерметаллидных соединений в зависимости от содержания циркония в сплавах Al–Ni–Zr

Zr, wt.%	Compound	Composition, at.%
3.29	Al_3(Zr, Ni, W, V, Ti, Fe)	72.6 Al 4.05 Ni 0.28 Ti 0.835 V 21.19 Zr 0.32 Fe 1.0 W
3.29	Al_2(Zr, Ni, V, Hf, Ti)	64.6 Al 21.79 Ni 11.55 Zr 0.6 Ti 0.75 V 0.7 Hf
3.69	Zr_4(Al, Ni, Hf, Ti)	9.01 Al 7.92 Ni 0.94 Ti 79.27 Zr 2.93 Hf
3.69	Zr_3(Al, Ni, Hf, Ti)	25.6 Al 11.45 Ni 0.56 Ti 59.76 Zr 2.63 Hf
6.92	Al_2(Si, W, Ni, V, Ti, Mn)$_3$	39.06 Al 9.37 Ni 0.97 Cr 3.85 V 30.5 Si 0.75 Fe 1.0 Mn 12.95 W 1.58 Ti
6.92	Al(Zr, Ni, Hf, Ti)	52.56 Al 17.34 Ni 28.41 Zr 1.43 Hf 0.26 Ti

The main reason for increasing the hardness of the Al—Ni—Zr system alloys during alloying with 2.21—6.92 wt.% Zr is the crystallization of additional intermetallide compounds (Zr, W, Si aluminides and nickel zirconides) possessing high microhardness (Table 3).

Thus, by doping the Al—Ni alloy with zirconium (more than 2.21 wt.%), it is possible to obtain a plastic metal base of Al_3Ni_2, Al_3Ni, $Al_2(Ni,Zr)$ and high-hardness intermetallide phases of Al_2(Ni, Zr, V, Hf, Ti), Al_3(Zr, Ni, W, V, Ti, Fe), Zr_4(Al, Ni, Hf, Ti), Zr_3(Al, Ni, Hf, Ti), Al(Si, Ni, V, Mn, Cr, W) which increase the hardness of the Al—Ni—Zr system alloy.

Conclusion

1. The structural components in alloys of the Al—Ni—Zr system containing 2.21, 3.29, 3.69 and 6.92 wt.% Zr have been identified by electron-microscopic studies and *X*-ray spectral microanalysis of elements.

2. Regardless of the zirconium content, Al_3Ni_2 (β′-phase), Al_3Ni and $Al_2(Ni,Zr)$ crystallize in the Al—Ni—Zr alloy. In addition to these, various intermetallide compounds differing in stoichiometry and chemical composition crystallize in the alloy studied. They include zirconium, tungsten, silicon aluminides and nickel zirconide.

3. The solubility of nickel in Al_3Ni_2 (β′-phase) and Al_3Ni, as well as nickel with zirconium in $Al_2(Ni,Zr)$ has been found to change with increasing zirconium content in the Al—Ni—Zr alloy:

— the amount of nickel in Al_3Ni_2 and Al_3Ni decreases;

— the concentrations of Ni, Al and Ni + Zr in $Al_2(Ni,Zr)$ decrease;

— the silicon content increases on the contrary.

4. The regularity of Al_3Ni_2, Al_3Ni and $Al_2(Ni,Zr)$ microhardness decrease depending on the zirconium content in the Al—Ni—Zr alloy has been established.

5. Doping of the Al—Ni alloy with zirconium (more than 2.21 wt.%) promotes increase of hardness in spite of decrease of microhardness of the Al_3Ni_2, Al_3Ni and $Al_2(Ni,Zr)$ metal base.

6. The main reason for increasing the hardness of Al—Ni—Zr alloys is the crystallization of complex intermetallide phases — Zr, W, Si aluminides and Ni zirconides. Thus, the structure corresponding to the Charpy principle is confirmed.

7. Due to the structure developed and phase composition, as well as the increased hardness, it can be assumed that the alloys with the addition of 6.92 wt.% Zr are the most heat-resistant and wear-resistant of the synthesized alloys. This in turn, can be used in the conditions of increased wear and high temperatures.

References

1. Wu D.L., Dahl K.V., Christiansen T.L., Montgomery M., Hald J. Corrosion behaviour of Ni and nickel aluminide coatings exposed in a biomass fired power plant for two years. *Surface and Coatings Technology*. 2019;(362):355—365. https://doi.org/10.1016/j.surfcoat.2018.12.129
2. Dey G.K. Physical metallurgy of nickel aluminides. *Sadhana*. 2003;1(28):247—262. https://doi.org/10.1007/BF02717135
3. Talaş Ş. Nickel aluminides. In: *Intermetallic Matrix Composites*. Woodhead Publishing, Sawston, 2018. P. 37—69. https://doi.org/10.1016/B978-0-85709-346-2.00003-0
4. Baker I., Munroe P.R. Improving intermetallic ductility and toughness. *Journal of Metals*. 1988;2(40):28—31. https://doi.org/10.1007/BF03258828
5. Shang Z., Shen J., Wang L., Du Y., Xiong Y., Fu H. Investigations on the microstructure and room temperature fracture toughness of directionally solidified NiAl—Cr(Mo) eutectic alloy. *Intermetallics*. 2015;57:25—33. https://doi.org/10.1016/j.intermet.2014.09.012
6. Stoloff N. S., Koch C.C., Liu C.T., Izumi O. High-temperature ordered intermetallic alloys II. In: *Materials Research Society Proceedings of the Second Symposium* (Boston, MA, Dec. 2—4, 1986.). Troy, NY (USA): Rensselaer Polytechnic Inst., 1987. P. 3—11. https://doi.org/10.1557/PROC-81-3
7. Ponomareva A.V., Vekilov Y.K., Abrikosov I.A. Effect of Re content on elastic properties of B2 NiAl from ab initio calculations. *Journal of Alloys and Compounds*. 2014;586:274—278. https://doi.org/10.1016/j.jallcom.2012.12.103
8. Bochenek K., Basista M. Advances in processing of NiAl intermetallic alloys and composites for high temperature aerospace applications. *Progress in Aerospace Sciences*. 2015;79:136—146. https://doi.org/10.1016/j.paerosci.2015.09.003
9. Ameri S., Sadeghian Z., Kazeminezhad I. Effect of CNT addition approach on the microstructure and properties of NiAl—CNT nanocomposites produced by mechanical alloying and spark plasma sintering. *Intermetallics*. 2016;76:41—48. https://doi.org/10.1016/j.intermet.2016.06.010
10. Gostishchev V., Ri E., Ri H., Kim E., Ermakov M., Khimukhin S., Deev V., Prusov E. Synthesis of complex-alloyed nickel aluminides from oxide compounds by aluminothermic method. *Metals*. 2018;6(8):439. https://doi.org/10.3390/met8060439
11. Röyset J., Ryum N. Scandium in aluminium alloys. *International Materials Reviews*. 2005;1(50):19—44. https://doi.org/10.1179/174328005X14311
12. Michi R.A., Plotkowski A., Shyam A., Dehoff R.R., Babu S.S. Towards high-temperature applications of aluminium alloys enabled by additive manufacturing. *International Materials Reviews*. 2022;67(3):298—345. https://doi.org/10.1080/09506608.2021.1951580
13. Prusov E.S., Panfilov A.A., Kechin V.A. Role of powder precursors in production of composite alloys using liquid-phase methods. *Russian Journal of Non-Ferrous Metals*. 2017;58(3):308—316. https://doi.org/10.3103/S1067821217030154
14. Sanin V., Andreev D., Ikornikov D., Yukhvid V. Cast intermetallic alloys by SHS under high gravity. *Acta Physica Polonica A*. 2011;120(2):331—335. https://doi.org/10.12693/APhysPolA.120.331
15. Amosov A.P., Luts A.R., Latukhin E.I., Ermoshkin A.A. Application of SHS processes for in situ production of aluminum matrix composite materials discretely reinforced with titanium carbide nanoparticles. Review. *Russian Journal of Non-Ferrous Metals*. 2016;57(2):106—112. https://doi.org/10.3103/S1067821216020024
Амосов А.П., Луц А.Р., Латухин Е.И., Ермошкин А.А. Применение процессов СВС для получения *in situ* алюмоматричных композиционных материалов, дискретно армированных наноразмерными частицами карбида титана. Обзор. *Известия вузов. Цветная металлургия*. 2016;(1):39—49. https://doi.org/10.17073/0021-3438-2016-1-39-49
16. Tiwary C., Gunjal V., Banerjee D., Chattopadhyay K. Intermetallic eutectic alloys in the Ni—Al—Zr system with attractive high temperature properties. *MATEC Web of Conferences. — EDP Sciences*. 2014;14:01005. https://doi.org/10.1051/matecconf/20141401005
17. Fukumoto M., Yokota T., Hara M. Formation of Ni aluminide containing Zr by synchronous electrodeposition of Al and Zr and cyclic-oxidation resistance. *Journal of the Japan Institute of Metals*. 2010;74(9):584—591.

18. Wang L., Yao Ch., Shen J., Zhang Yu. Microstructures and compressive properties of NiAl—Cr (Mo) and NiAl—Cr eutectic alloys with different Fe contents. *Materials Science and Engineering: A.* 2019;744:593—603. https://doi.org/10.1016/j.msea.2018.12.085
19. Levashov E.A. Promising materials and technologies for self-propagating high-temperature synthesis. Moscow: Izdatelskii dom "MISIS", 2011. 377 p. (In Russ.).
Левашов Е.А. Перспективные материалы и технологии самораспространяющегося высокотемпературного синтеза. М.: Изд. дом МИСИС, 2011. 377 с.
20. Hassan A.I., El-Fawakhry M.K., Hamed A., Mattar T. Monitoring the effect of alloying elements segregation in Fe Mn Ni Al high entropy alloy. *Journal of Physics: Conference Series.* 2022;2368(1):012010.1—7. https://doi.org/10.1088/1742-6596/2368/1/012010
21. Khimukhin S.N., Kim E.D., Ri E.H. Synthesis of NiAl composite alloys by metallothermy method. *Materials Today: Proceedings.* 2019;19:2278—2282. https://doi.org/10.1016/j.matpr.2019.07.597
22. Ri E.Kh., Ri Kh., Kim E.D., Ermakov M.A. The structure, segregation and microhardness of the structural components of the Al—Ni—Zr alloys synthesized from nickel oxide NiO and brazilite concentrate by means of SHS metallurgy. *Tsvetnye Metally.* 2021;(7):58—64. (In Russ.). https://doi.org/10.17580/tsm.2021.07.07
Ри Э.Х., Ри Хосен, Ким Е.Д., Ермаков М.А. Структурообразование, ликвационные процессы и микротвердость структурных составляющих сплавов Al—Ni—Zr, синтезированных из оксида никеля NiO и бадделеитового концентрата методом СВС-металлургии. *Цветные металлы.* 2021;(7):58—64. https://doi.org/10.17580/tsm.2021.07.07
23. Agafonov S.N., Krasikov S.A., Ponomarenko A.A., Ovchinnikov L.A. Phase Formation in the Aluminothermic Reduction of ZrO_2. *Inorganic Materials.* 2012;48(8):813—820. https://doi.org/10.1134/S0020168512070011
Агафонов С.Н., Красиков С.А., Пономаренко А.А., Овчинников Л.А. Фазообразование при алюмотермическом восстановлении ZrO_2. *Неорганические материалы*. 2012;48(8):927—927.
24. Bazhin V.Y., Kosov Y.I., Lobacheva O.L., Dzhevaga N.V. Synthesis of aluminum-based scandium—yttrium master alloys. *Russian Metallurgy (Metally).* 2015;(7):516—520. https://doi.org/10.1134/S0036029515070034

Information about the authors

Khosen Ri – Dr. Sci. (Eng.), Professor, Department of Foundry and Metal Technology, Pacific State University.
https://orcid.org/0000-0001-7633-8989
E-mail: opirus@list.ru

Ernst Kh. Ri – Dr. Sci. (Eng.), Professor, Head of the Department of Foundry and Metal Technology, Pacific State University.
https://orcid.org/0000-0001-7784-1252
E-mail: erikri999@mail.ru

Mikhail A. Ermakov – Cand. Sci. (Eng.), Associate Professor, Department of Foundry and Metal Technology, Pacific State University.
https://orcid.org/0000-0001-6525-2004
E-mail: ermakovma@yandex.ru

Evgeniy D. Kim – Cand. Sci. (Eng.), Lecturer, Department "Foundry and Technology of Metals", Pacific State University.
https://orcid.org/0000-0002-0175-0503
E-mail: jenya_1992g@mail.ru

Информация об авторах

Хосен Ри – д.т.н., профессор кафедры «Литейное производство и технология металлов», Тихоокеанский государственный университет (ТОГУ).
https://orcid.org/0000-0001-7633-8989
E-mail: opirus@list.ru

Эрнст Хосенович Ри – д.т.н., профессор, зав. кафедрой «Литейное производство и технология металлов», ТОГУ.
https://orcid.org/0000-0001-7784-1252
E-mail: erikri999@mail.ru

Михаил Александрович Ермаков – к.т.н, доцент кафедры «Литейное производство и технология металлов», ТОГУ.
https://orcid.org/0000-0001-6525-2004
E-mail: ermakovma@yandex.ru

Евгений Давидович Ким – к.т.н., преподавтель кафедры «Литейное производство и технология металлов», ТОГУ.
https://orcid.org/0000-0002-0175-0503
E-mail: jenya_1992g@mail.ru

Contribution of the authors

Kh. Ri – formation of the main concept, goal and objectives of the study, preparation of the text, formulation of conclusions.

E.Kh. Ri – conducting the calculations, analysis of the research results.

M.A. Ermakov – provision of the resources, testing the samples, formulation of the conclusions.

E.D. Kim – coconducting the calculations, preparation and management of the experiment, conducting the experiments, writing the text.

Вклад авторов

Х. Ри – формирование основной концепции, постановка цели и задачи исследования, подготовка текста, формулировка выводов.

Э.Х. Ри – проведение расчетов, анализ результатов исследований.

М.А. Ермаков – обеспечение ресурсами, проведение испытаний образцов, формулировка выводов.

Е.Д. Ким – осуществление расчетов, подготовка эксперимента, проведение экспериментов, подготовка текста статьи.

The article was submitted 06.12.2022, revised 02.05.2023, accepted for publication 19.05.2023

Статья поступила в редакцию 06.12.2022, доработана 02.05.2023, подписана в печать 19.05.2023

UDC 669.2/.8.017
https://doi.org/10.17073/0021-3438-2023-4-35-47

Research article
Научная статья

Improvement of selective laser melting regimes for the fabrication of Ti–6Al–4V porous structures for medical applications

V.A. Sheremetyev[1], V.D. Lezin[1], M.V. Kozik[1], S.A. Molchanov[2]

[1] **National University of Science and Technology "MISIS"**
4 bld. 1 Leninskiy Prosp., Moscow 119049, Russia

[2] **LLC "Conmet"**
24/1 Onezhskaya Str., Moscow 125413, Russia

✉ Vadim A. Sheremetyev (vadim.sheremetyev@gmail.com)

Abstract: This article describes approaches to the optimization of regimes of selective laser melting (SLM) used in the fabrication of porous materials from medical grade Ti–6Al–4V alloy with thin structural elements and a low level of defect porosity. Improved fusion of thin elements based on SLM regimes is achieved due to a significant decrease in the distance between laser passes (from 0.11 to 0.04–0.05 mm). Moreover, the balance between the laser energy density and building rate is compensated by changing the laser speed and laser power. The results of the study of defect porosity and hardness of samples fabricated according to experimental SLM regimes allowed three promising sets of parameters to be defined. One was selected for studying mechanical properties in comparison with the reference SLM regime. In the aims of this study, the samples were developed and fabricated using the structures of rhombic dodecahedron and Voronoi types with a porosity of 70–75 %. The decrease in defect porosity was established at ≈1.8 % to 0.6 %, depending on the SLM regime. This promotes a significant increase in strength properties of the material, including an increase in the yield strength of rhombic dodecahedron from 76 to 132 MPa and the Voronoi structure from 66 to 86 MPa. The low Young module (1–2 GPa) remains, corresponding to the rigidity level of spongy bone tissue.

Keywords: selective laser melting, titanium alloys, porous structures, microstructure, porosity, mechanical properties.

Acknowledgements: This work was supported by Grant No. 22-79-10299 of the Russian Science Foundation, https://rscf.ru/project/22-79-10299/

For citation: Sheremetyev V.A., Lezin V.D., Kozik M.V., Molchanov S.A. Improvement of selective laser melting regimes for the fabrication of Ti–6Al–4V porous structures for medical applications. *Izvestiya. Non-Ferrous Metallurgy.* 2023;29(4):35–47.
https://doi.org/10.17073/0021-3438-2023-4-35-47

Совершенствование режима селективного лазерного плавления для изготовления пористых структур из сплава Ti–6Al–4V медицинского назначения

В.А. Шереметьев[1], В.Д. Лезин[1], М.В. Козик[1], С.А. Молчанов[2]

[1] **Национальный исследовательский технологический университет «МИСИС»**
Россия, 119049, г. Москва, Ленинский пр-т, 4, стр. 1

[2] **ООО «Конмет»**
Россия, 125413, г. Москва, ул. Онежская, 24/1

✉ Вадим Алексеевич Шереметьев (vadim.sheremetyev@gmail.com)

Аннотация: Разработаны подходы к оптимизации режима селективного лазерного плавления (СЛП) для получения пористых материалов из сплава Ti–6Al–4V медицинского назначения с тонкими конструкционными элементами и низким уровнем дефектной

пористости. Улучшенное проплавление тонких элементов с применением разработанных экспериментальных режимов СЛП достигается за счет значительного снижения расстояния между проходами лазера (с 0,11 до 0,04–0,05 мм), а баланс между плотностью энергии лазера и скоростью построения скомпенсирован путем изменения скорости пробега и мощности лазера. Результаты изучения дефектной пористости и твердости образцов, изготовленных по экспериментальным режимам СЛП, позволили установить 3 наиболее перспективных набора параметров, один из которых выбран для исследования механических свойств в сравнении со стандартным режимом СЛП. Для этого исследования разработаны и изготовлены образцы на основе структур типа ромбического додекаэдра и полиэдра Вороного пористостью 70–75 %. Установлено, что снижение уровня дефектной пористости с ≈1,8 % до 0,6 %, обеспеченное применением разработанного режима СЛП, способствует значительному повышению прочностных характеристик материала. Увеличение условного предела текучести ромбического додекаэдра с 76 до 132 МПа и Вороного с 66 до 86 МПа. При этом сохраняется низкий модуль Юнга (1–2 ГПа), соответствующий уровню жесткости губчатой костной ткани.

Ключевые слова: селективное лазерное плавление, титановые сплавы, пористые структуры, микроструктура, пористость, механические свойства.

Благодарности: Работа выполнена за счет гранта Российского научного фонда № 22-79-10299, https://rscf.ru/project/22-79-10299/

Для цитирования: Шереметьев В.А., Лезин В.Д., Козик М.В., Молчанов С.А. Совершенствование режима селективного лазерного плавления для изготовления пористых структур из сплава Ti–6Al–4V медицинского назначения. *Известия вузов. Цветная металлургия.* 2023;29(4):35–47. https://doi.org/10.17073/0021-3438-2023-4-35-47

Introduction

Selective laser melting (SLM), consisting of layer-by-layer melting of a metal powder under the impact of a moving laser beam, has become widespread in the production of medical implants and tools. This is due to the rapid transition to manufacturing, greater freedom in product design, and the high accuracy of their geometry. Standardized medical alloys Ti—6Al—4V, Ti—6Al—7Nb are widely employed [1; 2] in the manufacture of implants using the SLM method. This also includes as Ti—Ni, Ti—Zr—Nb shape memory alloys for medical purposes [3; 4].

In the medical industry, the advantage of SLM over traditional manufacturing methods, in addition to manufacturing individual implants, also lies in the possibility of obtaining porous structures with a given geometry and cell size. The use of porous structures arises from the necessity to simulate the structure of bone tissue and its properties (Young's modulus, compressive strength, biological compatibility, tendency to bone tissue ingrowth) [5]. The ingrowth of bone tissue into the implant is one of the most important properties, and provides a reliable mechanical connection with the bone [6; 7]. This property is determined by such macrostructural parameters as porosity (the proportion of voids in the total volume of the product), dimensions, geometric shape and pore distribution.

In the last decade, the development of new bone structures, and optimization of the geometry of existing porous structures, for bone implants has been the subject of numerous works [8—11]. Two approaches to the creation of such structures can be identified:

— non-parametric design, when the structure is created on the basis of the geometry of a single element;

— parametric design, based in an algorithm with input data in the form of porous structure parameters (porosity, pore size). The structure is generated with some element of randomness, based on mathematical expressions [5].

Of the existing variety of types of porous structures, two were selected for study: a rhombic dodecahedron (*D*, nonparametric design); and Voronoi polyhedra (*V*, parametric design). Materials based on a *D*-type cell are distinguished by the homogeneity of the macrostructure and the high strength properties in all directions [12]. Structure *V* is less homogeneous, but similar in morphology to real bone tissue [13]. It is formed by creating a grid structure based on connecting random discrete points with struts, in accordance with a certain algorithm [14].

Increase in the functional and mechanical properties of materials obtained by the SLM method is associated with the minimization of internal material defects in the form of pores in the struts. Defect porosity is formed due to insufficient or excessive energy density, determining the conditions for powder melting [15]. In order to eliminate defective porosity, it is necessary to correctly select the SLM parameters [4]. When applied to porous structures, where the thickness of internal structural elements ("struts") is 200—300 μm, the problem of defective porosity, as well as geometry accuracy, is of particular importance from the point of view of increasing the strength characteristics of products

[16]. The solution to this problem can achieved by correcting the laser trajectory and reducing the distance between its passes. This in turn requires the other SLM parameters to be changed, in order to ensure optimal energy density.

This study focuses on improving the SLM regime for fabricating porous structures of the *D* and *V* types with thin structural elements and a low level of defect porosity from a Ti—6Al—4V alloy (ASTM F3001) for medical purposes.

Experimental

The initial material employed in this research was Ti—6Al—4V alloy powder (AP&C a GE Additive Company, Canada). According to the ASTM B822 specification, particle size distribution is as follows: $d10$ = = 23 μm, $d50$ = 35 μm, $d90$ = 47 μm. Fluidity according to ASTM B213 and bulk density according to ASTM B213 were 25 s/50 g and 2.55 g/cm^3, respectively. Experimental samples were fabricated using a TRUPRINT1000 laser setup (TRUMPF Gruppe, Germany) equipped with an ytterbium laser with a power of P_L = 175 W, spot diameter of 30 μm, and a maximum laser speed of $v \le 3000$ mm/s. In order to control the SLM regimes, the thickness of the powder layer (t) and the scanning step (h) can be varied. This can be determined by the distance between the laser passes in one layer.

A standard regime (hereinafter *T*) is used, according to the recommendation by the manufacturer, TRUMPF (Germany), for the manufacture of products from this powder. This includes two sets of parameters: for building the main (internal) and contour (external) parts of the product (Table 1).

The main regime is formed by "hatching" with a certain step to build the bulk of the product and must meet the requirements of optimal penetration of the powder layer, in order to ensure low defective porosity (p_d). The tracing regime has one pass along the contour of the object in each layer and serves to ensure the required surface quality of the product. In order to optimize the SLM parameters, it is customary to use the following characteristics: energy density (E) and build rate (BR), calculated by the following equations [17]:

$$E = \frac{P_L}{vht}, \quad (1)$$

$$BR = vht. \quad (2)$$

After fabrication, all samples were subjected to heat treatment in a vacuum furnace according to the standard regime: annealing at 1010 °C (45 min) followed by cooling in the furnace. After heat treatment, the samples were cut from the platform using the EDM method.

In order to assess defect porosity by metallographic analysis, thin sections were prepared by multi-stage grinding and polishing in two stages:

— mechanical grinding on abrasive SiC-paper with particle size from P320 to 4000;

— polishing using a suspension based on silicon oxide with a particle size of 0.05 μm.

Thin polished sections were analyzed using a VERSAMET-2 metallographic microscope (UNITRON, Japan) at 50× magnification. The resulting photographs of the microstructure were processed using ImageJ software (Wayne Rasband (NIH), USA). The ratio of the area of dark segments (pores) to the entire area of the micrograph was used to determine the defect porosity of the segment.

The porosity of the experimental samples (p) was determined by weighing the density of the Ti—6Al—4V compact alloy. This was calculated by the following equation:

$$p = \left(1 - \frac{\rho_{por}}{\rho_{mon}}\right) \cdot 100\ \%, \quad (3)$$

where ρ_{por} is the density of porous sample, and ρ_{mon} = = 4.47 g/cm^3 is the density of Ti—6Al—4V solid alloy.

The density of porous samples was estimated by weighing them and calculating according to the following equation:

$$\rho_{por} = \frac{m_{por}}{V_{ctl}} \cdot 100\ \%, \quad (4)$$

where m_{por} is the weight of sample, g; V_{stl} is the model volume, cm^3.

Table 1. **Parameters of SLM regimes recommended by the manufacturer**

Таблица 1. Параметры режимов СЛП, рекомендованные производителем

Regime	P_L, W	t, mm	h, mm	v, mm/s	E, J/mm^2	BR, cm^3/h
Main	155	0.02	0.11	1200	58.71	9.50
Tracing	75	0.02	–	1000	–	–

X-ray diffraction analysis was carried out using a D8 ADVANCE X-ray diffractometer (Bruker, Germany) at room temperature in CuK_α radiation in the range of 2θ = 30°÷80°. The microstructure of the samples was studied using a VEGA LMH scanning electron microscope (TESCAN, Czech Republic) equipped with an electron backscatter diffraction (EBSD) device.

The Vickers hardness of the samples was determined using a Metkon Metallography hardness tester (Metkon, Turkey), performing at least 5 measurements for each sample at a load of 1 kg and a holding time of 10 s.

The mechanical properties of the samples of porous structures in the form of cylinders with a diameter of 14.0—14.5 mm and a height of 7.0—7.5 mm were evaluated by uniaxial compression tests. The tests were carried out on an Instron 5966 testing machine (Instron — Division of ITW Ltd., USA) at a strain rate of 2 mm/min until a relative strain of 50 % was reached. The values of Young's modulus (E), yield strength ($\sigma_{0,2}$) and ultimate strength (σ_u) were determined according to the deformation curves obtained. For testing purposes, 3 samples were used for each experimental point. The calculated values of mechanical properties were averaged. The measurement error was determined as the standard deviation

Results and discussion

Selection of parameters of porous structures and development of models

As described above, two types of porous structures, *D* and *V*, were selected for study in this work. Their geometric characteristics were selected based on the analysis of the publications, as well as the requirements for porous structures to ensure osseointegration. The technological possibilities of manufacturing [8] were also taken into account.

The selection of the optimal pore size is limited by a very wide range D = 0.1÷1.0 mm [18]. Pore sizes D = 0.1÷0.2 mm are sufficient to accommodate individual osteo-like cells (osteoblasts). D = 0.2÷0.6 mm allow colonization of osteoblasts, while an increase in pore size above 0.6 mm contributes to vascularization, the formation of new blood vessels and bone tissue [8, 10].

The higher the porosity of the material, the greater the internal free volume for the bone tissue. However, according to [19, 20], at porosity values p > 75 %, the strength parameters of porous structures degrade significantly to levels below those of bone tissue.

The thickness of thin internal structural elements ("struts") largely determines the porosity of the final structure, and is limited by the capabilities of SLM. According to [8; 9], the minimum size of such elements to ensure high accuracy is 0.20—0.25 mm. Considering these requirements and using the Materialize 3-matic software (Belgium), models of porous structures and cylindrical samples were created for subsequent fabrication and evaluation of their mechanical properties (see Fig. 1). In order to determine the parameters of the resulting porous structures (porosity (p), pore size (D), and strut thickness (h)) CAD models were analyzed using VGStudio MAX 3.1 software (Germany). The parameters of the developed porous structures are summarized in Table. 2.

The struts of the structure with a *D* type cell have the same thickness. Their location at an angle of 45° relative to the axes ensures the uniformity of mechanical properties in all directions (see Fig. 1). In a structure element of *V* type of a similar size, struts with a variable thickness are observed, although their arrangement looks chaotic. Due to randomization during the generation of such a structure, the pores also have different sizes.

Development of experimental SLM regimes

Table. 1 shows a laser scanning step of 0.11 mm. This is too large for building thin structural elements, since it is comparable to the strut thickness (0.25 μm) (see Fig. 2). Therefore, in order to build the porous structures, the main SLM regimes with a scanning step of 0.04 and 0.05 mm were selected. Fig. 2 shows that a laser movement strategy enables the main regime to be applied more efficiently when building small-sized elements by increasing the number of laser passes inside the struts.

While developing the experimental SLM regimes, the values of the energy density and the building rate of the regime by the manufacturer were taken as a guide-

Table 2. **Parameters of the developed models of porous structures**

Таблица 2. Параметры разработанных моделей пористых структур

Structure type	Strut thickness, mm	Pores size, mm	Porosity, %
D	~0.26	0.4–0.5	~75.3
V	0.20–0.25	0.2–0.8	~75.5

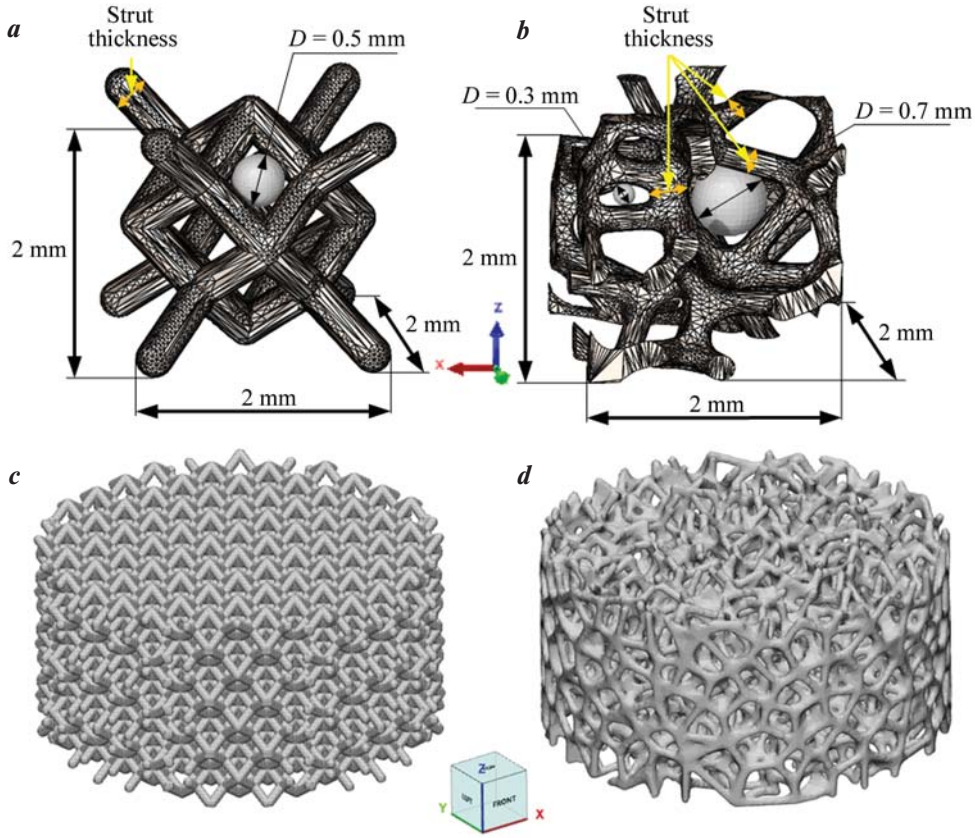

Fig. 1. Elementary cell of *D* type structure (***a***) and cell of *V* type structure of similar size (***b***), models of experimental samples of porous structures *D* (***c***) and *V* (***d***) for mechanical tests

Рис. 1. Элементарная ячейка структуры типа *Д* (***a***) и элемент структуры *В* аналогичного размера (***b***), а также модели экспериментальных образцов пористых структур *Д* (***c***) и *В* (***d***) для механических испытаний

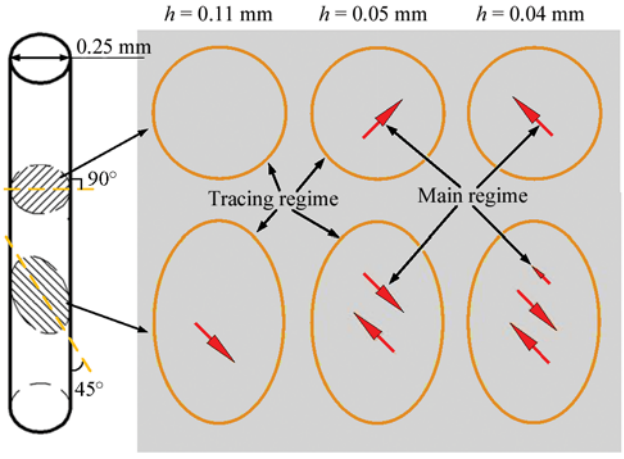

Fig. 2. Schematic view of laser trajectories when plotting a cylinder with a diameter of 0.25 mm in two different sections using SLM regimes with a scanning step of 0.11, 0.05 and 0.04 mm

Рис. 2. Схемы траекторий движения лазера при построении цилиндра диаметром 0,25 мм в двух разных сечениях при использовании режимов с шагом сканирования 0,11, 0,05 и 0,04 мм

line. These conditions enabled products with a low level of defect porosity (less than 0.5 %) to be obtained. Moreover, based on the data of [17], a conditional region was marked on the graph of energy density dependence on building rate. This corresponds to a combination of SLM parameters to obtain products with a minimum number of internal defects (Fig. 3). An additional limitation in the selection of SLM parameters is the limiting speed of building products (vertical lines in Fig. 3), determined by the scanning step (0.04 and 0.05 mm) and the limiting scanning speed. As a result of the selection of SLM parameters, 9 experimental modes were developed (Table 3). These are shown on the map of their dependence on the energy density and building rate (see Fig. 3).

Study of defect porosity and hardness of samples fabricated according to experimental SLM regimes

Using the regimes developed, 9 samples were fabricated in the form of a cube with the size of 3×3×3 mm.

Table 3. **Parameters of the developed experimental SLM regimes and standard regime *T***

Таблица 3. Параметры разработанных экспериментальных режимов СЛП и стандартного режима *T*

SLM regime	P_L, W	*h*, mm	*v*, mm/s	*E*, J/mm^2	*BR*, cm^3/h
1	136	0.04	2900	58.62	8.35
2	143	0.04	2600	68.75	7.49
3	160	0.04	2900	68.97	8.35
4	140	0.05	2860	48.95	10.30
5	155	0.05	2630	58.94	9.47
6	155	0.05	2250	68.89	8.10
7	175	0.05	2630	66.54	9.47
8	135	0.05	2630	51.33	9.47
9	167	0.05	2860	58.39	10.3
T	155	0.11	1200	58.71	9.50

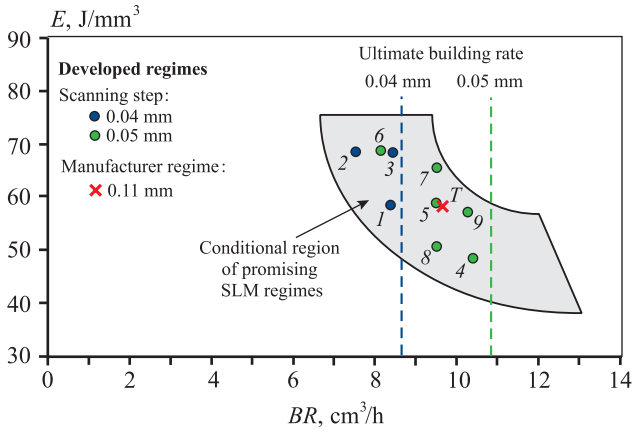

Fig. 3. Distribution map of experimental (***1–9***) and standard (*T*) SLM regimes as a function of energy density and building rate

The conditional area of promising SLM regimes is highlighted in gray

Рис. 3. Карта распределения экспериментальных (т. ***1–9***) и стандартного (*T*) режимов СЛП в зависимости от плотности энергии и скорости построения

Условная область перспективных режимов СЛП выделена серым

Their external view is illustrated in Fig. 4. The e sample obtained according to regime *2* is visually distinguished by the presence of defects on the surface. This regime with the minimum *BR* is the extreme one in the plot of energy density and building rate (see Fig. 3).

Fig 5 shows measurements of defect porosity (p_d) and hardness of the samples obtained using the experimental regimes and under standard conditions (*T*). A high level of p_d values correlates with a large error in measuring the hardness *HV*. This can be explained by the indenter entering in the immediate vicinity of the pores. The material produced according to regimes *1*, *5*, and *7* has the lowest defect porosity and high hardness comparable to the level of these characteristics for the alloy produced according to regime *T*. These regimes correspond to a rather narrow range of parameters (E = 58.6÷66.5 J/mm^2, BR = = 8.4÷9.5 cm^3/h). Taking into account the measurement results, as well as the minimum scanning step (0.04 mm), regime *1* was selected for further research and fabrication of porous structures in comparison with standard conditions *T*.

Study of phase composition and microstructure

Fig. 6 shows the results of the *X*-ray diffraction analysis of the alloy fabricated according to regimes *T* and *1* before and after heat treatment (HT). In all cases, the alloy is in the single-phase state of the low-temperature hexagonal close-packed (HCP) α-phase. No clear *X*-ray lines of the high-temperature BCC β-phase were found in the *X*-ray diffraction patterns.

The microstructure of the alloy after SLM was studied in two regimes with subsequent heat treatment. It was performed using electron backscatter diffraction in a plane parallel to the building plane. Fig. 7 shows

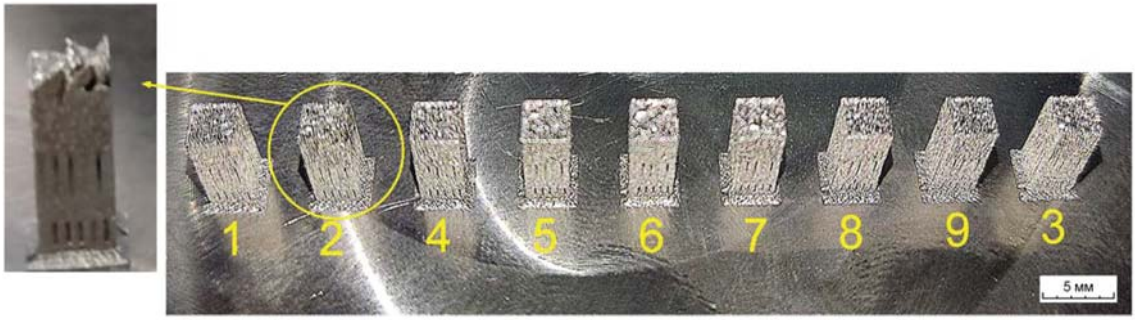

Fig. 4. External view of samples obtained according to the experimental SLM regimes ***1–9*** (see Table 3), with supports on the platform

Рис. 4. Внешний вид образцов, полученных по экспериментальным режимам СПЛ ***1–9*** (см. табл. 3), с поддержками на платформе

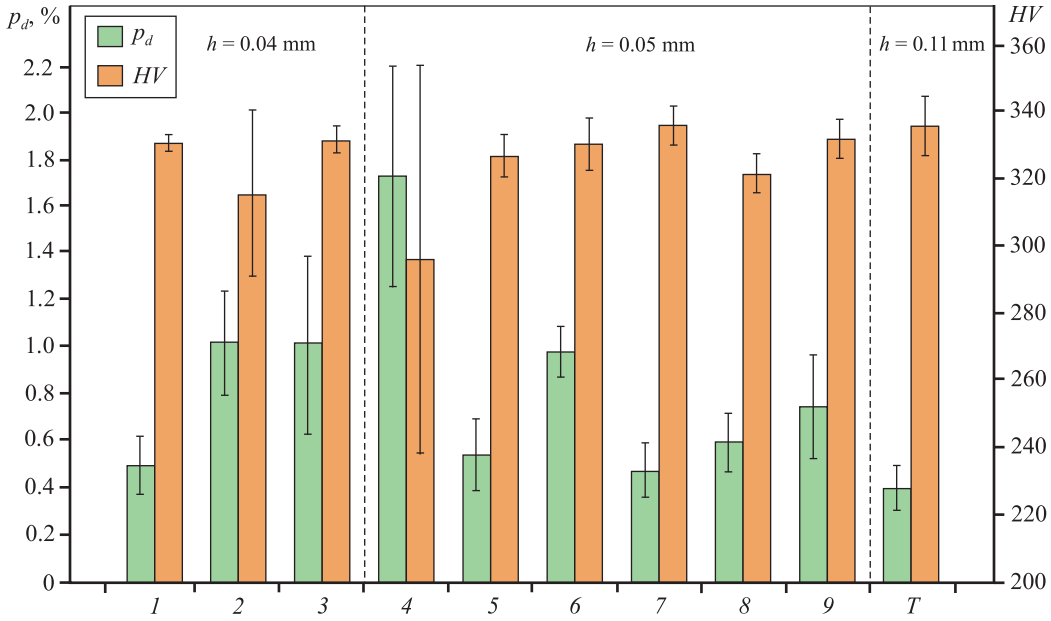

Fig. 5. Defect porosity and hardness of samples obtained by experimental regimes ***1–9***, compared with the standard regime *T*

Рис. 5. Дефектная пористость и твердость образцов, полученных по экспериментальным режимам ***1–9***, в сопоставлении со стандартным режимом *T*

that changing the regime does not lead to a change in the structural state of the material. The microstructure is predominantly represented by α-phase plates 1—5 μm thick formed as a result of β → α-transformation during cooling after annealing. The contours of the packets of α-phase plates are the former (inherited) grain boundaries of the high-temperature β-phase, within which the packets were formed.

The phase state and microstructure of the alloy fully correspond to those obtained using the standard SLM mode after HT in the earlier study of this alloy [20].

Study of the macrostructure and mechanical properties of porous structures

Fig. 8 shows the macrostructure of porous samples obtained according to regime *1*. A considerable quantity of fused granules of powder material is observed on the inner surface. In the lower part of the samples, these particles are much more numerous. This can be explained by the features of the SLM process and is consistent with the observations of other researchers [21]. Granules on the surface create stress concentrators, contribute to

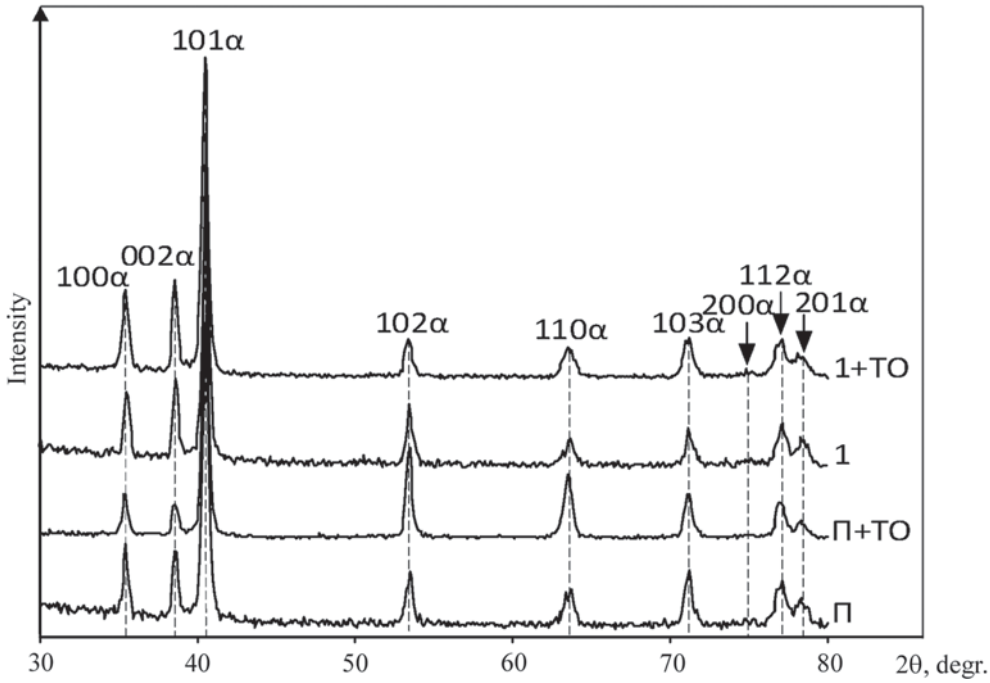

Fig. 6. *X*-ray diffraction patterns of samples obtained by regimes *T* and *1*, before and after heat treatment

Рис. 6. Рентгеновские дифрактограммы образцов, полученных по режимам *T* и *1*, до и после термообработки

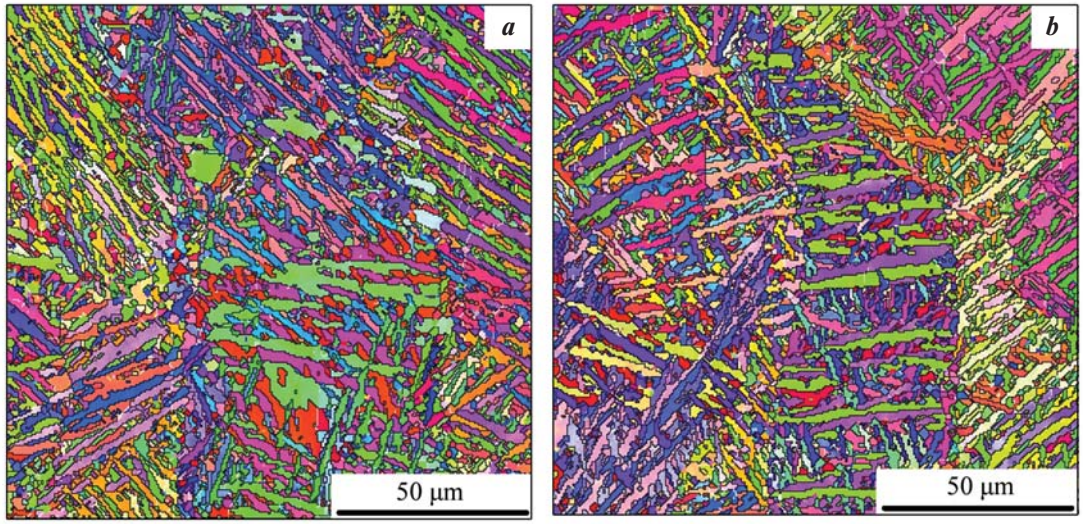

Fig. 7. Microstructure of samples obtained by regimes *T* (***a***) and *1* (***b***), after heat treatment

Рис. 7. Микроструктура образцов, полученных по режимам *T* (***a***) и *1* (***b***), после термообработки

the initiation of fatigue cracks and reduce the fatigue strength of the material, thus they need to be removed [21]. In addition, their presence makes it difficult to quantify the accuracy of the geometry of thin structural elements.

Fig. 9 shows quantitative assessment of defect porosity and geometry was carried out by analyzing images in several sections of the sample obtained using light electron microscopy. Qualitative assessment of the images showed a difference in the level of defect porosity between the samples made according to regimes *T* and *1*.

It was established as a result of the quantitative analysis of defective porosity that for structures obtained

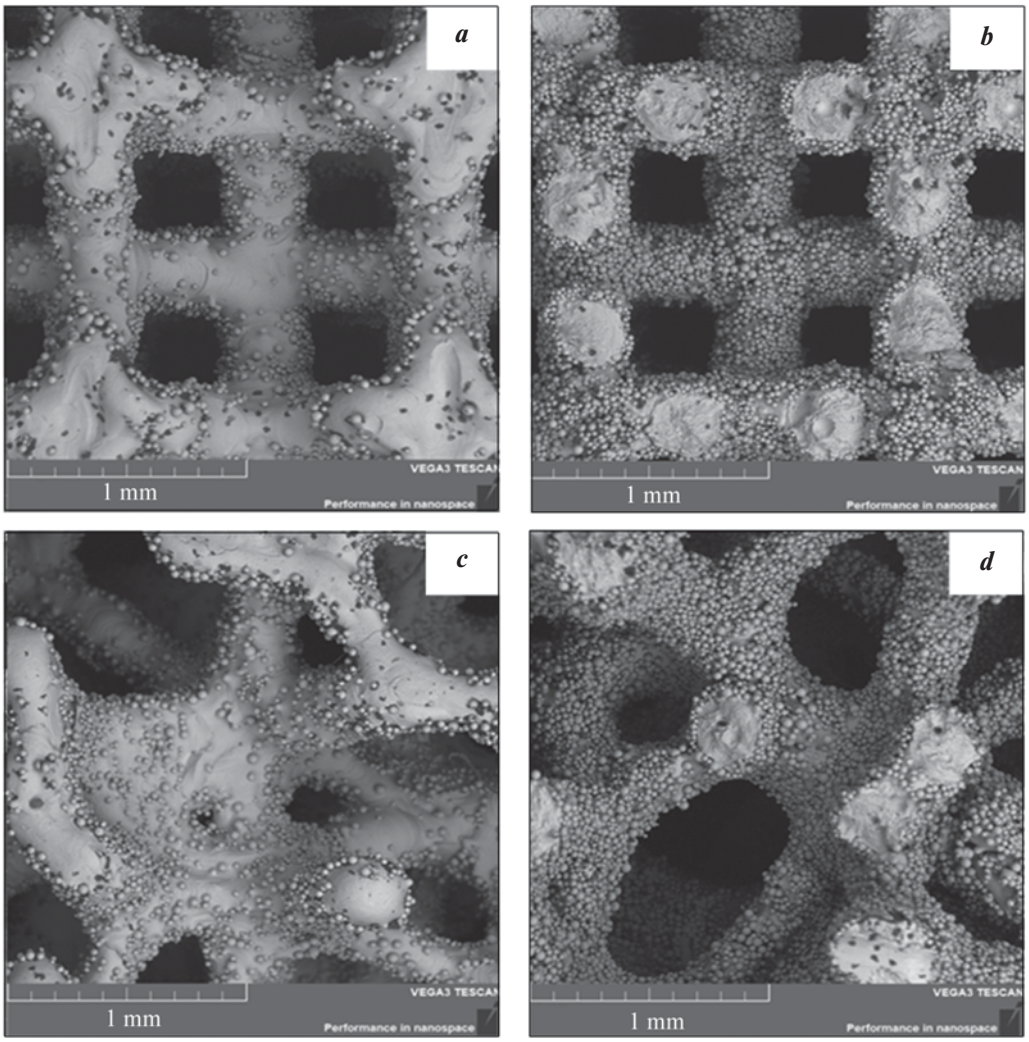

Fig. 8. Macrostructure of samples of porous structures of *D* type (***a***, ***b***) and *V* type (***c***, ***d***), obtained by regime *1*
a, ***c*** – top view, ***b***, ***d*** – bottom view

Рис. 8. Макроструктура образцов пористых структур типа *Д* (***a***, ***b***) и *В* (***c***, ***d***), полученных по режиму *1*
a, ***c*** – вид сверху, ***b***, ***d*** – снизу

according to mode *1*, it is 3 times lower than for samples made according to the manufacturer's mode, and is about 0.6 % (see Fig. 9, *e*).

The thickness of the struts of the *D* type structure, measured from microphotographs, is 265±15 μm and 245±14 μm for modes *1* and *T*. Any differences in the values of defect porosity and the average size of the struts are reflected in the total porosity of the samples: p = 72.3±1.2 % for mode *T* and p = 70.0±1.0 % for regime *1*.

Fig. 10 shows diagrams of deformation by compression of samples of porous structures of *D* and *V* types, fabricated in two regimes. Ultimate strength (σ_u) was determined from the point of the first sharp decrease in stress, corresponding to the primary destruction of one of the rows of struts of the porous structure.

A comparison of the mechanical properties of porous structures shows that the application of the regime developed leads to a significant increase in strength characteristics: increase in the yield strength from 76 to 132 MPa for *D* and from 66 to 86 MPa for *V* (see Fig. 10 and Table 4). A difference in the strength of the two types of structures is associated with a more optimal *D* design [5]. It should be noted that the Young's modulus changes slightly with a sufficiently significant increase in strength and remains in the range of 1—2 GPa. This corresponds to this indicator for spongy bone tissue. When comparing the

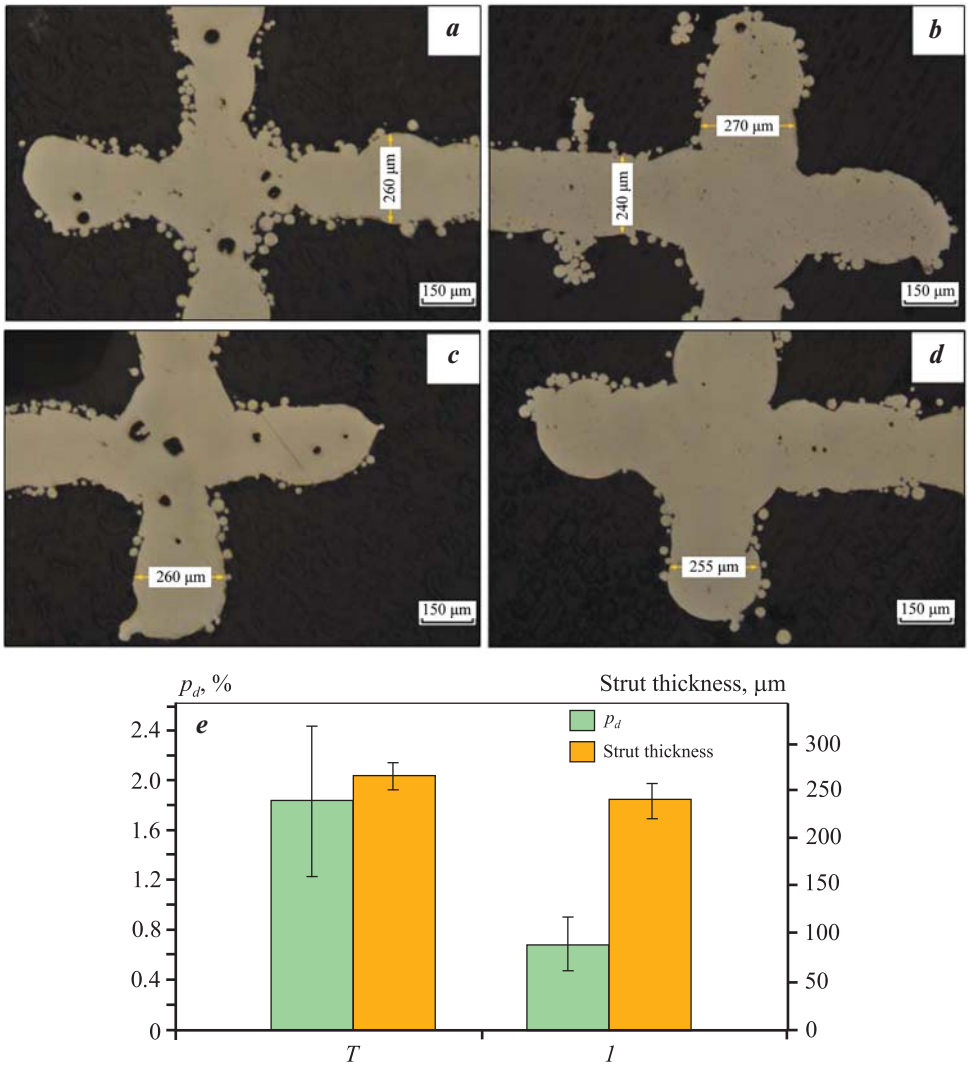

Fig. 9. Typical images of struts in samples of porous structures of *D* type obtained by regimes *T* (***a***, ***c***) and *1* (***b***, ***d***), ***e*** – the average size of the struts of samples of type *D* built according to different modes

Рис. 9. Типичные изображения перемычек в образцах пористых структур типа *Д*, полученных по режимам *T* (***a***, ***c***) и *1* (***b***, ***d***), ***e*** – средний размер перемычки образцов типа *Д* построенных по разным режимам

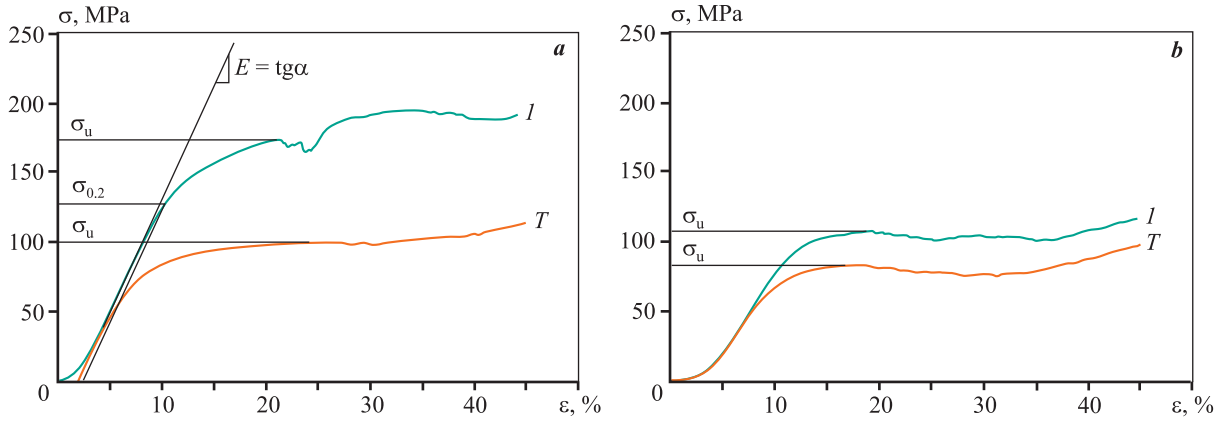

Fig. 10. Compression strain diagrams of samples of porous structures of *D* type (***a***) and *V* type (***b***), obtained by regimes *T* and *1*

Рис. 10. Диаграммы деформации сжатием образцов пористых структур типа *Д* (***a***) и *B* (***b***), полученных по режимам *T* и *1*

Table 4. **Mechanical properties of porous structures obtained by regimes *T* and *1* in comparison with analogues and types of bone tissue**

Таблица 4. Механические свойства пористых структур, полученных по режимам *T* и *1*, в сравнении с аналогами из литературы и типами костной ткани

Structure type (SLM regime)	*p*, %	$\sigma_{0.2}$, MPa	σ_u, MPa	*E*, GPa
D (*P*)	72.3±1.2	76±3	103±6	1.24±0.08
V (*P*)	74.5±1.5	66±4	80±4	1.09±0.14
D (*1*)	70.0±1.0	132±8	173±5	1.55±0.12
V (*1*)	73.4±1.3	86±6	104±5	1.25±0.10
V [19]	68.1±2.7	80±5	93±3	1.82±0.15
D [12]	70*	140±6	174±4	4.89±0.05
Bone tissue [11]:				
cortical bone	–	42–176	–	7–30
trabecular bone	40–80	0.2–10.5	–	0.04–2.0
vertebrae	–	3–6	–	0.37

* Porosity according to CAD model.

mechanical properties of the porous structures of two types build according to the developed SLM regime, the values of Young's modulus are lower than those of analogues with the same porosity and a comparable level of strength, (1.55±0.12 vs. 4.89 ±0.05 for *D* and 1.25±0.10 vs. 1.82±0.15 for *V*).

Conclusions

Based on the results of the study of the influence of selective laser melting parameters on defect porosity, phase composition, microstructure and hardness of Ti—6Al—4V alloy, an approach to the improvement of SLM regimes in the production of highly porous materials with thin internal structural elements was developed. The method was efficiently applied in the manufacturing of porous structures of *D* and *V* type with a porosity of about 75 % developed for bone implants.

A decrease in the level of defect porosity from ≈1.8 to 0.6 %, provided by the use of the developed SLM regime, contributes to a significant increase in the strength characteristics of the material. This is seen in the increase in the yield stress of rhombic dodecahedron from 76 to 132 MPa and that of Voronoi polyhedron from 66 to 86 MPa. At the same time, a low Young's modulus (1—2 GPa) is maintained, corresponding to the level of stiffness of the spongy bone tissue.

References

1. Shunyu Liu, Yung C. Shin, Additive manufacturing of Ti6Al4V alloy: A review. *Materials & Design*. 2019; 164:107552. https://doi.org/10.1016/j.matdes.2018.107552
2. Chlebus E., Kuźnicka B., Kurzynowski T., Dybała B. Microstructure and mechanical behaviour of Ti—6Al—7Nb alloy produced by selective laser melting. *Materials Characterization*. 2011;62(5):488—495. https://doi.org/10.1016/j.matchar.2011.03.006
3. Jalali M., Mohammadi K., Movahhedy M.R., Karimi F., Sadrnezhaad S.K., Chernyshikhin S.V., Shishkovsky I.V. SLM additive manufacturing of NITI porous implants: A review of constitutive models, finite element simulations, manufacturing, heat treatment, mechanical, and biomedical studies. *Metals and Materials International*. 2023. https://doi.org/10.1007/s12540-023-01401-1
4. Brailovski V., Kalinicheva V., Letenneur M., Lukashevich K., Sheremetyev V., Prokoshkin S. Control of density and grain structure of a laser powder bed-fused superelastic Ti—18Zr—14Nb alloy: Simulation-driven process mapping. *Metals*. 2020;10(12):1697. https://doi.org/10.3390/met10121697
5. Chen H., Han Q., Wang C., Liu Y., Chen B., Wang J. Porous scaffold design for additive manufacturing in ortho-

pedics: A review. *Frontiers in Bioengineering and Biotechnology*. 2020;8.
https://doi.org/10.3389/fbioe.2020.00609

6. Nune K.C., Misra R.D., Li S.J., Hao Y.L., Yang R. Cellular response of osteoblasts to low modulus Ti—24Nb—4Zr—8Sn alloy mesh structure. *Journal of Biomedical Materials Research. Pt. A*. 2016;105(3):859—870.
https://doi.org/10.1002/jbm.a.35963
7. Warnke P.H., Douglas T., Wollny P., Sherry E., Steiner M., Galonska S., Becker S.T., Springer I.N., Wilftang J., Sivenanthan S. Rapid prototyping: Porous titanium alloy scaffolds produced by selective laser melting for bone tissue engineering. *Tissue Engineering. Pt. C: Methods*. 2009;15(2):115—124.
https://doi.org/10.1089/ten.tec.2008.0288
8. Barba D., Alabort E., Reed R.C. Synthetic bone: Design by additive manufacturing. *Acta Biomaterialia*. 2019; 97:637—656.
https://doi.org/10.1016/j.actbio.2019.07.049
9. Yan C., Hao L., Hussein A., Young P. Ti—6Al—4V triply periodic minimal surface structures for bone implants fabricated via selective laser melting. *Journal of the Mechanical Behavior of Biomedical Materials*. 2015; 51:61—73.
https://doi.org/10.1016/j.jmbbm.2015.06.024
10. Taniguchi N., Fujibayashi S., Takemoto M., Sasaki K., Otsuki B., Nakamura T., Matsushita T., Kokubo T., Matsuda S. Effect of pore size on bone ingrowth into porous titanium implants fabricated by additive manufacturing: An in vivo experiment. *Materials Science and Engineering: C*. 2016;59:690—701.
https://doi.org/10.1016/j.msec.2015.10.069
11. Timercan A., Sheremetyev V., Brailovski V. Mechanical properties and fluid permeability of gyroid and diamond lattice structures for intervertebral devices: Functional requirements and comparative analysis. *Science and Technology of Advanced Materials*. 2021; 22(1):285—300.
https://doi.org/10.1080/14686996.2021.1907222
12. Li J., Chen D., Zhang Y., Yao Y., Mo Z., Wang L., Fan Y. Diagonal-symmetrical and midline-symmetrical unit cells with same porosity for bone implant: Mechanical properties evaluation. *Journal of Bionic Engineering*. 2019;16(3):468—479.
https://doi.org/10.1007/s42235-019-0038-z
13. Fantini M., Curto M.. Interactive design and manufacturing of a Voronoi-based biomimetic bone scaffold for morphological characterization. *International Journal on Interactive Design and Manufacturing (IJIDeM)*. 2017;12(2):585—596.
https://doi.org/10.1007/s12008-017-0416-x
14. Liu T., Guessasma S., Zhu J., Zhang W. Designing cellular structures for additive manufacturing using Voronoi—Monte Carlo approach. *Polymers*. 2019;11(7):1158.
https://doi.org/10.3390/polym11071158
15. Bhandari L., Gaur V. A study on defect-induced fatigue failures in SLM Ti6Al4V alloy. *Procedia Structural Integrity*. 2022;42:529—536.
https://doi.org/10.1016/j.prostr.2022.12.067
16. Sombatmai A., Uthaisangsuk V., Wongwises S., Promoppatum P. Multiscale investigation of the influence of geometrical imperfections, porosity, and size-dependent features on mechanical behavior of additively manufactured Ti—6Al—4V lattice struts. *Materials & Design*. 2021;209:109985.
https://doi.org/10.1016/j.matdes.2021.109985
17. Letenneur M., Kreitcberg A., Brailovski V. Optimization of laser powder bed fusion processing using a combination of melt pool modeling and design of experiment approaches: Density control. *Journal of Manufacturing and Materials Processing*. 2019;3(1):21.
https://doi.org/10.3390/jmmp3010021
18. Saremian R., Badrossamay M., Foroozmehr E., Kadkhodaei M., Forooghi F. Experimental and numerical investigation on lattice structures fabricated by selective laser melting process under quasi-static and dynamic loadings. *The International Journal of Advanced Manufacturing Technology*. 2021;112(9-10):2815—2836.
https://doi.org/10.1007/s00170-020-06112-0
19. Zhu L., Liang H., Lv F., Xie D., Wang C., Mao Y., Yang Y., Tian Z., Shen L. Design and compressive fatigue properties of irregular porous scaffolds for orthopedics fabricated using selective laser melting. *ACS Biomaterials Science & Engineering*. 2021;7(4):1663—1672.
https://doi.org/10.1021/acsbiomaterials.0c01392
20. Jimenez E.H., Kreitcberg A., Moquin E., Brailovski V. Influence of post-processing conditions on the microstructure, static, and fatigue resistance of laser powder bed fused Ti—6Al—4V components. *Journal of Manufacturing and Materials Processing*. 2022;6:85.
https://doi.org/10.3390/jmmp6040085
21. Van Hooreweder B., Apers Y., Lietaert K., Kruth J.P. Improving the fatigue performance of porous metallic biomaterials produced by selective laser melting. *Acta Biomaterialia*. 2017;47:193—202.
https://doi.org/10.1016/j.actbio.2016.10.005

Information about the authors

Vadim A. Sheremetyev – Cand. Sci. (Eng.), Leading Researcher, Metal Forming Department, National University of Science and Technology "MISIS" (NUST MISIS).
http://orcid.org/0000-0002-2086-0628
E-mail: vadim.sheremetyev@gmail.com

Viacheslav D. Lezin – Postgraduate, Research Laboratory Assistant, Metal Forming Department, NUST MISIS.
http://orcid.org/0000-0002-7568-2005
E-mail: vyacheslavlezin@gmail.com

Marina V. Kozik – Master Student, Research Laboratory Assistant, Metal Forming Department, NUST MISIS.
http://orcid.org/0009-0001-9857-973X
E-mail: marinakozik627@gmail.com

Sergey A. Molchanov – Head of Quality Service, LLC "Conmet".
http://orcid.org/0009-0001-7237-3872
E-mail: molchanov@conmet.ru

Информация об авторах

Вадим Алексеевич Шереметьев – к.т.н., ведущий научный сотрудник кафедры обработки металлов давлением (ОМД), Национальный исследовательский технологический университет «МИСИС» (НИТУ МИСИС).
http://orcid.org/0000-0002-2086-0628
E-mail: vadim.sheremetyev@gmail.com

Вячеслав Дмитриевич Лезин – аспирант, лаборант-исследователь кафедры ОМД, НИТУ МИСИС.
http://orcid.org/0000-0002-7568-2005
E-mail: vyacheslavlezin@gmail.com

Марина Владимировна Козик – студент-магистр, лаборант-исследователь кафедры ОМД, НИТУ МИСИС.
http://orcid.org/0009-0001-9857-973X
E-mail: marinakozik627@gmail.com

Сергей Алексеевич Молчанов – начальник службы качества, ООО «Конмет».
http://orcid.org/0009-0001-7237-3872
E-mail: molchanov@conmet.ru

Contribution of the authors

V.A. Sheremetyev – formulated the research objectives, conducted experiments, wrote and revised the manuscript.

V.D. Lezin – prepared materials and initial samples, prepared the manuscript.

M.V. Kozik – prepared polished samples and obtained micrographs, participated in the discussion of the results.

S.A. Molchanov – participated in the discussion of the results.

Вклад авторов

В.А. Шереметьев – определение цели работы, проведение экспериментов, написание и корректировка текста статьи.

В.Д. Лезин – подготовка материалов и исходных образцов, подготовка текста статьи.

М.В. Козик – подготовка шлифов и получение микроснимков, участие в обсуждении результатов.

С.А. Молчанов – участие в обсуждении результатов.

The article was submitted 24.04.2023, revised 28.04.2023, accepted for publication 03.05.2023

Статья поступила в редакцию 24.04.2023, доработана 28.04.2023, подписана в печать 03.05.2023

UDC 539.219.2: 548.73
https://doi.org/10.17073/0021-3438-2023-4-48-59

Research article
Научная статья

Sputtering by inverted magnetrons: influence on the texture and residual stresses in four layer Ta/W/Ta/W coatings

A.A. Lozovan, S.Ya. Betsofen, A.S. Lenkovets, A.V. Shalin, N.A. Ivanov

Moscow Aviation Institute (National Research University)
4 Volokolamskoe shosse, Moscow 125993, Russia

✉ Alexander A. Lozovan (loz-plasma@yandex.ru)

Abstract: The aim of the study is to examine the possibilities of sputtering of multilayer coatings at a high rate of deposition on products of complex shape using inverted magnetrons. The formation of texture and residual stresses in magnetron four-layer Ta/W/Ta/W coatings deposited at voltages from 0 to –200 V on cylindrical and flat copper substrates imitating elements of the surface of complex shape products was evaluated using the *X*-ray method of inverse pole figures and the $\sin^2\Psi$ method. The patterns of texture formation in coatings depend mainly on the bias voltage on the substrate (U_s), while at $U_s = -200$ V they differ for W and Ta layers. At $U_s = -100$ V, the epitaxial mechanism of texture formation is realized. In the case of a cylindrical substrate, this leads to intense texture (111) of all four layers. In the case of a flat substrate, this can lead to the formation of a single-crystal texture (111) in all layers with a texture maximum width of 12°–14°. The presence of a single-crystal (111) tantalum texture corresponds to the maximum Young moduli and, accordingly, the interatomic bonding forces normal to the coating plane. This suggests that multilayer coatings with an external Ta layer have high tribological characteristics. Increasing the voltage on a flat substrate from 0 to –200 V leads to an increase in residual compressive stresses from 0.5 to 2.7 GPa for the four-layer coating under study.

Keywords: Ta/W/Ta/W coatings, «$\sin^2\Psi$» method, texture, residual stresses, bias voltage.

Acknowledgements: This research was supported by the Russian Science Foundation (grant no. 22-19-00754).

For citation: Lozovan A.A., Betsofen S.Ya., Lenkovets A.S., Shalin A.V., Ivanov N.A. Sputtering by inverted magnetrons: influence on the texture and residual stresses in four layer Ta/W/Ta/W coatings. *Izvestiya. Non-Ferrous Metallurgy*. 2023;29(4):48–59.
https://doi.org/10.17073/0021-3438-2023-4-35-59

Исследование влияния условий напыления системой инвертированных магнетронов на текстуру и остаточные напряжения в четырехслойных Ta/W/Ta/W-покрытиях

А.А. Лозован, С.Я. Бецофен, А.С. Ленковец, А.В. Шалин, Н.А. Иванов

Московский авиационный институт (Национальный исследовательский университет)
125993, Россия, г. Москва, Волоколамское шоссе, 4

✉ Александр Александрович Лозован (loz-plasma@yandex.ru)

Аннотация: Исследованы возможности нанесения с высокой скоростью осаждения многослойных покрытий на изделия сложной формы с помощью инвертированных магнетронов. Рентгеновским методом обратных полюсных фигур и методом «$\sin^2\Psi$» оценивали формирование текстуры и остаточных напряжений в магнетронных четырехслойных Ta/W/Ta/W-покрытиях, нане-

сенных при напряжениях от 0 до –200 В на цилиндрическую и плоскую подложки из меди, имитирующие элементы поверхности изделий сложной формы. Показано, что закономерности формирования текстуры в покрытиях зависят в основном от напряжения смещения на подложке ($U_п$), при этом при $U_п$ = –200 В они отличаются для слоев W и Ta. При $U_п$ = –100 В реализуется эпитаксиальный механизм текстурообразования, который в случае цилиндрической подложки приводит к интенсивной (111) текстуре всех четырех слоев, а в случае плоской – к формированию во всех слоях монокристальной (111) текстуры с шириной текстурного максимума 12°–14°. Наличие монокристальной (111) текстуры тантала соответствует максимальным значениям модуля Юнга и, соответственно, сил межатомной связи нормально плоскости покрытия, что предполагает у многослойных покрытий с внешним Ta-слоем высокие трибологические характеристики. Увеличение напряжения на плоской подложке от 0 до –200 В приводит к повышению остаточных сжимающих напряжений от 0,5 до 2,7 ГПа для исследуемого четырехслойного покрытия.

Ключевые слова: Ta/W/Ta/W-покрытия, метод «$\sin^2\Psi$», текстура, остаточные напряжения, напряжение смещения.

Благодарности: Работа выполнена при финансовой поддержке Российского научного фонда (грант № 22-19-00754).

Для цитирования: Лозован А.А., Бецофен С.Я., Ленковец А.С., Шалин А.В., Иванов Н.А. Исследование влияния условий напыления системой инвертированных магнетронов на текстуру и остаточные напряжения в четырехслойных Ta/W/Ta/W-покрытиях. *Известия вузов. Цветная металлургия*. 2023;29(4):48–59.
https://doi.org/10.17073/0021-3438-2023-4-48-59

Introduction

Refractory coatings, primarily based on tungsten, are promising for various applications such as: microelectronics [1], including spintronics [2; 3]; thermophotovoltaic converters in power engineering; and high-temperature nanophotonics [4]. They can be in demand as thermal barrier coatings for parts of future thermonuclear reactors such as ITER [5; 6], subject to extreme thermal stress and ion bombardment. They can also be used for other heat loaded products such as rocket engine combustion chambers. Key issues for such coatings are thermomechanical stability against delamination, tungsten oxide formation and diffusion at high operating temperatures, as well as the difficulty of achieving long-term high temperature stability in terms of preventing grain growth [4].

Tantalum coatings are of particular interest because they are a promising candidate for the replacement of electrolytic chrome coatings, often used in a variety of tribological and corrosion-resistant applications. Replacement of these coatings is justified, since chromium waste contains 6-valent chromium, a known carcinogen dangerous to the environment. Paper [7] presents the results of a study of the formation of thin magnetron films of α- and β-Ta. It shows that when applied to an amorphous substrate (α-Si, α-SiO_x, α-SiN_x), β-Ta is formed. This belongs to the spatial group of tetragonal syngony P-42_1m (a = 10.194 Å, c = 5.313 Å) with strong axial texture [001]. Heating of Ta coating to 176 °C leads to the formation of α-Ta along with β-Ta, and at a temperature > 326 °C, a single-phase structure of α-Ta is formed. When such coatings are applied to crystalline molybdenum, α-Ta with a texture [110] is formed.

An important role for multilayer coatings is played by the texture of individual layers formed in them, since the efficiency of stress relaxation processes at the interface depends on this. In addition, texture is a defining characteristic for many service properties due to their pronounced orientational dependence. In this regard, special attention should be paid to Ta. Unlike W, it has a pronounced anisotropy of elastic and, with a high probability, also tribological properties. In [8], the phase composition, texture and residual stresses in magnetron Ta coatings of thickness (h) up to 40 μm sputtered at t = 20÷400 °C were investigated. At room temperature β-Ta with (001) texture is formed; at t = = 300 °C — a two-phase mixture of β- and α-Ta with β-Ta dominating with (001) texture (while α-Ta has no pronounced texture); at t = 400 °C — α-Ta with pronounced (110) texture.

The dependence of the α-Ta texture on the film thickness was found. At h > 10 μm, the texture (110) is transferred to (111). The phase composition and texture change as the final coating thickness is formed.

In [9], an *in-situ X*-ray study of tantalum film growth during deposition using a planar magnetron at distances from the target to the glass substrate of 25 and 108 mm was carried out. In the first case, deposition was carried out at a rate of 6.4 nm/min, with an amorphous layer with a thickness of 45 nm closest to the substrate, followed by a β-Ta layer with h = 15 nm, and then an α-Ta layer with h = 190 nm. In the second case, the deposition rate was 1.6 nm/min and the amorphous layer occupied almost 90 % of the total film thickness of 36 nm. β-Ta

had texture (002) and α-Ta was characterized by texture (110), and the degree of texturing increased with the time of film deposition.

The authors [10] investigated the structure of Ta coatings deposited using magnetron sputtering at different bias voltages ranging from 0 to –100 V. This has a marked influence on the phase structure of these coatings. When the bias voltage was increased from 0 to –70 V, their structure changed from a single-phase β-phase at U_s from 0 to –20 V to a two-phase structure in the range of –30 to –40 V and to a full α-phase when the U_s values were in the range of –50 to –100 V. The authors managed to obtain a coating with a thickness of 100 μm with good mechanical properties and relatively low residual stresses (–2.1 GPa) for this thickness.

In [11], the influence of argon pressure (P_{Ar}) from 0.3 to 1.4 Pa on the phase composition, texture, residual stresses, and hardness of magnetron Ta coatings 10—1000 nm thick was investigated. At all P_{Ar}, the coatings consisted of a metastable β-phase, and only at 0.7 Pa was the α-phase Ta detected. For most coatings, compressive stresses from –200 to –1500 MPa were observed, but tensile stresses from 400 to 1100 MPa were found in a number of coatings. The hardness of the coatings varied from 10.2 to 17.7 GPa. At the same time, no correlations were found between hardness and texture or with the magnitude of residual stresses.

The authors of [12] considered the influence of the conditions for deposition of magnetron coatings by the modulated pulse method on the structure and properties of Ta coatings. Their phase composition depends on temperature. The α-Ta phase is formed at a substrate temperature above 365—375 °C, achieved in ~150 min. The β-Ta phase is formed at lower temperatures. For this reason, β-Ta is formed at the initial stage of coating formation, and only at a distance of >14 μm from the substrate the α-Ta phase begins to dominate. Measurements of residual stresses in coatings 5—20 μm thick showed the presence of compressive stresses from –2.0 to –2.2 GPa for coatings with h = 5, 8, 14; and 20 μm and tensile stresses of 1.7 GPa only for coatings with h = 6 μm.

Composite multilayer W/Ta coatings with both a BCC structure and a close surface energy of 3.26 and 2.9 J/m^2, respectively, have been intensively studied in order to establish their possible application in a variety of applied problems [13—15]. Important among them is the development of a method for applying a multilayer uniform thickness W/Ta-coating on the surface of products of complex shape.

Direct current planar magnetron sputtering (DCMS) and high-power pulsed magnetron sputtering (HPPMS) have been successfully used [16] to deposit W/Ta. HPPMS coating is denser and has a smoother surface than DCMS which is a consequence of the deposition of a stream with a higher degree of ionization of the sputtered atoms [17]. However, from the point of view of industrial application, the main disadvantage of HPPMS technology is the significantly lower deposition rate compared to DCMS [16].

Simultaneously resolving both of these problems by using inverted strip magnetrons is also a relevant objective. [17] shows that hollow cathode deposition, in which the substrates are mounted on the axis of an elongated tubular source, can be an efficient method of coating complex-shaped objects. In a hollow cathode magnetron with a uniform current density and a cosine angular distribution of the sputtered material, the sputtered flux (per unit area) at all points inside the cathode (where the final effects are not important) is equal to the cathode erosion flux, regardless of the pressure of the working gas. The authors obtained a copper deposition rate of 400 nm/min. However, it should be borne in mind that when the substrate is large, and the space between it and the cathode becomes a thin ring, the geometry approaches a planar cathode and backscattering of the sputtered atoms reduces the deposition rate.

[18; 19] shows that in order to create thin-walled small-sized axisymmetric shell structures made of layered composites: for example, tubular products with different surface profiles; a system of successively arranged inverted field-cathode magnetrons; and one straight cylindrical magnetron used to clean the substrates is very efficient. Such a system allows the formation of layered composite shells by sputtering various layers onto a mandrel (for example, made of copper) which is subsequently etched.

The aim of achieving uniformity of the coating on the surface of products of complex shape cannot be isolated from the problem of structure, since the microstructure of coatings deposited in vacuum depends on the deposition rate, the directions of arrival of coating atoms, pressure of the working gas, as well as the ion bombardment flux, bias voltage (U_s) on the substrate and its temperature.

This work studies the formation of texture and residual stresses in individual layers of four-layer Ta/W/Ta/W coatings deposited by a system of inverted strip cathode magnetrons on copper substrates of various shapes (flat and cylindrical) at bias voltages on the substrate from 0 to –200 V.

Experimental

The sputtering deposition was carried out using a system of inverted magnetrons installed in series at a distance of 30 mm from each other on a specialized MRM-1 setup as presented in [18]. Argon with a purity of at least 99.9 % was selected as the working gas The cathode material was W and Ta with a purity of ≈99.9 %; the inner diameter and length of the cathodes were 37 and 24 mm, respectively. A tube made of copper M-1 with a diameter of 10 mm and a length of 20 mm was used as a substrate. Before sputtering, the tube was polished and washed in an ultrasonic cleaner in acetone and alcohol. Then the substrate was installed on the rod for vertical movement of samples in the chamber and evacuated to a residual pressure of 10^{-3} Pa. Before sputtering, the glow discharge plasma treatment was applied for 30 min at argon pressure of 5 Pa and a voltage on the substrate of 1100 V. Next, deposition of tantalum and tungsten was carried out at different bias voltages on the substrate according to the regimes presented in Table 1. During sputtering, the substrate performed reciprocating movements along the cathode axis and periodically completely left the cathode area, both ends alternately. Each layer was deposited for 2 h, sputtering all samples for 8 h and obtaining a total coating thickness of 198, 189, 167, 128, and 64 μm at U_s = 0, –50, –100, –150, and –200 V, respectively. The layers alternated in the Ta/W/Ta/W sequence.

The texture was estimated using quantitative inverse pole figures (IPF) by taking diffraction patterns in the angle range 2θ = 30°÷140° in filtered CuK_α radiation. The pole density for 6 normals to (*hkl*) on a stereographic triangle (001, 011, 013, 111, 112, 123) was determined by the equation:

$$P_{(hkl)} = n \frac{I_{(hkl)} / R_{(hkl)}}{\sum_{i=1}^{n} (I_{(hkl)} / R_{(hkl)})}, \quad (1)$$

where $I_{(hkl)}$ and $R_{(hkl)}$ are the integral intensities of reflections (*hkl*) for texturized and textureless (reference) samples, respectively; n = 6 is the number of independent (*hkl*) reflections.

In diffraction strain measurement, the "$\sin^2\Psi$" method is widely applied, in which the interplanar distances for reflection (*hkl*) are measured at several values of the tilt angle Ψ. The residual stress value is determined by the slope (tgα) of the experimental dependence d_Ψ (interplanar distance at the slope angle Ψ) on $\sin^2\Psi$:

$$\sigma_{ост} = \frac{\mathrm{tg}\,\alpha E_{(hkl)}}{d_0(1+\nu_{(hkl)})}, \quad (2)$$

where $E_{(hkl)}$ and $\nu_{(hkl)}$ are the Young's modulus and the Poisson's ratio for the direction of the normal to (*hkl*); d_0 is the interplanar distance at Ψ = 0.

Results and discussion

Investigation of texture in four-layer coating

Figures 1 and 2 show combined diffraction patterns of magnetron coatings Ta, Ta/W, Ta/W/Ta, and Ta/W/Ta/W deposited on a cylindrical Cu substrate at voltages U_s = –100 and –200 V. Analysis of these

Table 1. **Sputtering regimes**

Таблица 1. Режимы напыления

Regime	Layer	U_m, V	I_m, A	$-U_s$, V	I_s, A	P_{Ar}, Pa	t, °C
1	Ta	280–285	1	–	–	0.2	420
	W	290–305	1	–	–	0.2	430
	Ta	275–285	1	–	–	0.2	415
	W	290–305	1	–	–	0.2	430
2	Ta	270–280	1	50 (100, 150, 200)	0.14–0.05	0.2	430
	W	290–300	1	50 (100, 150, 200)	0.14–0.05	0.2	440
	Ta	270–285	1	50 (100, 150, 200)	0.14–0.05	0.2	430
	W	290–305	1	50 (100, 150, 200)	0.14–0.05	0.2	440

diffraction patterns, summarized in Fig. 3 as dependences of the pole densities of reflections (211), (321) and (222) for successive layers in four-layer coatings, indicates that the regularities of texture formation depend mainly on the stress on the substrate. However, they differ for W and Ta layers. This is especially noticeable for coatings deposited at U_s = –200 V (see Fig. 3, *b*).

The use of the calculation of pole densities gives a more adequate and, in addition, a quantitative picture of the features of texture formation in comparison with a qualitative consideration of the reflection intensities in diffractograms. The intensity of the reflection (222) in the textureless reference is 7 and 6 times less than the intensity of the reflections (321) and (211), respectively. In addition, the angular width of the reflection (222) is almost 2 times greater than the reflection (211). Therefore, at the same height of both reflections (211) and the pole density (222) is more than an order of magnitude higher, observed in Fig. 3, *a*.

The influence of the bias voltage on the substrate on texture formation in a four-layer coating can be seen in the fact that at U_s = –100 V (Fig. 3, *a*) an epitaxial relationship between the layer orientations is achieved. The pronounced (111) texture formed in the first Ta layer is reproduced by all subsequent three layers, and even some enhancement of its intensity is observed.

At –200 V (see Fig. 3, *b*), another mechanism of texture formation is observed. This includes the absence of dominance of the (111) orientation, as well as the violation of epitaxy. In the first and third Ta layers, the pole density of the (222) reflection is maximum, but still lower than at a voltage of –100 V. In this case, in the second and fourth W layers, the pole density of the (211) and (321) reflections is higher than reflection (222). The texture in the third tantalum and fourth tungsten layers completely reproduces the texture not of the previous layer, but the texture characteristic of the metal in the first and second layers. This indicates not a partial, but a complete absence of epitaxy. Partial violation of epitaxy would be accompanied by a gradual weakening of the intensity of all texture components with distance from the substrate. However, at U_s = –200 V, a texture is formed in each layer characteristic of this particular metal (see Fig. 3, *b*). This fundamentally distinguishes the texture formation mechanism at this voltage on the substrate from the mechanism typical for U_s = –100 V (see Fig. 3, *a*).

Figure 4 shows diffraction patterns of four-layer Ta/W/Ta/W coatings deposited on a flat substrate at voltages U_s = 0, –50, –100, and –200 V. In the absence of voltage on the substrate (Fig. 4, *a*) and at its value — 50 V (Fig. 4, *b*) the (111) texture dominates, and at U_s = –100 V (Fig. 4, *c*) it is enhanced to such an extent that we can speak of its single-crystal character. At a voltage of –200 V, as on a cylindrical substrate, the (111) texture component is weakened. Of particular interest in this regard is the single-crystal texture shown in Fig. 4, *c*, which corresponds to the texture of the fourth W-layer.

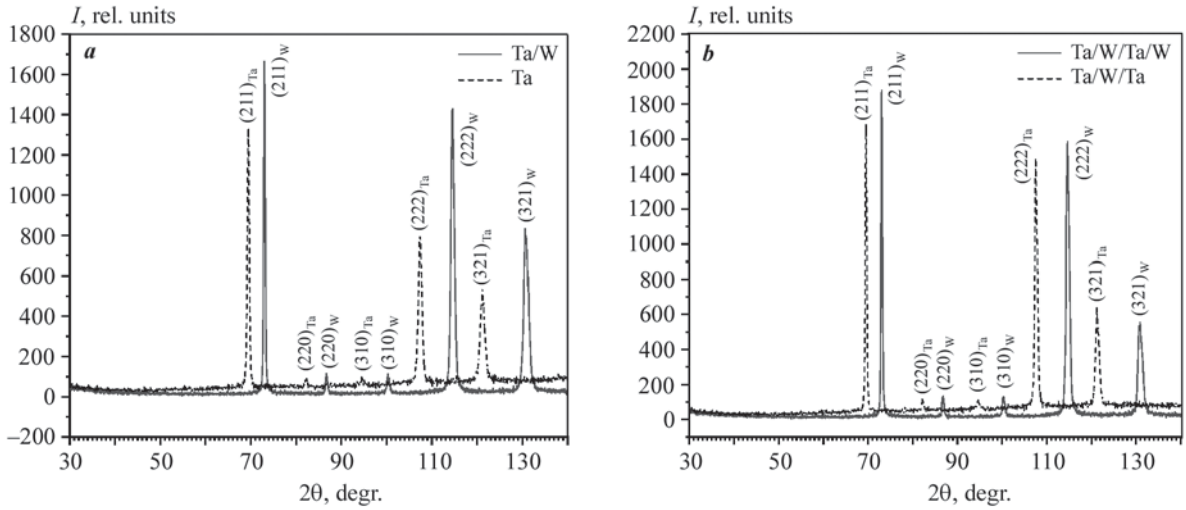

Fig. 1. Combined *X*-ray diffraction patterns of Ta, Ta/W (***a***) and Ta/W/Ta, Ta/W/Ta/W (***b***) magnetron coatings deposited on a cylindrical Cu substrate at U_s = –100 V

Рис. 1. Совмещенные дифрактограммы магнетронных покрытий Ta, Ta/W (***a***) и Ta/W/Ta, Ta/W/Ta/W (***b***) нанесенных на цилиндрическую Cu-подложку при напряжении $U_п$ = –100 В

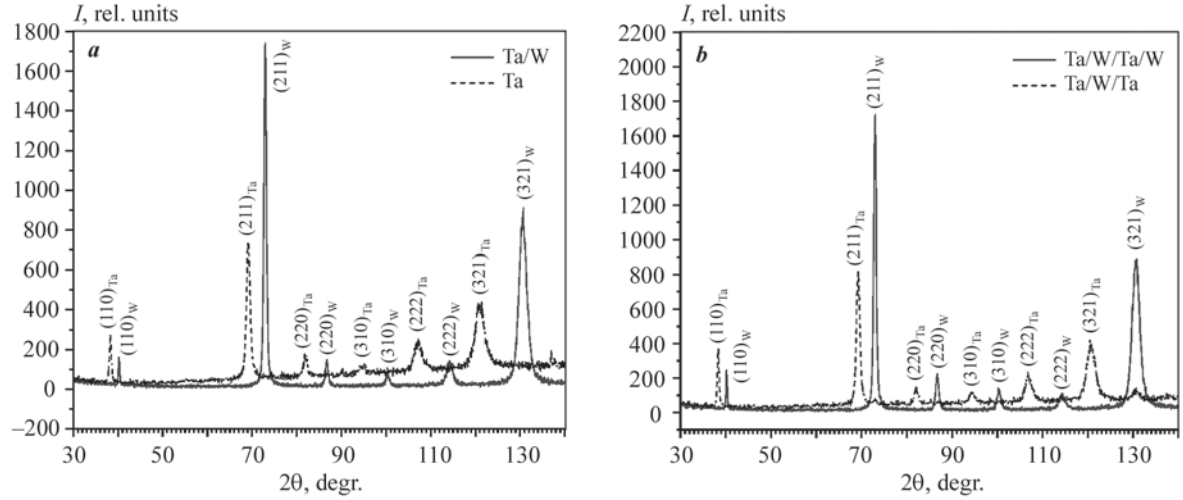

Fig. 2. Combined X-ray diffraction patterns of Ta, Ta/W (***a***) and Ta/W/Ta, Ta/W/Ta/W (***b***) magnetron coatings deposited on a cylindrical Cu substrate at $U_s = -200$ V

Рис. 2. Совмещенные дифрактограммы магнетронных покрытий Ta, Ta/W (***a***) и Ta/W/Ta, Ta/W/Ta/W (***b***), нанесенных на цилиндрическую Cu-подложку при напряжении $U_п = -200$ В

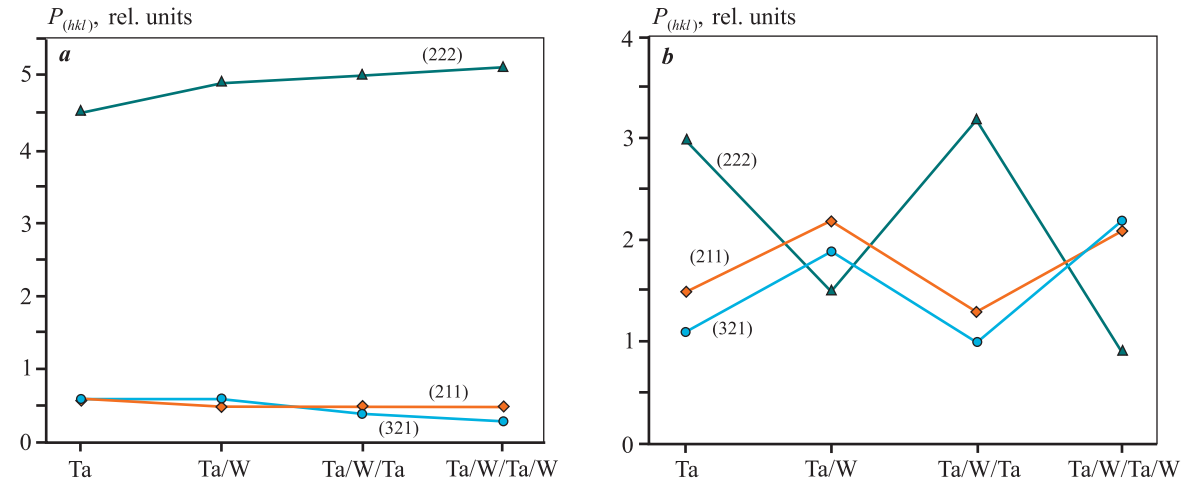

Fig. 3. Pole reflection densities (*hkl*) for layers of four-layer coatings deposited on a cylindrical Cu substrate at voltages $U_s = -100$ V (***a***) and –200 V (***b***)

Рис. 3. Полюсные плотности рефлексов (*hkl*) для слоев четырехслойных покрытий, нанесенных на цилиндрическую Cu-подложку при напряжениях $U_п = -100$ В (***a***) и –200 В (***b***)

Figure 5, *a* shows reflection (222) for the outer W layer at tilt angles Ψ = 0°, 5°, and 10°. When the deviation from the normal to the sample exceeds 10°, there are no grains with such a misorientation. The half-width of the texture maximum for the (222) reflection is ~12°, corresponding to the misorientation angles of single-crystal nickel superalloys [20]. The diffraction pattern from the first Ta layer deposited at $U_s = -100$ V practically does not differ from that for the fourth W layer, which indicates that, as in the case of coatings on a cylindrical substrate (see Fig. 3, *a*), at the mentioned voltage, an epitaxial correspondence of the orientations of successive layers is realized on it.

Figure 5, *b* shows reflections (222) for a single-layer Ta coating at angles Ψ = 0°, 10°, and 15°, which demonstrate that there are no grains with such angle of misorientation when deviated from the normal to the sample by an angle of 15°. The half-width of the texture maximum for the (222) reflection for Ta layer is ~14°, which, as in the case of a cylindrical substrate (see Fig. 3, *a*),

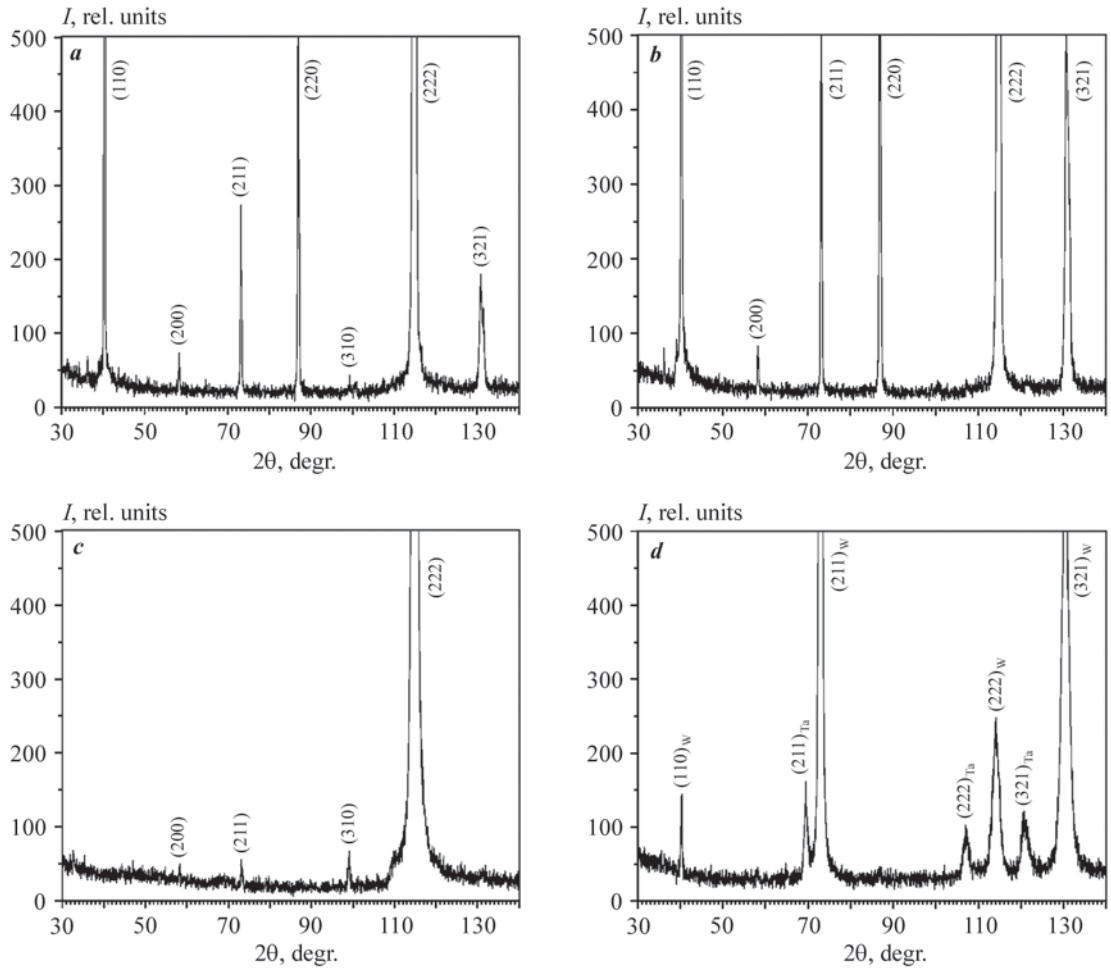

Fig. 4. *X*-ray diffraction patterns of outer W-layers of four-layer magnetron Ta/W/Ta/W coatings deposited at different substrate voltages

U_s = 0 (***a***), –50 V (***b***), –100 V (***c***) and –200 V (***d***)

Рис. 4. Дифрактограммы внешних W-слоев четырехслойных магнетронных покрытий Ta/W/Ta/W, нанесенных при различных напряжениях на подложке

$U_п$ = 0 (***a***), –50 В (***b***), –100 В (***c***) и –200 В (***d***)

indicates an increase in the degree of texturization of the fourth layer compared to the first.

The importance of the result obtained is due to the fact that Ta has a "positive" elastic anisotropy, for which the maximum Young modulus (E_{max}) is located along the <111> direction of the Ta BCC lattice (Table 2). Therefore, the orientation of the coating plane parallel to the (111) crystallographic plane corresponds to the location of the direction with E_{max} and, accordingly, with the maximum value of the interatomic bond forces normal to the coating plane.

Thus, with a high degree of probability, high wear resistance should be expected in multilayer coatings with an external Ta layer. Tungsten is the only metal that does not have elastic anisotropy (Table 3), but it is possible that the "single-crystal" orientation of W-layers will be useful for realizing other physicochemical properties, in relation to which this metal will have the necessary anisotropy.

Measuring residual stresses in four-layer coating

Our attempts to estimate the residual stresses for coatings deposited on cylindrical substrates failed. In essence this was the reason for applying coatings on a flat substrate. Problems also arose in estimating the residual stresses on the coatings, in which, at U_s = –100 V, a "single-crystal" texture was formed (see Fig. 5) for the outer layer of a four-layer Ta/W/Ta/W and a single-layer Ta coating.

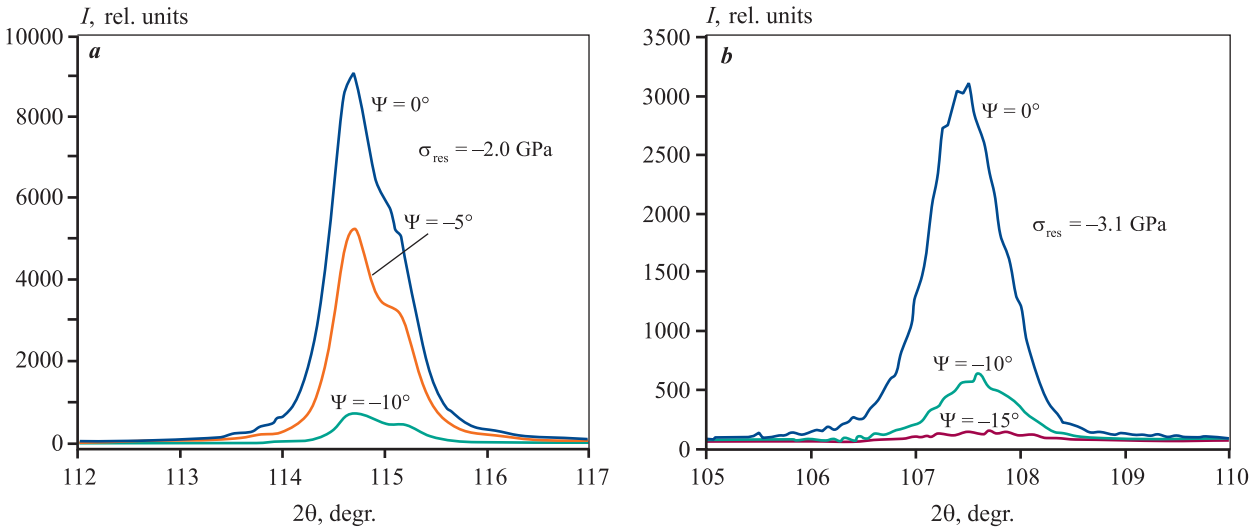

Fig. 5. Reflection (222) for pseudo-single-crystal magnetron coatings deposited at $U_s = -100$ V at various tilt angles Ψ
a – the outer W layer of the four-layer Ta/W/Ta/W coating; ***b*** – single-layer Ta-coating

Рис. 5. Рефлекс (222) для псевдомонокристальных магнетронных покрытий, нанесенных при $U_п = -100$ В, при различных углах наклона Ψ
a – внешний W-слой четырехслойного Ta/W/Ta/W-покрытия; ***b*** – однослойное Ta-покрытие

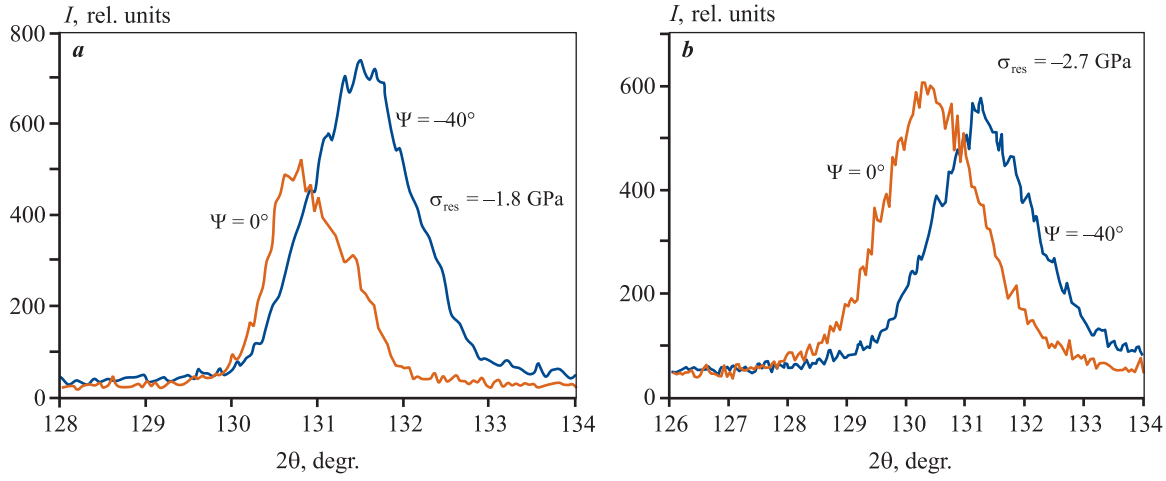

Fig. 6. Reflection (321) of the outer W-layer for four-layer Ta/W/Ta/W magnetron coatings deposited at $U_s = -50$ V (***a***) and –200 V (***b***) at tilt angles Ψ = 0° and –40°

Рис. 6. Рефлекс (321) внешнего W-слоя для четырехслойных Ta/W/Ta/W магнетронных покрытий, нанесенных при $U_п = -50$ В (***a***) и –200 В (***b***) при углах наклона Ψ = 0° и –40°

The "$\sin^2\Psi$" method provides for recording at tilt angles in the range from 0° to 40°—60°. For single-crystal coatings, as can be seen from Fig. 5, the value of Ψ cannot exceed 10°, severely limiting the sensitivity of the method. Only the presence of ultrahigh stress values in both coatings made it possible to estimate the residual stresses for them. They amounted to –2.0 GPa for the outer W layer in a four-layer coating and –3.1 GPa for a single-layer Ta coating.

Such a difference between the residual stresses can be attributed to two reasons. First, it is possible that the high stress value of a single-layer Ta-coating decreases in subsequent layers due to the mutual compensation of the thermal component of stresses when alternat-

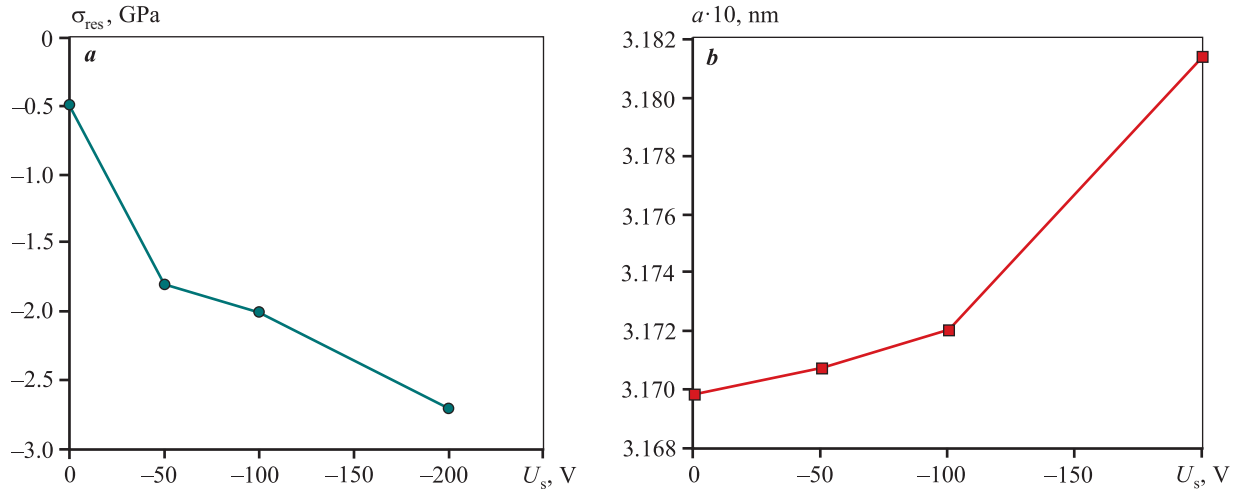

Fig. 7. Residual stresses (***a***) and lattice periods (***b***) of four-layer magnetron Ta/W/Ta/W coatings as a function of voltage on the substrate

Рис. 7. Зависимости остаточных напряжений (***a***) и периодов решетки (***b***) четырехслойных магнетронных покрытий Ta/W/Ta/W от напряжения на подложке

Table 2. **Young's moduli for Ta and W <*uvw*> directions**

Таблица 2. Значения модуля Юнга для <uvw> направлений Ta и W

<*uvw*>	*E*, GPa	
	Ta	W
<110>	193.4	409.8
<100>	145.8	409.8
<211>	193.4	409.8
<310>	160.0	409.8
<111>	217.1	409.8
<321>	193.4	409.8

ing layers of refractory metals [21] differ in coefficient of thermal expansion (CTE) ($\alpha_W = 4.3 \cdot 10^{-6}$ K– and $\alpha_{Ta} = 6.5 \cdot 10^{-6}$ K^{-1}). This leads to a decrease in stresses in the W-coating, which is the fourth layer. The second reason for such a difference in voltages may be related to the fact that the first Ta layer is deposited on a copper substrate, the CTE value of which ($\alpha_{Cu} = 16.6 \cdot 10^{-6}$ K^{-1}) differs from Ta by almost 5 times the difference of the W-layer from the preceding Ta layer.

For other coatings, the use of the "$\sin^2\Psi$" method is not a problem. Figure 6 shows reflections (321) of the outer W-layer of four-layer coatings deposited at voltages of –50 and –200 V. It can be seen that with a tilt of –40°, the intensity can be even higher than with symmetrical shooting ($\Psi = 0°$). In general, the value of residual compressive stresses for four-layer coatings increases with increasing stress on the substrate (Fig. 7, *a*), due to which the value of the grating period also increases (Fig. 7, *b*).

Conclusions

1. The regularities of texture formation in a four-layer Ta/W/Ta/W coating obtained using a sputtering system of inverted magnetrons depend mainly on the voltage on the substrate, but differ for W and Ta layers. The latter is especially evident for coatings deposited at $U_s = –200$ V.

2. At a substrate voltage of –100 V, a special mechanism of texture formation operates, manifesting itself in the realization of an epitaxial relation between the layer orientations. In this case, for a cylindrical substrate, the strong texture (111) of the first Ta layer is reproduced by all subsequent three layers, while for a flat substrate, a single-crystal texture (111) is formed with a texture maximum width of 12°—14°.

3. The presence of a single-crystal texture (111) of the Ta layer corresponds to the maximum Young modulus and, accordingly, the interatomic bond forces normal to the coating plane, suggesting that multilayer coatings with an external Ta layer have high tribological characteristics.

4. An increase in the voltage on a flat substrate from 0 to –200 V leads to an increase in residual compressive stresses from 0.5 to 2.7 GPa for a four-layer Ta/W/Ta/W coating.

5. In the first Ta-layer of the single-crystal coating, the residual stresses were –3.1 GPa, while in the fourth W-layer they were –2.0 GPa. This can be attributed to stress relaxation in the intermediate layers, as well as the fact that the difference in TCLE values between the first Ta layer and the Cu substrate is 5 times greater than the difference between the fourth W layer and the previous Ta layer.

References

1. Dooho Choi, Bincheng Wang, Suk Chung, Xuan Liu, Amith Darbal, Adam Wise, Noel T. Nuhfer, Katayun Barmak. Phase, grain structure, stress, and resistivity of sputter-deposited tungsten films. *Journal of Vacuum Science & Technology: A*. 2011;29(5):051512. http://dx.doi.org/10.1116/1.3622619
2. Pai Chi-Feng, Liu Luqiao, Li Y., Tseng H.W., Ralph D.C., Buhrman R.A. Spin transfer torque devices utilizing the giant spin hall effect of tungsten. *Applied Physics Letters*. 2012;101:122404. http://dx.doi.org/10.1063/1.4753947
3. Vüllers F.T.N., Spolenak R. Alpha-vs. Beta-W nanocrystalline thin films: A comprehensive study of sputter parameters and resulting materials' properties. *Thin Solid Films*. 2015;577:26—34. https://doi.org/10.1016/j.tsf.2015.01.030
4. Stelmakh V., Rinnerbauer V., Joannopoulos J.D., Soljačić M., Celanovic I., Senkevich J.J. Evolution of sputtered tungsten coatings at high temperature. *Journal of Vacuum Science & Technology: A*. 2013;31(6):061505. http://dx.doi.org/10.1116/1.4817813
5. Chargui A., Beainou R.El., Mosset A., Euphrasie S., Potin V., Vairac P., Martin N. Influence of thickness and sputtering pressure on electrical resistivity and elastic wave propagation in oriented columnar tungsten thin films. *Nanomaterials*. 2020;10(1):81. https://doi.org/10.3390/nano10010081
6. Dutta N.J., Buzarbaruah N., Mohanty S.R. Damage studies on tungsten due to helium ion irradiation. *Journal of Nuclear Materials*. 2014;452(1-3):51—56. http://dx.doi.org/10.1016/j.jnucmat.2014.04.032
7. Liudas Pranevicius. Magnetron-sputter deposition of W coatings for fusion applications. *Materials Science (Medžiagotyra)*. 2009;15(3):212—219.
8. Esteve J., Zambrano G., Rincon C., Martinez E., Galindo H., Prieto P. Mechanical and tribological properties of tungsten carbide sputtered coatings. *Thin Solid Films*. 2000;373(1—2):282—286. https://doi.org/10.1016/S0040-6090(00)01108-1
9. Nygren R.E., Raffray R., Whyte D., Urickson M.A., Baldwin M., Snead L.L. Making tungsten work—ICFRM-14 session T26 paper 501. *Journal of Nuclear Materials*. 2011;417(1-3):451—456. https://doi.org/10.1016/j.jnucmat.2010.12.289
10. Smid I., Akiba M., Vieider G., Plöchl L.. Development of tungsten armor and bonding to copper for plasma-interactive components. *Journal of Nuclear Materials*. 1998;258-263(1):160—172. https://doi.org/10.1016/S0022-3115(98)00358-4
11. Dias M., Mateus R., Catarino N., Franco N., Nunes D., Correia J. B., Carvalho P. A., Hanada K., Sarbu C., Alves E. Synergistic helium and deuterium blistering in tungsten—tantalum composites. *Journal of Nuclear Materials*. 2013;442(1-3):69—74. https://doi.org/10.1016/j.jnucmat.2013.08.010
12. Colin J.J., Abadias G., Michel A., Jaouen C. On the origin of the metastable b-Ta phase stabilization in tantalum sputtered thin films. *Acta Materialia*. 2017; 126:481—493. https://doi.org/10.1016/j.actamat.2016.12.030
13. Gladczuk L., Patel A., Paur C.S., Sosnowski M. Tantalum films for protective coatings of steel. *Thin Solid Films*. 2004;467(1-2):150—157. https://doi.org/10.1016/j.tsf.2004.04.041
14. Lee S.L., Windover D., Lub T.-M., Audino M. In situ phase evolution study in magnetron sputtered tantalum thin films. *Thin Solid Films*. 2002;420-421:287—294. https://doi.org/10.1016/S0040-6090(02)00941-0
15. Lin J., Moore J.J., Sproul W.D., Lee S.L., Wang J. Effect of negative substrate bias on the structure and properties of Ta coatings deposited using modulated pulse power magnetron sputtering. *IEEE Transactions on Plasma Science*. 2010;38(11):3071—3078. https://doi.org/10.1109/TPS.2010.2068316
16. Navid A.A., Hodge A.M. Nanostructured alpha and beta tantalum formation—Relationship between plasma parameters and microstructure. *Materials Science and Engineering: A*. 2012;536:49—56. https://doi.org/10.1016/j.msea.2011.12.017
17. Myers S., Lin J., Souza R.M., Sproul W.D., Moore J.J. The β to α phase transition of tantalum coatings deposited by modulated pulsed power magnetron sputtering. *Surface & Coatings Technology*. 2014;214:38—45. https://doi.org/10.1016/j.surfcoat.2012.10.061
18. Fritze S., Hans M., Riekehr L. Osinger B., Lewin E., Schneider J.M., Jansson U. Influence of carbon on microstructure and mechanical properties of magnetron sputtered TaW coatings. *Materials and Design*. 2020;196:109070. https://doi.org/10.1016/j.matdes.2020.109070
19. Konuru S.L.K., Umasankar V., Sarma A. Deposition of tungsten—tantalum composite coating on RAFM steel

by sputtering deposition process. *Fusion Engineering and Design*. 2020;160:111972.
https://doi.org/10.1016/j.fusengdes.2020.111972

20. Konuru S.L.K., Umasankar V., Sarma A. Development and characterisation of W and W—25%Ta composite coatings on steel material. *Journal of Surface Science and Technology*. 2020;36(3-4):103—108.
https://doi.org/10.18311/jsst/2020/20109
21. Emmerlich J., Mráz S., Snyders R., Jiang K., Schneider J.M. The physical reason for the apparently low deposition rate during high-power pulsed magnetron sputtering. *Vacuum*. 2008;82(8):867—870.
https://doi.org/10.1016/j.vacuum.2007.10.011
22. Thornton J.A., Hedgcoth V.L. Tubular hollow cathode sputtering onto substrates of complex shape. *Journal of Vacuum Science & Technology*. 1975;12: 93—97.
https://doi.org/10.1116/1.568631
23. Lozovan A.A., Lenkovets A.S., Ivanov N.A., Alexandrova S.S., Kubatina E.P. System of inverted magnetrons for the formation of multilayer composites on axisymmetric small-sized substrates. *Journal of Physics: Conference Series*. 2018;1121:012020.
https://doi.org/10.1088/1742-6596/1121/1/012020
24. Lozovan A.A, Betsofen S.Ya., Lenkovets A.S., Grushin I.A., Labutin A.A., Pavlov Yu.S. Research of the effect of bias voltage on the morphology, structure and lattice spacings of the Nb coatings deposited by inverted magnetron. *Journal of Physics: Conference Series*. 2018;1121:012019.
https://doi.org/10.1088/1742-6596/1121/1/012019
25. Shalin R.E., Svetlov I.L., Kachanov E.B., Toloraia V.N., Gavrilov O.S.. Single crystals of nickel heat-resistant alloys. Moscow: Mashinostroyeniye, 1997. 336 p. (In Russ.).
Шалин Р.Е., Светлов И.Л., Качанов Е.Б., Толораия В.Н., Гаврилин О.С. Монокристаллы никелевых жаропрочных сплавов. М.: Машиностроение, 1997. 336 с.
26. Betsofen S.Ya., Lozovan A.A., Lenkovets A.S., Labutin A.A., Grushin I.A. Texture and residual stresses in Mo, Nb, and Nb/Mo magnetron coatings. *Russian Metallurgy (Metally)*. 2021;(7):883—891.
https://doi.org/10.1134/S0036029521070028
Бецофен С.Я., Лозован А.А., Ленковец А.С., Лабутин А.А., Грушин И.А. Исследование формирования текстуры и остаточных напряжений в магнетронных Mo-, Nb- и Nb/Mo-покрытиях. *Металлы*. 2021;4:87—98.

Information about the authors

Alexander A. Lozovan – Dr. Sci. (Eng.), Professor of the Department 1101, Moscow Aviation Institute (National Research University) (MAI (NRU)).
http://orcid.org/0000-0001-9478-6793
E-mail: loz-plasma@yandex.ru

Sergey Ya. Betsofen – Dr. Sci. (Eng.), Professor of the Department 1101, MAI (NRU).
http://orcid.org/0000-0003-0931-2839
E-mail: s.betsofen@gmail.com

Aleksandr S. Lenkovets – Cand. Sci. (Eng.), Senior Lecturer of the Department 1101, MAI (NRU).
http://orcid.org/0009-0006-6271-2179
E-mail: kompozitplasma@gmail.com

Alexey V. Shalin – Cand. Sci. (Eng.), Assistant Professor of the Department 1102, MAI (NRU).
http://orcid.org/0009-0009-0660-7026
E-mail: shalinaleks@yandex.ru

Nikolai A. Ivanov – Junior Research Scientist of the Department 1101, MAI (NRU).
http://orcid.org/0009-0002-3513-8571
E-mail: el8i7presley@gmail.com

Информация об авторах

Александр Александрович Лозован – д.т.н., профессор кафедры 1101, Московский авиационный институт (Национальный исследовательский университет) (МАИ (НИУ)).
http://orcid.org/0000-0001-9478-6793
E-mail: loz-plasma@yandex.ru

Сергей Яковлевич Бецофен – д.т.н., профессор кафедры 1101, МАИ (НИУ).
http://orcid.org/0000-0003-0931-2839
E-mail: s.betsofen@gmail.com

Александр Сергеевич Ленковец – к.т.н., ст. преподаватель кафедры 1101, МАИ (НИУ).
http://orcid.org/0009-0006-6271-2179
E-mail: kompozitplasma@gmail.com

Алексей Владимирович Шалин – к.т.н., доцент кафедры 1102, МАИ (НИУ).
http://orcid.org/0009-0009-0660-7026
E-mail: shalinaleks@yandex.ru

Николай Андреевич Иванов – мл. науч. сотрудник кафедры 1101, МАИ (НИУ).
http://orcid.org/0009-0002-3513-8571
E-mail: el8i7presley@gmail.com

Contribution of the authors

A.A. Lozovan – formulated the objectives of the study, conducted experiments, wrote the manuscript.

S.Ya. Betsofen – participated in the discussion of the results, wrote the manuscript.

A.S. Lenkovets – conducted experiments.

A.V. Shalin – conducted *X*-ray phase analysis.

N.A. Ivanov – prepared initial samples, conducted experiments, participated in the discussion of the results.

Вклад авторов

А.А. Лозован – определение цели работы, участие в обсуждении результатов, написание текста статьи.

С.Я. Бецофен – участие в обсуждении результатов, написание текста статьи.

А.С. Ленковец – проведение экспериментов.

А.В. Шалин – проведение рентгенофазового анализа.

Н.А. Иванов – подготовка исходных образцов, проведение экспериментов, участие в обсуждении результатов.

The article was submitted 22.05.2023, revised 25.05.2023, accepted for publication 29.05.2023

Статья поступила в редакцию 22.05.2023, доработана 25.05.2023, подписана в печать 29.05.2023

UDC 669.295
https://doi.org/10.17073/0021-3438-2023-4-60-69

Research article
Научная статья

Effect of structure and phase composition on the physical and mechanical properties of hot extruded titanium alloy Ti–3Al–2.5V tubes

A.G. Illarionov[1,2], F.V. Vodolazskiy[1], S.M. Illarionova[1], Ya.I. Kosmatskiy[3], N.A. Shirinkina[4], M.A. Shabanov[1]

[1] **Ural Federal University named after the First President of Russia B.N. Yeltsin**
19 Mira Str., Yekaterinburg 142432, Russia

[2] **Institute of Metal Physics named after M.N. Mikheev of the Ural Branch of the Russian Academy of Sciences**
18 S. Kovalevskaya Str., Yekaterinburg 620108, Russia

[3] **JSC "The Russian Research Institute of the Tube & Pipe Industries"**
30 Novorossiyskaya Str., Chelyabinsk 454139, Russia

[4] **JSC "Ural Works of Civil Aviation"**
2g Bakhchivandzhi Str., Yekaterinburg 620025, Russia

✉ Yaroslav I. Kosmatsky (Kosmatski@rosniti.ru)

Abstract: This study investigates the impact the hot extrusion process variables on the physical and mechanical properties of Ti–3Al–2.5V alloy tubes. The research examines four tube segments extracted from various hot-extruded tubes of Ti–3Al–2.5V alloy, with an outer diameter (OD) of 90 mm and a wall thickness of 20 mm. The manufacturing process involves expanding sleeves with a horizontal hydraulic press to achieve an OD of 195 mm, followed by heating to 850–865 °C prior to extrusion. The tube segments are labeled as *1*, *2*, *3*, and *4*, corresponding to their order of production. Our findings demonstrate that an increase in the number of extrusions in the $\alpha + \beta$ area from tube 1 to tube 4 leads to a reduction in the primary α-phase volume fraction and an increase in the β-transformed structure volume fraction. These changes are attributed to the higher final extrusion temperature resulting from more intense deformation heating during hot tooling (die and mandrel) processes. Additionally, elevating the final extrusion temperature from tube *1* to tube *4* leads to a notable decrease in the residual β-solid solution volume fraction and a reduction in the "sharpness" of the α-phase tangent-oriented texture. The alterations in the structural and phase state of the alloy from tube *1* to tube *4* are found to influence the contact modulus of elasticity and microhardness. These identified relationships can be utilized to optimize the process variables for the extrusion of multiple Ti–3Al–2.5V alloy tubes.

Keywords: titanium alloy Ti–3Al–2.5V, hot extrusion, structure, texture, mechanical properties.

Acknowledgements: This study is supported by the Russian Science Foundation, grant No. 18-79-10107-P.

For citation: Illarionov A.G., Vodolazskiy F.V., Illarionova S.M., Kosmatskiy Ya.I., Shirinkina N.A., Shabanov M.A. Effect of structure and phase composition on the physical and mechanical properties of hot extruded titanium alloy Ti–3Al–2.5V tubes. *Izvestiya. Non-Ferrous Metallurgy*. 2023;29(4):60–69. https://doi.org/10.17073/0021-3438-2023-4-60-69

Влияние структурно-фазового состояния на физико-механические свойства горячепрессованных труб из титанового сплава Ti–3Al–2,5V

А.Г. Илларионов[1,2], **Ф.В. Водолазский**[1], **С.М. Илларионова**[1], **Я.И. Космацкий**[3], **Н.А. Ширинкина**[4], **М.А. Шабанов**[1]

[1] **Уральский федеральный университет имени первого Президента России Б.Н.Ельцина**
620002, Россия, г. Екатеринбург, ул. Мира, 19

[2] **Институт физики металлов имени М.Н. Михеева УрО РАН**
620108, Россия, г. Екатеринбург, ул. С. Ковалевской, 18

[3] **АО «Русский научно-исследовательский трубный институт»**
454139, Россия, г.Челябинск, ул. Новороссийская 30

[4] **АО «Уральский завод гражданской авиации»**
620025, Россия, г. Екатеринбург, ул. Бахчиванджи, 2г

✉ Ярослав Игоревич Космацкий (Kosmatski@rosniti.ru)

Аннотация: Исследовано влияние изменения параметров горячего прессования на физико-механические свойства труб из сплава Ti–3Al–2,5V. Материалом для исследования служили четыре патрубка, отобранные от разных горячепрессованных труб из сплава Ti–3Al–2,5V с внешним диаметром 90 мм и толщиной стенки 20 мм, полученных из экспандированных гильз с внешним диаметром 195 мм на горизонтальном гидравлическом прессе. Экспандированные гильзы перед прессованием нагревались до температуры 850–865 °С. Образцам исследуемых горячепрессованных труб присвоены номера *1*, *2*, *3* и *4* согласно последовательности их получения в промышленных условиях. Показано, что увеличение количества проведенных прессовок в α + β-области от трубы *1* к трубе *4* приводит к закономерному уменьшению объемной доли первичной α-фазы в их структуре, а также к росту объемной доли β-превращенной структуры вследствие повышения температуры окончания прессования, вызванного более активным деформационным разогревом из-за увеличения температуры инструмента (матрицы и иглы). Обнаружено, что фиксируемое структурно повышение температуры окончания прессования от 1-й трубы к 4-й влечет за собой характерное уменьшение объемной доли остаточного β-твердого раствора и снижение «остроты» наблюдаемой тангенциальной текстуры α-фазы. Установлено, что выявленные изменения структурно-фазового состояния сплава от 1-й трубы к 4-й оказывают закономерное влияние на получаемый в них уровень свойств – контактного модуля упругости и микротвердости. Полученные закономерности необходимо учитывать при разработке технологического режима многоразового прессования труб из сплава Ti–3Al–2,5V.

Ключевые слова: титановый сплав Ti–3Al–2,5V, горячее прессование, структура, текстура, механические свойства.

Благодарности: Исследования проведены в рамках выполнения проекта Российского научного фонда (№ 18-79-10107-П).

Для цитирования: Илларионов А.Г., Водолазский Ф.В., Илларионова С.М., Космацкий Я.И., Ширинкина Н.А., Шабанов М.А. Влияние структурно-фазового состояния на физико-механические свойства горячепрессованных труб из титанового сплава Ti–3Al–2,5V. *Известия вузов. Цветная металлургия*. 2023;29(4):60–69. https://doi.org/10.17073/0021-3438-2023-4-60-69

Introduction

Pseudo-α-titanium alloys exhibit a distinctive combination of advantageous properties, such as high specific strength, corrosion resistance, and excellent manufacturability. They find application in the production of critical components, including tubes [1—4]. One such alloy is the Ti—3Al—2.5V pseudo-α-titanium alloy which conforms to the ASTM B338 Standard Specification for Seamless and Welded Titanium and Titanium Alloy Tubes for Condensers and Heat Exchangers. This alloy is widely employed in the manufacturing of tubes [5; 6], and its manufacturability allows for the production both hot-extruded [7] and cold-drawn tubes [8; 9].

Nikol'skii L. et al. [10], Kosmatskiy Ya. et al. [11] have observed that the hot extrusion process used to fab-

ricate tubes and other products from the Ti—3Al—2.5V alloy can exhibit temperature and deformation variations. These variations arise due to deformation heating of the workpiece and tooling, as well as potential cooling of the product surfaces when they come into contact with a colder tool.

Kosmatskiy Ya. et al. [12], Tarin P. et al. [13], and Illarionov A. et al. [14] conducted research on the Grade 9 alloy and found that temperature fluctuations during hot drawing in the α + β two-phase region influence the ratio of α- and β-phases, thermophysical properties, and deformation forces. Additionally, Pyshmintsev I. et al. [7] reported that such temperature variations impact the final structure, phase composition, and texture after cooling. Consequently, these variations are likely to affect the physical and mechanical properties of the end product.

Despite the existing research on the topic, there is a notable absence of studies investigating the effects of the structure and phase composition formed under non-stationary hot extrusion conditions on the properties of Ti—3Al—2.5V alloy tubes. Therefore, the purpose of this study is to address this research gap and explore the specific impact of non-stationary hot extrusion conditions on the properties of the Ti—3Al—2.5V alloy tubes.

Materials and methods

The samples consisted of four tube segments extracted from various hot-extruded Ti—3Al—2.5V alloy tubes, with an outer diameter (OD) of 90 and a wall thickness of 20 mm. These tubes were manufactured by utilizing 195 mm outer diameter expanded sleeves and a horizontal hydraulic press. Prior to the extrusion process, the expanded sleeves were heated to 850—865 °C. The specific extrusion process variables, including temperature and strain rate, were detailed in a previous work by the authors [15]. The four samples of the hot-extruded tubes were numbered *1*, *2*, *3*, and *4* according to the sequence of their manufacturing.

In this study, three main analytical techniques were employed to characterize the samples. Optical microscopy, *X*-ray diffraction (XRD), and micro-indentation were utilized to measure the Vickers hardness and contact modulus of elasticity of the tubes. The microstructure of the tubes was analyzed using a GX51 microscope (Olympus, Japan). For sample preparation, micro slides were etched using an aqueous solution consisting of a mixture of hydrofluoric and nitric acids (1 part HF + + 3 parts HNO_3 + 5 parts H_2O) as suggested by Anoshkin N. et al. in [16], following the method suggested by Anoshkin N. et al. in [16]. XRD analysis was performed on a Bruker D8 Advance *X*-ray diffraction platform (Bruker, Germany) using copper CuK_α radiation in the $2\theta = 34°\div102°$ range. The XRD data were analyzed using Rietveld refinement [17] with the TOPAS® 4.2 software package.

Microgeometry and contact modulus of elasticity measurements were carried out using the Oliver-Farr micro indentation hardness test [18]. A MHTX micro indenter (CSM Instruments, Switzerland) was utilized, applying a 9 N load with 6 measurements conducted per sample.

Results and discussion

In order to assess the phase state of the tubes, *X*-ray diffraction (XRD) analysis was conducted on the longitudinal sections of the samples (Fig. 1).

The Rietveld refinement of the XRD patterns (Fig. 2) yielded the identification of two distinct phases, namely, α-phase and β-phase lines. The lattice parameters of both the α + β- and β-phases were estimated from the XRD patterns, and the corresponding volume fraction of the β-phase was determined. The results are summarized in the table below.

The olume fraction of the β-phase in all the samples varied between 4.8 to 6.2 %. There is a noticeable correlation between changes in the volume fraction of the β-phase and the lattice period; the period slightly increases with the volume fraction. This outcome is in line with expectations, as the presence of β-stabilizers (vanadium and iron impurities) in the β-solid solution

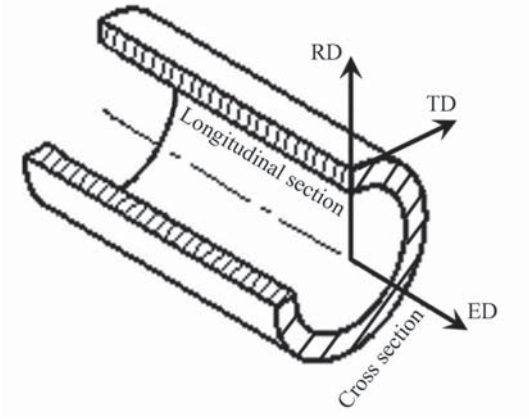

Fig. 1. The three directions are denoted as follows
RD – radial direction, TD – tangential direction,
ED – extrusion direction

Рис. 1. Эскиз трубы с указанием трех основных направлений, связанных с внешним воздействием
РН – радиальное направление, ТН – тангенциальное направление, НП – направление прессования

Lattice periods of the α- and β-phases, the volume fraction of the β-phase in hot-extruded tube samples *1–4*

Периоды решеток α- и β-фаз, объемная доля β-фазы в образцах *1–4* горячепрессованных труб

Sample No.	α-phase			β-phase	
	Lattice parameter, nm		*c/a*	Lattice period, nm	Volume fraction, %
	a	*c*			
1	0.29370	0.46724	1.5909	0.32242	6.2
2	0.29408	0.46770	1.5904	0.32222	5.4
3	0.29388	0.46757	1.5911	0.32202	5.0
4	0.29391	0.46761	1.5910	0.32196	4.8

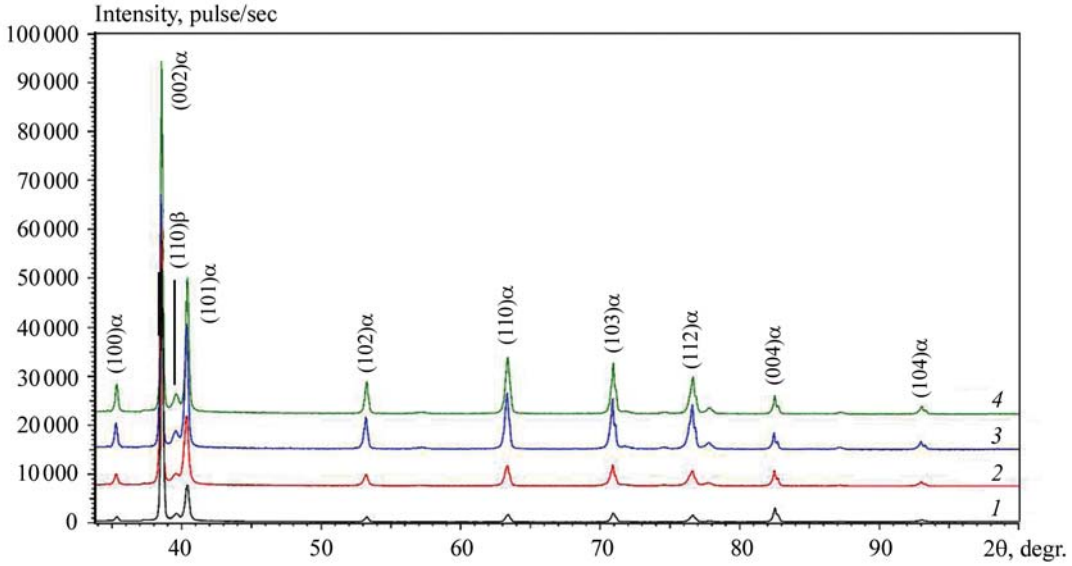

Fig. 2. XRD patterns of the hot-extruded tubes ***1–4***

Shooting in the tangential direction

Рис. 2. Дифрактограммы образцов ***1–4*** горячепрессованных труб

Съемка в тангенциальном направлении

decreases. Prior research [19—21] has established that these stabilizers contribute to the reduction of the lattice period.

Regarding the tube samples (labeled as 1-4), the c/a parameter of the α-phase falls within the range of 1.5904 to 1.5911 (refer to the table). This value is lower than the c/a values for the original sleeves, which range from 1.5913 to 1.5915, and these sleeves were expanded at a temperature similar to that of the hot extrusion process. This discrepancy suggests that the diffusion processes in the α-phase, which occur during cooling down from the extrusion temperature, are less complete compared to those in the the phase formed during cooling after expansion. The reason behind this observation is that the wall of the hot-extruded tubes is 72 % thinner than that of the expanded sleeves, leading to higher cooling rates and consequently reducing the diffusion period.

Fedulov V. et al. [22] conducted a study on the VT23 titanium alloy, which shares a similar temperature of polymorphic $\alpha + \beta \rightarrow \beta$ transformation with the Ti—3Al—2.5V alloy [1]. In their research, it was demonstrated that when the wall thickness is reduced by 65—75 % during cooling from 850 °C (close to the tube extrusion temperature), the cooling rate along the cross-section more than doubles.

An analysis of the *X*-ray diffraction (XRD) patterns of the tubes allowed for a comparison of the intensities of the α-phase lines. It was observed that the (002)α line exhibits the highest intensity in the hot-extruded tube samples *1—4*. Interestingly, for the sleeves after expansion, the (101)α line, not the (002)α

line, displayed the highest intensity. This discrepancy indicates that the hot extrusion process creates a tangent-oriented basic texture of the α-phase (Fig. 3) in the two-phase region of the tube samples *1—4*. In other words, the normal to the basis plane (0001) in the α-phase grains is predominantly oriented in the tangential direction. This finding aligns with the work of Forney C. et al. [23], who reported that reduction drawing, as in our case, facilitates the formation of a tangent-oriented basic texture. It should be noted that the quality of the texture varies from tube to tube, as evidenced by the changes in the relative intensities of the primary α-phase lines in the XRD patterns relative to the (002)α line (Fig. 4).

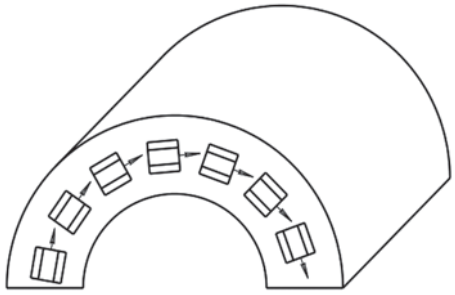

Fig. 3. Characteristic arrangement of the α-phase hexagonal cell as the tangent-oriented texture is formed in the Ti–3Al–2.5V alloy

Рис. 3. Характерное расположение гексагональной призмы α-фазы при формировании тангенциальной текстуры в сплаве Ti–3Al–2,5V

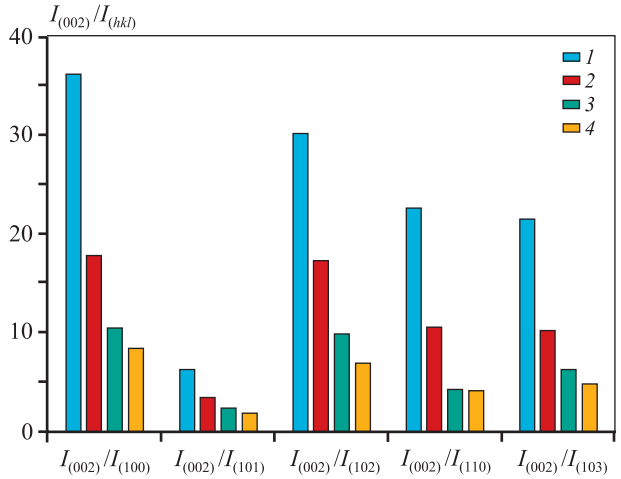

Fig. 4. $I_{(002)}/I_{(hkl)}$ ratio variations at the max intensity of the α-phase lines with different (*hkl*) indices ***1—4***

Рис. 4. Изменение отношения $I_{(002)}/I_{(hkl)}$ для максимальной интенсивности линий α-фазы с различными индексами (*hkl*) на дифрактограммах для горячепрессованных труб ***1—4***

As evident from Fig. 4 and the table, there exists a correlation between the quality of the tangent-oriented texture and the volume fraction of the β-phase: the higher the fraction, the more intense the line becomes (reflected by the higher $I_{(002)}/I_{(hkl)}$) ratio). This observation leads to the conclusion that the XRD pattern analysis for the β-phase volume fraction indicates the resistance to decomposition during cooling of the high-temperature β-solid solution. Moreover, this resistance is linked to the relationship between the condition of the α-phase texture and the physical and mechanical properties (as depicted in Fig. 5). Specifically, as the volume fraction of the β-phase decreases, both the contact modulus of elasticity and microhardness exhibit a corresponding decrease.

The observed relationship between the values can be explained as follows. Samples *1* and *2* retain a larger amount of β-phase, indicating less complete decomposition of the high-temperature β-solid solution and α-phase separation during cooling, in comparison to samples *3* and *4*. The less complete decomposition of the high-temperature β-phase usually occurs when the initial β-solid solution contains more β-stabilizers

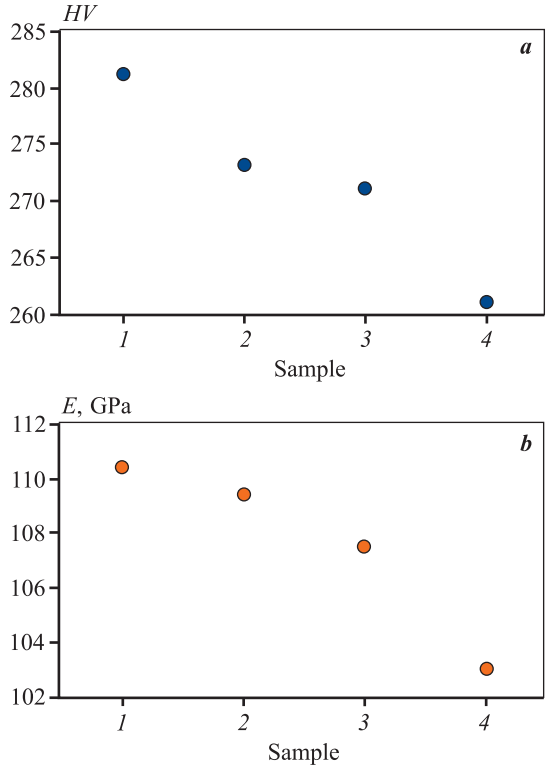

Fig. 5. Variations of the average microhardness (***a***) and contact modulus of elasticity (***b***) in samples ***1—4***

Рис. 5. Изменение средних значений микротвердости (***a***) и контактного модуля упругости (***b***) в образцах ***1—4*** горячепрессованных труб

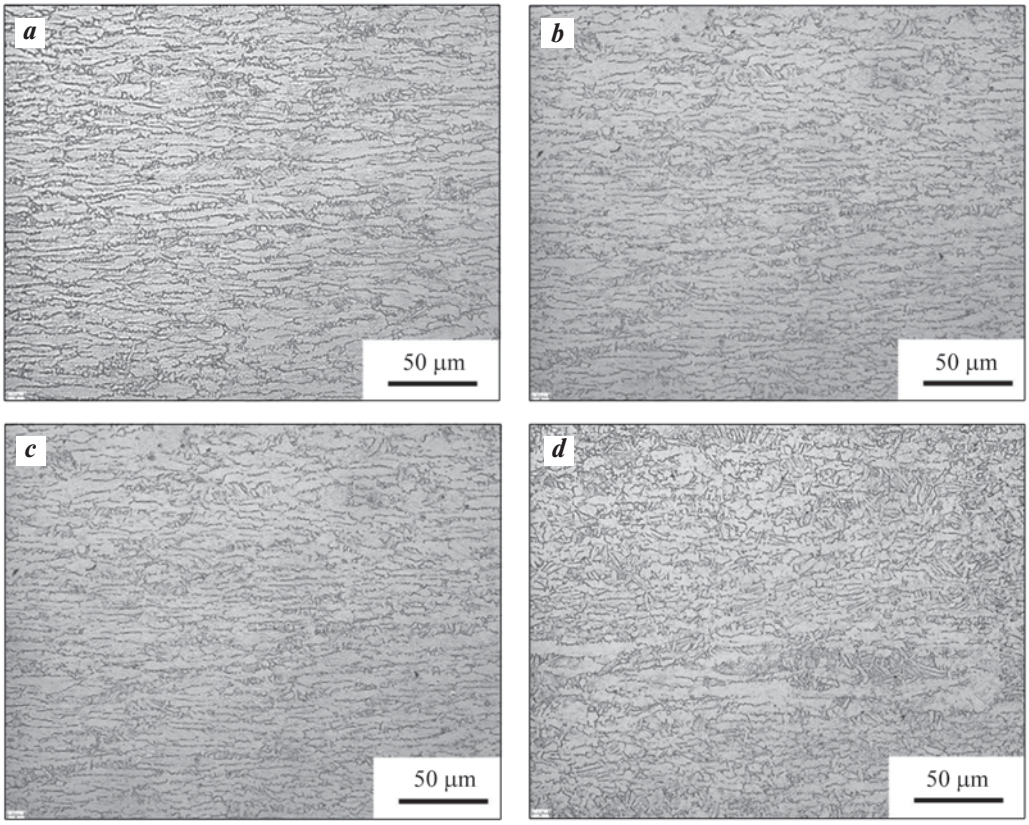

Fig. 6. Predominant longitudinal section microstructure of the ***1*** (***a***), ***2*** (***b***), ***3*** (***c***) and ***4*** (***d***) hot-extruded tube samples, Ti–3Al–2.5V alloy

Рис. 6. Преобладающая микроструктура в продольном сечении горячепрессованных труб ***1*** (***a***), ***2*** (***b***), ***3*** (***c***) и ***4*** (***d***) из сплава Ti–3Al–2,5V

before cooling. The presence of more β-stabilizers in the initial state is a result of a lower initial cooling temperature of the tube compared to the other tubes. This effect arises from the lesser deformation heating of the first Ti—3Al—2.5V alloy tubes manufactured by hot extrusion. Subsequent extrusions cause additional heating of the tools (die and mandrel), leading to reduced heat removal from the tube to the tool. Similar effects have been observed in other metal extrusion processes [24; 25].

The proposed explanation is further supported by the microstructural analysis of the tubes. A thorough examination of typical structures found in most areas of the longitudinal tube section revealed that samples *1* and *2* (Fig. 6, *a*, *b*) are dominated by primary α-phase grains elongated along the direction of extrusion. Small regions of the β-transformed structure exist between the grains, appearing as clusters of secondary α-phase thin plates with different orientations and β-phase interlayers. The formation of the β-transformed structure occurs as a consequence of the high-temperature β-solid solution decomposition during cooling from the extrusion temperature.

A notable characteristic of the structure in samples *3* and *4* (Fig. 6, *c*, *d*) compared to samples *1* and *2* is a significant decrease in the volume fraction of the primary α-phase elongated along the direction of extrusion. This reduction results in an increase in the volume fraction of the β-transformed structure areas. The primary α-phase exhibits partial fragmentation and spheroidization, indicating dynamic recovery processes [26]. Furthermore, the β-transformed structure areas become broader, and the secondary α-plates are enlarged.

The observed difference in the structure of the tube samples can be logically explained by the gradual increase in the end-extrusion temperature from sample *1* to sample *4*. This temperature rise occurs due to higher deformation heating caused by the increasing temperature of the die and mandrel during the extrusion process of tubes *1* to *4*. Consequently, this intensifies relaxation recovery and dissolution of the

primary α-phase, leading to an increase in the volume fraction and size of the high-temperature β-phase areas during the extrusion process. Upon cooling, the β-phase decomposes in these areas, forming plates of the secondary α-phase.

The observed decrease in microhardness from sample *1* to sample *4* (see Fig. 5) can be attributed to the more intense recovery processes in the primary α-phase, which are associated with the removal of deformation hardening, and the enlargement of decomposition products in the β-transformed matrix. This conclusion is further supported by comparing the β-phase volume fraction with the thermodynamic analysis conducted in the ThermoCalc software [14].

The increase in extrusion temperature in the two-phase α + β region leads to a higher amount of β-solid solution and a depletion of β-stabilizers (vanadium and iron). This, in turn, reduces the resistance of the β-phase to decomposition during subsequent cooling. As a result, in samples *3* and *4*, which were heated to higher temperature during extrusion compared to samples *1* and *2*, the decomposition of the β-solid solution starts at higher temperatures and leads to the formation of larger secondary α-phase plates. Additionally, the decomposition process is more complete, resulting in a smaller volume fraction of the residual β-solid solution (as indicated in the table).

Unlike the primary phase, the secondary α-phase plates were not deformed during extrusion. Therefore, they lack a clear orientation or pronounced texture. The XRD patterns demonstrate a decrease in the intensity of the (002)α lines from sample 1 to sample 4 relative to the intensity of other α-phase lines. This indicates a decrease in the sharpness of the tangent-oriented prism texture. Consequently, there is a slight decrease in the contact modulus of elasticity (*E*), measured in the tangential direction, from sample 1 to sample 4. This is consistent with the well-known fact that the α-phase exhibits the maximum *E* value along the <001> direction [27].

In our view, the dominant high-modulus orientation <001> in the direction of the contact modulus of elasticity measurements results in average modulus values (ranging from 103 to 110 GPa) that are close to or even above the upper values typical for Ti—3Al—2.5V alloy products (ranging from 95—105 GPa) [2].

Conclusions

1. The study demonstrates that an increase in the number of α + β-area extrusions, from tube *1* to tube *4*, leads to a reduction in the volume fraction of the primary α-phase and an increase in the volume fraction of the β-transformed structure due to end-of-extrusion temperature rise caused by more intense deformation heating of the die and mandrel.

2. Furthermore, the investigation reveals that the elevation of the final extrusion temperature from tube *1* to tube *4* results in a distinctive decrease in the volume fraction of the residual β-solid solution and a reduction in the "sharpness" of the α-phase tangential texture.

3. Additionally, it was observed that the aforementioned changes in the structure and phase state, from sample *1* to sample *4*, have an impact on the contact modulus of elasticity and microhardness.

4. These established relationships provide valuable insights for adjusting the process variables in the multiple Ti—3Al—2.5V alloy tube extrusion.

References

1. Ilyin A.A., Kolachev B.A., Polkin I.S. Titanium alloys. Composition, structure, properties: Reference book. Moscow: VILS—MATI, 2009. 520 p. (In Russ.).
Ильин А.А., Колачев Б.А., Полькин И.С. Титановые сплавы. Состав, структура, свойства: Справочник. М.: ВИЛС—МАТИ, 2009. 520 с.
2. Pumpyanskiy D.A., Illarionov A.G, Vodolazskiy F.V., Kosmatskiy Y.I., Popov A.A. Promising titanium alloys for manufacture of cold-worked pipes. *Metallurg.* 2023;1:37—48.
https://doi.org/10.52351/00260827_2023_01_37
Пумпянский Д.А., Илларионов А.Г., Водолазский Ф.В., Космацкий Я.И., Попов А.А. Перспективные сплавы титана для изготовления холоднодеформированных труб. *Металлург.* 2023;1:37—48.
https://doi.org/10.52351/00260827_2023_01_37
3. Romantcev B.A., Goncharuk A.V., Aleshchenko A.S., Gamin Yu.V. Production of thick-wall hollow profiles and tubes made of titanium alloys by screw rolling. *Izvestiya. Non-Ferrous Metallurgy.* 2015;(4):38—41. (In Russ.).
https://doi.org/10.17073/0021-3438-2015-4-38-41
Романцев Б.А., Гончарук А.В., Алещенко А.С., Гамин Ю.В. Получение полых толстостенных профилей и труб из титановых сплавов методом винтовой прокатки. *Известия вузов. Цветная металлургия.* 2015;(4):38—41.
https://doi.org/10.17073/0021-3438-2015-4-38-41
4. Pilipenko S.V. Analysis of the influence of cold pipe rolling technological factors on the change in Q-factor distribution along the deformation cone. *Izvestiya. Non-Ferrous Metallurgy.* 2019;(3):30—35. (In Russ.).
https://doi.org/10.17073/0021-3438-2019-3-30-35
Пилипенко С.В. Анализ влияния технологических

факторов процесса холодной прокатки труб на изменение распределения Q-фактора вдоль конуса деформации. *Известия вузов. Цветная металлургия*. 2019;(3):30—35.
https://doi.org/10.17073/0021-3438-2019-3-30-35

5. Boyer R., Welsch G., Collings E.W. Materials roperties Handbook: Titanium alloys. ASM Int., The Material Information Society, 1994. 1176 p.
6. Chen S., Li X., Xu D. Manufacture of Gr9 titanium alloy tube for small size and extra-thin wall. In: *Chinese Materials Conference. High Performance Structural Materials*. 2018. P. 531—538.
https://doi.org/10.1007/978-981-13-0104-9_56
7. Pyshmintsev I.Y., Kosmatskii Y.I., Filyaeva E.A., Illarionov A.G., Barannikova N.A. Alloy Ti—3Al—2.5V hot-extruded pipe metal structure and properties. *Metallurgist*. 2018;62(3-4):374—379.
https://doi.org/10.1007/s11015-018-0671-5
Пышминцев И.Ю., Космацкий Я.И., Филяева Е.А., Илларионов А.Г., Водолазский Ф.В., Баранникова Н.А. Структура и свойства металла горячепрессованной трубы из сплава Ti—3Al—2,5V. *Металлург.* 2018;4:70—75.
8. Li H., Wei D., Zhang H.Q., Yang H., Zhang D., Li G.J. Tooling design—related spatial deformation behaviors and crystallographic texture evolution of high-strength Ti—3Al—2.5V tube in cold pilgering. *The International Journal of Advanced Manufacturing Technology*. 2019;104: 2851—2862.
https://doi.org/10.1007/s00170-019-04151-w
9. Yang Q., Hui S., Ye W., Xu Z., Dai C., Lin Y. Effect of "Q" ratio on texture evolution of Ti—3Al—2.5V alloy tube during rolling. *Materials*. 2022;15(3):817.
https://doi.org/10.3390/ma15030817
10. Nikol'skii L.A., Figlin S.Z., Boitsov V.V., Kalpin Y.G., Baharev A.V. Hot stamping and extrusion of titanium alloys. Moscow: Mashinostroenie, 1975. 285 p. (In Russ.).
Никольский Л.А., Фиглин С.З., Бойцов В.В., Калпин Ю.Г., Бахарев А.В. Горячая штамповка и прессование титановых сплавов. М.: Машиностроение, 1975. 285 с.
11. Kosmatskiy Ya.I., Fokin N.V., Filyaeva E.A., Barichko B.V. Deformation ability research of the titanium alloy Ti—3Al—2.5V and the assessment of the technological capability production of hot-extrusion tube from him. *Titan*. 2016;2(52):18—22. (In Russ.).
Космацкий Я.И., Фокин Н.В., Филяева Е.А., Баричко Б.В. Исследование деформационной способности титанового сплава Ti—3Al—2,5V и оценка технологической возможности изготовления из него горячепрессованных труб. *Титан.* 2016;2(52): 18—22.
12. Kosmatskiy Ya.I., Filyaeva E.A., Fokin N.V., Yakovleva K.Yu. Determination of the production possibilities to preparing a new form of seamless TREX pipes of Ti—3Al—2.5V alloy. *Kachestvo v obrabotke materialov.* 2016;2:15—22. (In Russ.).
Космацкий Я.И., Филяева Е.А., Фокин Н.В., Яковлева К.Ю. Определение технологической возможности изготовления нового вида бесшовных труб TREX из титанового сплава Ti—3Al—2.5V. *Качество в обработке материалов*. 2016;2:15—22.
13. Tarin P., Corral N., Simon A.G. Evolution of alpha-beta transformation in Ti—3Al—2,5V alloy. Microstructural changes and properties obtained. In: *Proceedings of the 12th World Conference on Titanium*. Beijing: Science Press., 2012. Vol. 1. P. 481—484.
14. Illarionov A.G., Vodolazskiy F.V., Barannikova N.A., Kosmatskiy Y.A., Khudorozhkova Y.V. Influence of phase composition on thermal expansion of Ti—0.4Al, Ti—2.2Al—2.5Zr and Ti—3Al—2.5V alloys. *Journal of Alloys and Compounds*. 2021;857:158049.
https://doi.org/10.1016/j.jallcom.2020.158049
15. Illarionov A.G., Kosmatskii Y.I., Filyaeva E.A. Vodolazskii F.V., Barannikova N.A., Experimental determination of temperature parameters for evaluating the possibility of manufacturing alloy Ti—3Al—2.5V hot-extruded tubes. *Metallurgist*. 2017;9-10(60):983—988.
https://doi.org/10.1007/s11015-017-0396-x
Илларионов А.Г., Космацкий Я.И., Филяева Е.А., Водолазский Ф.В., Баранникова Н.А. Экспериментальное определение температурных параметров для оценки возможности изготовления горячепрессованных труб из сплава Ti–3Al–2,5V. *Металлург.* 2016;9:83—87.
16. Anoshkin N.F., Borisova E.A., Bochvar G.A., Brun M.Ya., Glazunov S.G., Kolachev B.A., Korobov O.S., Malkov A.V., Moiseev V.N., Notkin A.B. and etc. Metallography of titanium alloys. Moscow: Metallurgiya, 1980. 464 p. (In Russ.).
Аношкин Н.Ф., Борисова Е.А., Бочвар Г.А., Брун М.Я., Глазунов С.Г., Колачев Б.А., Коробов О.С., Мальков А.В., Моисеев В.Н., Ноткин А.Б. и др. Титановые сплавы. Металлография титановых сплавов. М.: Металлургия, 1980. 464 с.
17. Rietveld H.M. A profile refinement method for nuclear and magnetic structures. *Journal of Applied Crystallography*. 1969;2:65—71.
18. Oliver W.C., Pharr G.M. An improved technique for determining hardness and elastic modulus using load and displacement sensing indentation experiments. *Journal of Materials Research*. 1992;7(6):1564—1583.
https://doi.org/10.1557/JMR.1992.1564
19. Shao G., Miodownik A.P., Tsakiropoulos P. ω-phase

formation in V—Al and Ti—Al—V alloys. *Philosophical Magazine A*. 1995;71(6):1389—1408.
20. Aurelio G., Fernandez Guillermet A., Cuello G.J., Campo J. Metastable Phases in the Ti—V System: Pt. I. Neutron Diffraction study and assessment of structural properties. *Metallurgical and Materials Transactions A*. 2002;33A:1307—1317. https://doi.org/10.1007/s11661-002-0057-x
21. Zhelnina A.V., Kalienko M.S., Illarionov A.G., Shchetnikov N.V. Transformation of the structure and parameters of phases during aging of a titanium Ti—10V—2Fe—3Al alloy and their relation to strengthening. *Fizika metallov i metallovedenie*. 2020;121(12):1220—1226. (In Russ.). https://doi.org/10.1134/S0031918X20120133
Желнина А.В., Калиенко М.С., Илларионов А.Г., Щетников Н.В. Трансформация структуры, параметров фаз при старении сплава титана Ti-10V—2Fe—3Al и их связь упрочнением. *Физика металлов и металловедение*. 2020;121(12):1220—1226. https://doi.org/10.1134/S0031918X20120133
22. Fedulov V.N. Prediction of the efficiency of thermal hardening of titanium alloys, *Lit'ye i metallurgiy*a. 2006; 1(37):130—135. (In Russ.).
Федулов В.Н. Прогнозирование эффективности термического упрочнения титановых сплавов. *Литье и металлургия*. 2006;1(37):130—135.
23. Forney C.E., Meredith S.E. Ti—3Al—2.5V seamless tubing engineering guide. Sandvik special Metals Corp., Kennewick, Wash., USA, 1990. 3rd ed. 144 p.
24. Loginov Y.N., Semenov A.P. Changing the temperature of the tool during hot pressing of copper and brass bars. *Kuznechno-shtampovochnoe proizvodstvo. Obrabotka materialov davleniem*. 2006;4:10—13. (In Russ.).
Логинов Ю.Н., Семенов А.П. Изменение температуры инструмента при горячем прессовании прутков из меди и латуни. *Кузнечно-штамповочное производство. Обработка материалов давлением*. 2006;4:10—13.
25. Loginov Yu.N. Pressing as a method of intense deformation of metals and alloys. Yekaterinburg: UrFU, 2016. 156 p. (In Russ.). https://elar.urfu.ru/bitstream/10995/40656/1/978-5-7996-1623-6_2016.pdf
Логинов Ю.Н. Прессование как метод интенсивной деформации металлов и сплавов. Екатеринбург: Изд-во УрФУ, 2016. 156 с. https://elar.urfu.ru/bitstream/10995/40656/1/978-5-7996-1623-6_2016.pdf
26. Weiss I., Semiatin S.L. Thermomechanical processing of alpha titanium alloys — an overview. *Materials Science and Engineering A*. 1999;263:243—256. https://doi.org/10.1016/S0921-5093(98)01155-1
27. Zwicker U. Titan und titanlegierungen. Berlin, Heidelberg: Springer-Verlag, 1974. 717 p. https://doi.org/10.1007/978-3-642-80587-5

Information about the authors

Anatoly G. Illarionov – Cand. Sci. (Eng.), Associate Professor of the Department "Heat Treatment and Physics of Metals", Ural Federal University named after the First President of Russia B.N. Yeltsin (UrFU); Research Scientist, Institute of Metal Physics named after M.N. Mikheev of the Ural Branch of the Russian Academy of Sciences.
http://orcid.org/0000-0002-7571-1179
E-mail: a.g.illarionov@urfu.ru

Fedor V. Vodolazskiy – Cand. Sci. (Eng.), Associate Professor of the Department "Heat Treatment and Physics of Metals", UrFU.
http://orcid.org/0000-0002-6311-131X
E-mail: f.v.vodolazskiy@urfu.ru

Svetlana M. Illarionova – Head of the Laboratory of the Department "Heat Treatment and Physics of Metals", UrFU.
Scopus-ID: 56572890900
E-mail: s.m.illarionova@urfu.ru

Yaroslav I. Kosmatskiy – Dr. Sci. (Eng.), Deputy General Director for Scientific Work, The Russian Research Institute of the Pipe Industry.
Scopus-ID: 36166718600
E-mail: Kosmatski@rosniti.ru

Информация об авторах

Анатолий Геннадьевич Илларионов – к.т.н., доцент кафедры «Термообработка и физика металлов», Уральский федеральный университет имени первого Президента России Б.Н. Ельцина (УрФУ); науч. сотрудник Института физики металлов им. М.Н. Михеева УрО РАН.
http://orcid.org/0000-0002-7571-1179
E-mail: a.g.illarionov@urfu.ru

Федор Валерьевич Водолазский – к.т.н., доцент кафедры «Термообработка и физика металлов», УрФУ.
http://orcid.org/0000-0002-6311-131X
E-mail: f.v.vodolazskiy@urfu.ru

Светлана Михайловна Илларионова – зав. лабораторией кафедры «Термообработка и физика металлов», УрФУ.
Scopus-ID: 56572890900
E-mail: s.m.illarionova@urfu.ru

Ярослав Игоревич Космацкий – д.т.н., зам. ген. директора по научной работе, АО «Русский научно-исследовательский трубный институт».
Scopus-ID: 36166718600
E-mail: Kosmatski@rosniti.ru

Natalia A. Shirinkina – Head of the Department, JSC "Ural Works of Civil Aviation".
Scopus-ID: 57193270781
E-mail: nata382@yandex.ru

Maksim A. Shabanov – Research Engineer of the Department "Heat Treatment and Physics of Metals", UrFU.
http://orcid.org/0009-0008-6725-1724
E-mail: m.a.shabanov@urfu.ru

Наталья Александровна Ширинкина – начальник отдела АО «Уральский завод гражданской авиации».
Scopus-ID: 57193270781
E-mail: nata382@yandex.ru

Максим Александрович Шабанов – инженер исследователь кафедры «Термообработка и физика металлов», УрФУ.
http://orcid.org/0009-0008-6725-1724
E-mail: m.a.shabanov@urfu.ru

Contribution of the authors

A.G. Illarionov – basic concept, problem statement, paper authoring, conclusions.

F.V. Vodolazsky – XRD and EDS analysis and image processing.

S.M. Illarionova – metallographic analysis and processing of the results.

Ya.I. Kosmatsky – acquisition and analysis of manufacturing information.

N.A. Shirinkina – processing of the manufacturing process observations, and data structuring.

M.A. Shabanov – durometry analysis and processing of the results.

Вклад авторов

А.Г. Илларионов – формирование основной концепции, постановка цели и задачи исследования, подготовка текста, формулировка выводов.

Ф.В. Водолазский – постановка задач рентгеноструктурного фазового анализа, его проведение и обработка результатов.

С.М. Илларионова – постановка задач металлографического анализа, его проведение и обработка результатов.

Я.И. Космацкий – организация сбора производственных параметров и их анализ.

Н.А. Ширинкина – обработка наблюдений в производственном процессе, упорядочение полученных данных.

М.А. Шабанов – постановка задач дюрометрического анализа, его проведение и обработка результатов.

The article was submitted 26.04.2023, revised 22.06.2023, accepted for publication 23.06.2023

Статья поступила в редакцию 26.04.2023, доработана 22.06.2023, подписана в печать 23.06.2023

UDC 621.74 + 669.018
https://doi.org/10.17073/0021-3438-2023-4-70-86

Research article
Научная статья

Liquid matrix SHS manufacturing and heat treatment of Al–Mg composites reinforced with fine titanium carbide

A.R. Luts, Yu.V. Sherina, A.P. Amosov, A.D. Kachura

Samara State Technical University
244 Molodogvardeyskaya Str., Samara 443100, Russia,

✉ Alexander P. Amosov (egundor@yandex.ru)

Abstract: Aluminum matrix composites reinforced with ultra-fine refractory titanium carbide feature a unique combination of properties. They are promising structural materials. Self-propagating high-temperature synthesis (SHS) is an affordable and energy-saving composite-making process. It involves the exothermic reaction between titanium and carbon (or their compounds) directly in the melt. We studied the properties of SHS composites based on the AMg2 and AMg6 commercially available alloys reinforced with 10 wt.%TiC. We investigated the macro- and microstructure of the samples with XRD and EDS analysis. It was found that the β-phase is separated from α-solid solution of aluminum as early as the air cooling stage. We conducted experiments aimed at studying the effects of additional heating on the sample structure and properties and found the optimal temperature and time values. We also proposed a phenomenological model of the structural transformation sequence. We compared the physical, mechanical, and manufacturing properties and corrosion resistance of the original cold-hardened AMg2N and AMg6N alloys and the composites before and after heat treatment. It was found that additional heating reduces porosity and maintains electrical conductivity. It was also found that the compressive strength and relative strain of the composite based on the AMg2 alloy change insignificantly, while for the AMg6-based composite the reduction is more significant. Heat treatment increases the composite hardness while maintaining sufficient plastic deformation. It is confirmed by the measured values of the relative strain and the reduction ratio close to that of the original matrix alloys. It was also found that the composites retain high resistance to carbon dioxide and hydrogen sulfide corrosion.

Keywords: aluminum matrix composite (AMCs), aluminum, melt, titanium carbide, self-propagating high-temperature synthesis (SHS).

For citation: Luts A.R., Sherina Yu.V., Amosov A.P., Kachura A.D. Liquid matrix SHS manufacturing and heat treatment of Al–Mg composites reinforced with fine titanium carbide. *Izvestiya. Non-Ferrous Metallurgy.* 2023;29(4):70–86.
https://doi.org/10.17073/0021-3438-2023-4-70-86

Жидкофазное получение методом СВС и термическая обработка композитов на основе алюминиево-магниевых сплавов, упрочненных высокодисперсной фазой карбида титана

А.Р. Луц, Ю.В. Шерина, А.П. Амосов, А.Д. Качура

Самарский государственный технический университет
443100, Россия, г. Самара, ул. Молодогвардейская, 244

✉ Александр Петрович Амосов (egundor@yandex.ru)

Аннотация: Алюмоматричные композиционные материалы, дисперсно-упрочненные тугоплавкой фазой карбида титана, характеризуются уникальным сочетанием свойств и относятся к группе перспективных конструкционных материалов. Одним из наи-

более доступных и энергосберегающих методов их получения является самораспространяющийся высокотемпературный синтез (СВС), основанный на экзотермическом взаимодействии титана и углерода (или их соединений) непосредственно в расплаве. В работе приводятся результаты СВС композиционных материалов на основе промышленных сплавов АМг2Н и АМг6Н, упрочненных 10 мас.%TiC. Исследованы макро- и микроструктура полученных образцов, проведены микрорентгеноспектральный и рентгенофазовый анализы. Установлено, что уже в процессе охлаждения на воздухе после синтеза происходит выделение β-фазы из α-твердого раствора алюминия. Проведены эксперименты по изучению влияния дополнительного нагрева на структуру и свойства образцов, определены оптимальные температурно-временные параметры, предложена феноменологическая модель последовательности структурных превращений. Выполнен сравнительный анализ физических, механических, технологических свойств и коррозионной стойкости исходных сплавов АМг2Н и АМг6Н в нагартованном состоянии и композиционных материалов на их основе до и после термической обработки. Установлено, что проведение дополнительного нагрева способствует снижению пористости и сохранению уровня электропроводности относительно этих показателей для литых композитов. Выявлено, что прочность на сжатие и относительная деформация для композита на основе сплава АМг2 изменяются незначительно, тогда как для материала на основе АМг6 их падение более существенно. При этом термическая обработка позволяет повысить твердость материалов, сохранив достаточную способность композитов к пластической деформации, что подтверждается значениями степени деформации и коэффициента уковки, близкими к уровню матричных сплавов. Также установлено, что синтезированные композиционные материалы сохраняют высокий уровень устойчивости к углекислотной и сероводородной коррозии.

Ключевые слова: алюмоматричный композиционный материал (АМКМ), алюминий, расплав, карбид титана, самораспространяющийся высокотемпературный синтез (СВС).

Для цитирования: Луц А.Р., Шерина Ю.В., Амосов А.П., Качура А.Д. Жидкофазное получение методом СВС и термическая обработка композитов на основе алюминиево-магниевых сплавов, упрочненных высокодисперсной фазой карбида титана. *Известия вузов. Цветная металлургия*. 2023;29(4):70–86. https://doi.org/10.17073/0021-3438-2023-4-70-86

Introduction

Aluminum matrix composites (AMCs) reinforced with fine refractory titanium carbide (from hundredths of a percent to 50 wt.%) possess increased strength while retaining high plasticity, low specific weight, and good corrosion resistance as reported by Mikheyev R. et al. [1]. This unique combination of properties makes the material suitable for making connecting rod components, bearings, and other wear-resistant parts [2; 3].

There are many AMCs manufacturing technologies. As mentioned by Nath H. et al. [4], these technologies can be divided into solid matrix and liquid matrix processes. Amosov A. et al. [5] note that the solid matrix processes are long and energy-consuming. On the other hand, conventional liquid matrix processes are unable to add a significant amount of reinforcing phase into the melt. This is due to low fluidity, and may result in undesirable chemical reactions between the matrix and the added components.

The new AMCs manufacturing technology is self-propagating, high-temperature synthesis (SHS). It is simple and suitable for virtually any melting furnace with a relatively low level of energy consumption. The SHS process is an exothermic reaction of initial reagents (powders of titanium and carbon or their compounds) in aluminum melt, producing titanium carbide as multiple dispersed particles [5—8].

Many recent studies have focused on increasing the fineness of the carbide phase particles and adding alloying elements to the matrix, since these have a positive effect on the AMCs properties. For example, Zhou D. et al. [9] studied the following aluminum melt (wt.%.): 5 Cu, 0.45 Mn, 0.3 Ti, 0.2 Cd, 0.2 V, 0.15 Zr, and 0.04 B. They added aluminum, titanium, and carbon nanotubes in the amounts of 0.1—1.0 wt.%. It was found that the formation of 0.5 wt.% of nanosized TiC particles increases composite strength to 540 MPa, and relative elongation, to 19 % (11 and 188 % growth compared to the initial matrix alloy). Tian W. et al. [10] used the same matrix to manufacture composites with 0.5 wt.% of TiC (particle size d = 97 nm), and 1, 3, and 5 wt.% of TiC (d = 1.88 μm). It was found that at t = 180 °C and under a 20 N load, the wear resistance of the nanoscale composite is 16.5 % higher than that of the composite reinforced with 5 wt.% of titanium carbide microparticles.

Amosov A. et al., Samara State Technical University [5] showed SHS process applicability to Al—TiC

mixtures (with powdered titanium and carbon). The reinforcing phase content is up to 20 % with an initial particle size of about 2—4 μm. Luts A. et al. [11] found that the addition of 5 wt.% of Na_2TiF_6 reduces the carbide particle size in the Al—10%TiC composite to ultra-fine (less than 1 μm). As a result, the strength after casting is increased by more than 80 % (from 115 to 200 MPa). The authors [12] manufactured Al—5%Cu—10%TiC, Al—5%Cu—2%Mn—10%TiC, and other heavy-duty composites containing an ultra-fine carbide phase.

Many recent works study alloy reinforcement by carbide phase both formed in the melt by SHS or added [13—15]. As a rule, the base metals are heat-treatable alloys. After reinforcement, the metal is treated with precipitation hardening (hardening + aging). Cho Y. et al. [16] showed that SHS applies to the highly dispersed carbide phase (6, 10, and 12 vol.%) in A2024 (Al—4.4%Cu—1.5%Mg). The sample containing 12 vol.% TiC, after extrusion, annealed at 400 °C for 20 h, quenched for 1 h at t = 500 °C, and aged at 190 °C for 8 h, showed the greatest increase in modulus of elasticity and tensile strength. This reached up to 93 GPa and 461 MPa, respectively. Ramakoteswara Rao V. et al. [17; 18] noted that a sample with 8 wt.% of TiC particles after adding 2—10 wt.% of TiC particles of about 2 μm to the AA7075 foundry alloy (Al—5.8%Zn—2.4%Mg), subsequent homogenization at t = 450 °C for 2 h, and aged at 121 °C for 24 h, increased its tensile strength from 400 to 600 MPa, and hardness, from 110 to 200 HV.

Nevertheless, some works indicate that heat treatment of AMCs does not always improve strength. Chen C. et al. [19] studied the aging behavior of the Al6061 alloy (Al—Mg—Si) reinforced with 2 % TiC particles (d = 40÷50 μm) at t = 160 °C. They established that the reinforcing particles prevent the formation of Guinier-Preston zones and strengthening metastable Mg—Si phases in the aluminum matrix. As a result, after T6 heat treatment, the max hardness (75.8 HV) of the Al6061—TiC composite was reached after 8 h of aging. This was much lower than that of the Al6061 matrix alloy after 18 h of aging (123 HV).

The review [20] summarizes the quenching and subsequent aging of Al—Cu—Mg—SiC, Al—Mg—Si—Cu—SiC, Al—Mg—Si—Cu—B4C, and Al—Zn—Mg—Cu—SiC AMCs reinforced by silicon carbide and manufactured with both solid matrix and liquid matrix processes. In general, the aging patterns of composites and aluminum alloys are different. The sequence of precipitation hardening phases and phase composition of the matrix material may vary, while the max AMCs hardness and strength are achieved in a shorter time. Furthermore, the hardening of the composites generally results in lower hardness than expected by "adding" the results of the precipitation hardening of the aluminum alloy and the matrix strengthening by reinforcing particles.

There are highly interesting studies which show that by changing the composition and structure of interfacial boundaries and by improving the matrix-to-filler bonding, it becomes possible to apply heat treatment to alloys considered unsuitable for precipitation hardening. One example is the study by Hashim J. et al. [21]. They reported that quenching at 550 °C for 20 min with hot water cooling and subsequent aging at 160 °C for 30 min of the non-heat-treatable AMg1 alloy with 2.5 wt.% SiC (d = 3 μm) increases the hardness to 1040—1200 HB, and tensile strength, to 153 MPa. One of the reasons may be the presence of magnesium in the alloy. Magnesium is often used as a surface active additive that segregates at the phase interface and reduces its energy [22].

For example, Contreras A. et al. [23] studied the interaction between titanium carbide substrate and Al—Mg melt at 900 °C. It was found that by increasing the Mg content from 1 to 20 % in the base aluminum, the wetting of the ceramic phase can be significantly improved by reducing the surface tension of aluminum drops. Magnesium additions also significantly strengthen aluminum alloys. In particular, Shu S. et al. [24] reported that the addition of 14 % Mg to SHS alloys manufactured by hot pressing increases the compressive strength of the Al—TiC composite by as much as 353 MPa.

This review confirms that magnesium significantly increases the efficiency of alloy hardening by adding titanium carbide. Gulyayev A. et al. [25] reported that such reinforcement is most appropriate for Al—Mg alloys (magnalium) which are known to have good formability and weldability, albeit relatively low strength and hardness. The most common alloys contain from 1 to 6 wt.% Mg, and micro amounts of other alloying elements (Fe, Si, Mn, Ti, Cu, Be, etc).

The Mg solubility in Al is 17.4 % at t = 450 °C and about 1.4 % at room temperature. Nevertheless, non-equilibrium solidification conditions in alloys containing as low as 1—2 % Mg may result in the formation of eutectic β phase inclusions of the Al_3Mg_2 (Mg_5Al_8) composition.

When solidified, transition metals form supersaturated solid solutions with aluminum [26; 27]. However, their low content does not lead to a significant increase in strength. Therefore, the formation of one more ultra-fine titanium carbide phase in magnalium may have a positive effect explained both by its hardening by reinforcing perticles and changing the sequence and the rate of structural transformations during the solidification and heat treatment caused by lattice micro-distortions.

The reinforcement results largely depend on the chemical composition of the alloy (the contents of magnesium and alloying elements). The purpose of this study is to obtain two composite materials by the SHS process and analyze the effects of heat treatment on their structure and properties. We studied the addition of titanium carbide to the AMg_2 (10%TiC) and AMg_6 (10%TiC) alloys.

Methods and materials

We used AMg2 (1520) and AMg6 (1560) alloy grades from Sammet (Russia) manufactured to GOST 4784-2019 as the melted matrix. In order to produce the charge mixture, we mixed powdered titanium (TPP-7 grade, TU 1715-449-05785388 Spec.) and carbon (P-701, GOST 7585-86) in a stoichiometric ratio for the Ti + C = TiC SHS reaction with Na_2TiF_6 (GOST 10561-80) added in amount of 5 % of the charge weight. The mixture was then divided into 3 equal parts wrapped in aluminum foil. Each was added to the AMg2 or AMg6 melts at 900 °C in a graphite crucible placed in a PS-20/12 melting furnace (made in Russia), in order to induce the SHS reaction and make the desired composites.

In the aims of studying the microstructure, we etched the samples with a 50 % HF + 50 % HNO_3 solution for 10—15 sec. Then we analyzed the samples with a JSM-6390A scanning electron microscope (Jeol, Japan) with a JSM-2200 energy-dispersive spectroscopy (EDS) module.

We also used XRD for phase identification. The XRD instrument was an ARL X'trA *X*-ray diffraction system (Thermo Scientific, Switzerland) with the CuK_α radiation and continuous scanning in the 2θ = = 20÷80° angle range at 2 deg/min. The HighScore Plus software (PANalytical B.V., Netherlands) was used to analyze the XRD patterns. The AMCs samples were heat treated in a SNOL lab furnace (temperature up to 1300 °C).

We measured the sample density by hydrostatic weighing on a VK-300 scale (made in Russia), accuracy class 4, GOST 20018-74. The demineralized water density was assumed to be 0.99733 g/cm^3 at the room air temperature of 24 °C. For dimensional control and composition analysis, we used a MIM 43 optical metallographic microscope (made in Russia) and the SIAMS 800 image processing software.

We measured AMCs electrical conductivity using a VE-26NP eddy current structurescope (made in Russia) according to GOST 27333-87. The hardness of the samples was measured using a TSh-2M hardness tester (made in Russia) according to GOST 9012-59. The impression diameter was defined using a Motic DM-111 microscope (made in Russia) and the Motic Educator image analysis software. For sample microhardness testing, a PTM-3 standard microhardness tester (made in Russia) was used according to GOST 9450-76. The instrument drives a square diamond pyramid (136° vertex angle). The penetrator load was 100 g.

We performed compression tests on the type III samples (d_0 = 20 mm) according to GOST 25.503-97. The relative strain and reduction ratio was established as specified in GOST 8817-82.

Corrosion resistance was evaluated according to GOST 13819-68 in a Coat Test 3.3.150.150 autoclave under the following conditions: 5 % NaCl aqueous solution; CO_2 (1 Pa) + H_2S (0.5 MPa) + N_2 (3.5 MPa) gas phase at 80 °C 240 h: 5 MPa total pressure. The corrosion resistance factors were calculated according to GOST 9.908-85. We used a Universal-1B tribology tester (made in Russia) for tribology testing as follows:

— friction type: boundary friction (sliding);
— block-on-ring contact arrangement;
— counterbody material: 40H grade steel;

— lubricant: Shell Helix Ultra SAE 5W-40 synthetic engine oil;
— normal contact load: 380 N;
— counterbody rpm: 600 (average linear velocity at the contact area: 0.157 m/s);
— test period: 30 min (or until seizure).

Results and discussion

The powders mixtures used to make both composites in the AMg2 or AMg6 melts at 900 °C produced an intense, rapid SHS reaction with bright flashes. The fractures of the synthesized samples were homogeneously gray and lacked any foreign inclusions or residues of unreacted charge.

Composite manufacturing and heat treatment AMg2–10%TiC

Figure 1 shows the microstructure of AMg2—10%TiC composite manufactured with SHS. The process produces a large number of both small sintered agglomerates, and ultra-fine rounded particles larger than 180 nm. XRD analysis revealed the presence of Al, Ti, C, and Mg (Fig. 2). XRD analysis also identified the presence of the required TiC phase (Fig. 3). EDS analysis indicated a presence of Mg, so the β-phase may be also present but its amount is too small to be detected by XRD.

XRD processing identified the presence of a carbide phase (8 wt.%). This is an acceptable level, considering some inhomogeneity of its distribution. The average grain size reduced from 9.64 (±4.82) μm in the matrix to 1.31 (±0.056) μm in the composite material. It confirms the modifying effect of the carbide phase particles. Measurements showed an increase in hardness from 509 HB for the AMg2 casting alloy to 594 HB for the AMg2—10%TiC composite. It matches the hardness of the hardened AMg2 alloy.

We can conclude that, due to the absence of plastic deformation, the presence of highly dispersed carbide particles increases the hardness.

Next we selected the optimal temperature and time for heat treatment. As noted above, the lean AMg2 alloy does not undergo precipitation hardening after quenching. It consists mainly of a solid solution of magnesium in aluminum. However, as was shown above and by Kurganova Y. et al. [21], heat treatment of the AMg1 composite with a fine phase can produce some new effects.

Taking all the factors into account, we selected the following heat treatment modes: 130, 150, 180, and 350 °C for 1, 2, and 3 h with subsequent still air cooling [28]. The hardness was a quantitative criterion aimed at evaluating the effects of heat treatment. Figure 4 presents the results. The highest value of 676 HB (compared to the initial 594 HB for the foundry composite) is achieved after heating at 150 °C for 2—3 h. Heating at 350 °C does not affect the hardness.

The microstructure and EDS analysis of the AMC samples with the highest hardness (Figs. 5 and 6) show that the carbide particle sizes and chemical composi-

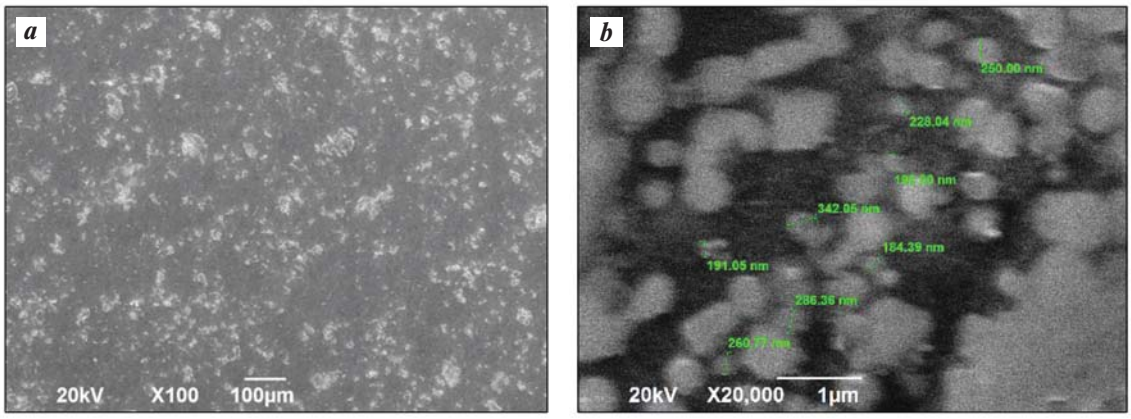

Fig. 1. SEM image of the AMg2–10%TiC composite
a – ×100 magnification, ***b*** – ×20000 magnification

Рис. 1. Микроструктура композиционного материала АМг2–10%TiC
a – увеличение ×100, ***b*** – ×20000

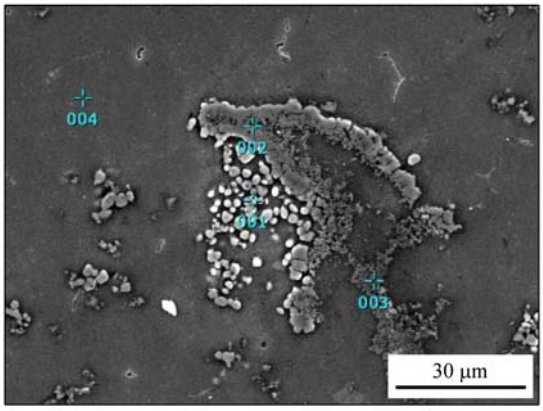

Marker number	Element content, wt.%				
	C	Al	Ti	Mg	F
001	28.01	14.27	57.72	0	0
002	17.97	38.17	38.01	3.49	2.36
003	17.82	47.91	28.71	3.92	1.65
004	0	93.93	0	6.07	0

Fig. 2. EDS analysis of the AMg2–10%TiC composite

Рис. 2. Результаты МРСА композиционного материала AMr2–10%TiC

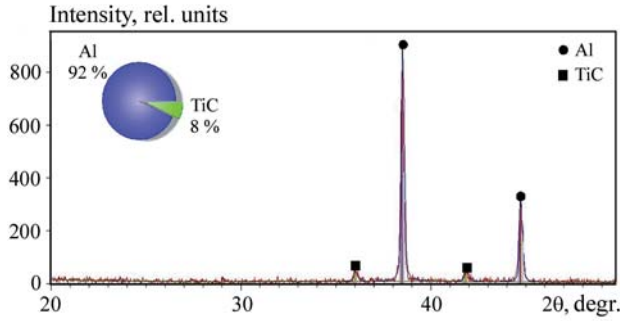

Fig. 3. XRD pattern of the AMg2–10%TiC composite

Рис. 3. Дифрактограмма композиционного материала AMr2–10%TiC

tion are not affected. However, EDS indicates that the result of heat treatment leads both to the appearance of elemental magnesium and XRD peaks of the Al_3Mg_2 β-phase in the amount of 3 wt.%. This means an additional release of magnesium from the solid solution of aluminum (Fig. 7).

We made the following assumption about the sequence of structural transformations before and after heat treatment based on the experimental data. Imme-

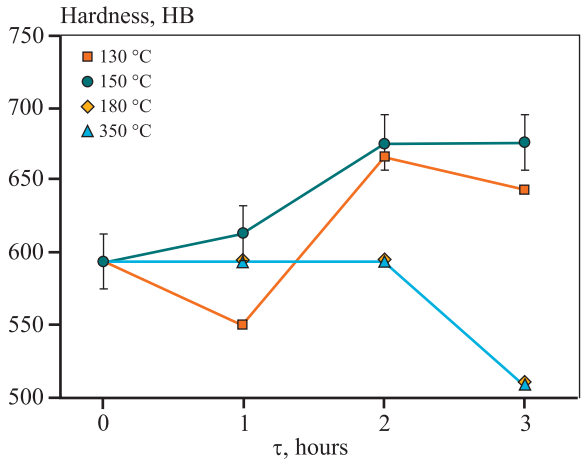

Fig. 4. The hardness variations of the AMg2–10%TiC composite after heat treatment at different temperatures

Рис. 4. Изменение твердости композиционного материала AMr2–10%TiC после дополнительного нагрева при разных температурах

diately after pouring the composite into the mould and during the solidification cooling, the presence of a large number of carbide particles distort the lattice of the matrix and cause high internal stresses. This is due to the formation of the Mg_2Si, $Al_6(Fe, Mn)$, $Al_{15}(Fe, Mn)_2Si_3$ crystallization phases [29]. After solidification, a partial precipitation of the β-phase from the solid solution is possible.

It should be noted that the presence of the Al_3Mg_2 phase can decrease the strength and corrosion resistance, since it precipitates as continuous chains along the grain boundaries [29]. In this case, the large number of dispersed carbide particles prevents the formation of such continuous precipitates, while individual intermetallic β-phase inclusions may increase the hardness. Additional heating at t = 150 °C while the internal stress still applies facilitates the diffusion. Subsequent cooling in air leads to an additional β-phase release, increasing hardness.

There is no change to hardness after heating to 350 °C (see Fig. 4) because a solid solution is formed throughout the entire alloy volume at this temperature. Cooling leads to the same processes as after SHS, and the initial hardness is restored.

Composite manufacturing and heat treatment AMg6–10%TiC

Figure 8 shows the microstructure of the AMg6–10%TiC composite. Compared to the previous case,

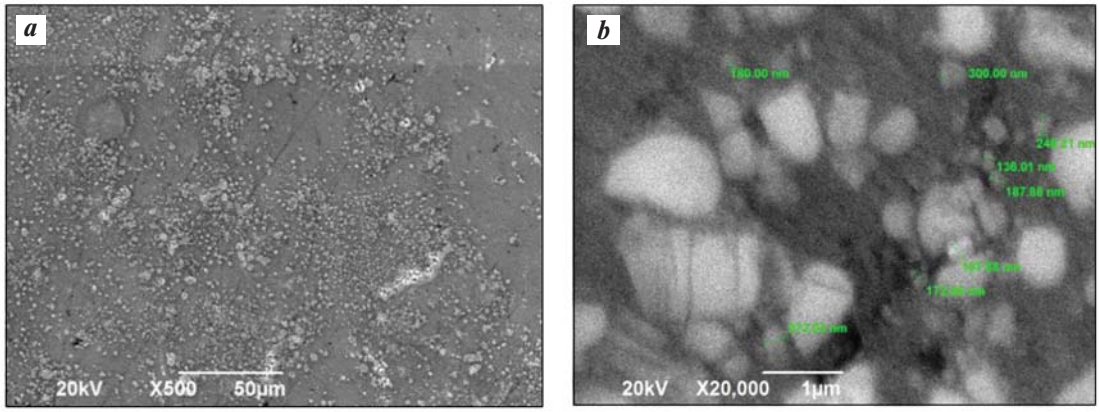

Fig. 5. SEM image of the AMg2–10%TiC composite after additional heating at t = 150 °C for 2 h
a – ×500 magnification, ***b*** – ×20000 magnification

Рис. 5. Микроструктура композиционного материала АМг2–10%TiC после дополнительного нагрева при t = 150 °C в течение 2 ч
a – увеличение ×500, ***b*** – ×20000

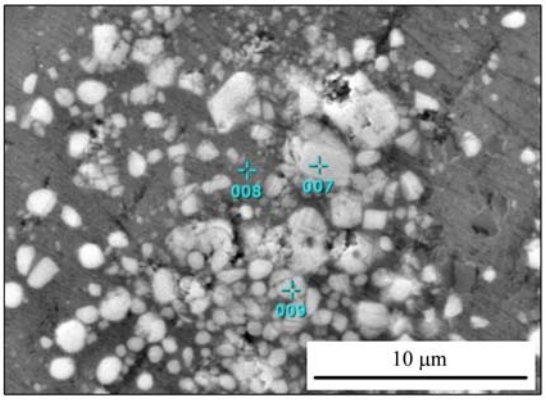

Marker number	Element content, wt.%			
	C	Al	Ti	Mg
007	22.04	13.54	63.19	1.22
008	14.60	75.90	4.88	4.60
009	29.00	38.44	29.89	2.67

Fig. 6. EDS analysis of the AMg2–10%TiC composite after additional heating at t = 150 °C for 2 h

Рис. 6. Результаты МРСА композиционного материала АМг2–10%TiC после дополнительного нагрева при t = 150 °C в течение 2 ч

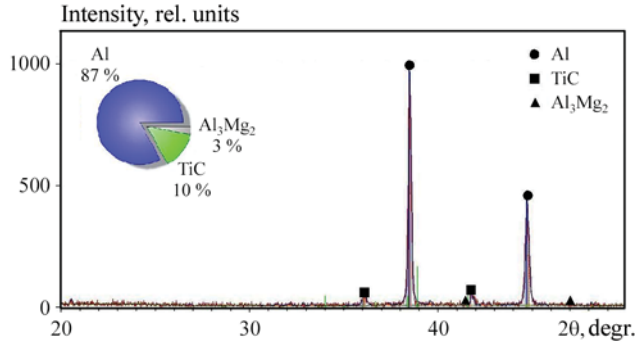

Fig. 7. XRD pattern of the AMg2–10%TiC composite after additional heating at t = 150 °C for 2 h

Рис. 7. Дифрактограмма композиционного материала АМг2–10%TiC после дополнительного нагрева при t = 150 °C в течение 2 ч

carbide phase particles exceeding 130 nm are distributed more uniformly over the alloy volume. This can be explained by the higher magnesium content and, consequently, their higher wettability, and better assimilation.

XRD analysis indicates the presence of the TiC target phase (Figs. 9 and 10), while the presence of magnesium suggests the presence of the β-phase.

The XRD pattern analysis confirms the presence of a carbide phase in the amount of 10 wt.%. Average grain size decreased from 15.8 (±34.3) μm in the matrix alloy to 10.6 (±3.56) μm in the composite. The process increases the hardness from 830 to 909 HB for AMg6—10%TiC casting alloy.

The AMg6 alloy is not a conventional precipitation hardened material. However, the high magnesium content provides the highest strength among all other magnalium alloys. The alloy is usually hardened or is subjected to recrystallization annealing in the

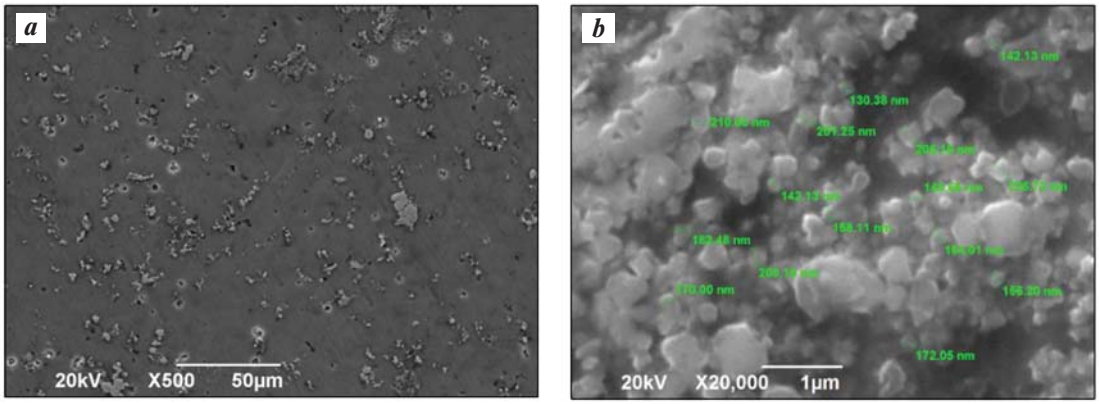

Fig. 8. SEM image of the AMg6–10%TiC composite
a – ×500 magnification, ***b*** – ×20000 magnification

Рис. 8. Микроструктура композиционного материала АМг6–10%TiC
a – увеличение ×500, ***b*** – ×20000

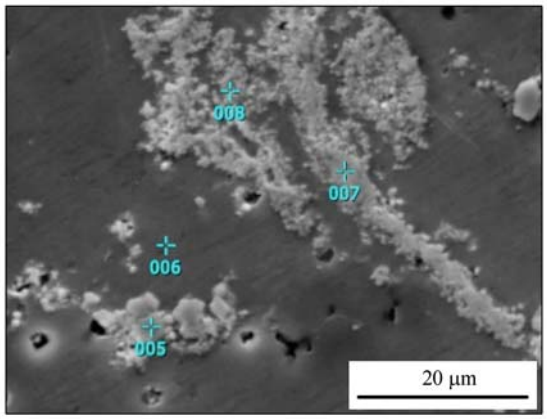

Marker number	Element contents, min., wt.%			
	Al	Ti	C	Mg
005	4.43	90.18	4.74	0.66
006	90.56	0.22	0.15	9.06
007	5.13	88.60	5.46	0.81
008	40.24	51.14	2.76	5.86

Fig. 9. EDS analysis of the AMg6–10%TiC composite

Рис. 9. Результаты МРСА композиционного материала АМг6–10%TiC

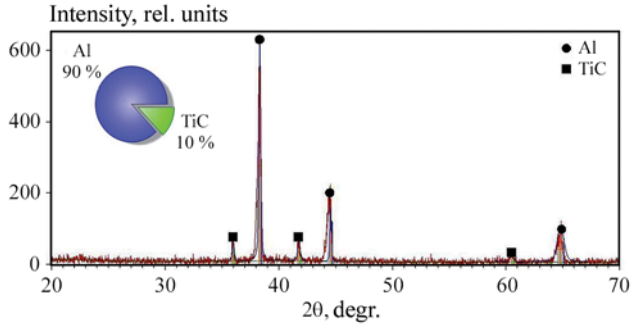

Fig. 10. XRD pattern of the AMg6–10%TiC composite

Рис. 10. Дифрактограмма композиционного материала АМг6–10%TiC

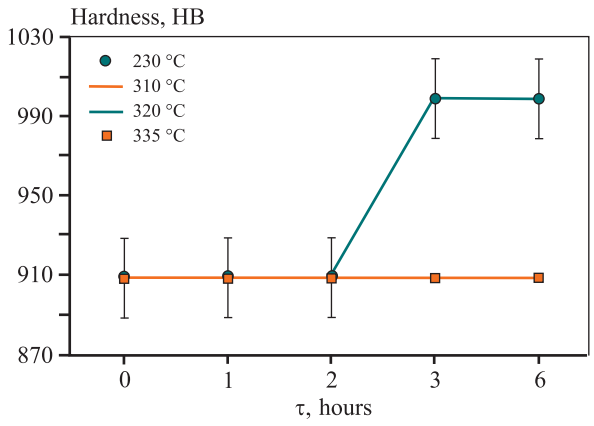

Fig. 11. The hardness changes of the AMg6–10%TiC composite after additional heating at different temperatures

Рис. 11. Изменение твердости композиционного материала АМг6–10%TiC после дополнительного нагрева при разных температурах

310—335 °C temperature range, in order to increase its ductility, with furnace holding time from 30 min to 3 h and air cooling [26].

Kishchik M. et al. [30] studied the effects of different heterogenization annealing modes for the 1565ch alloy containing 5.1—6.0 wt.% Mg and alloying Zr. The tem-

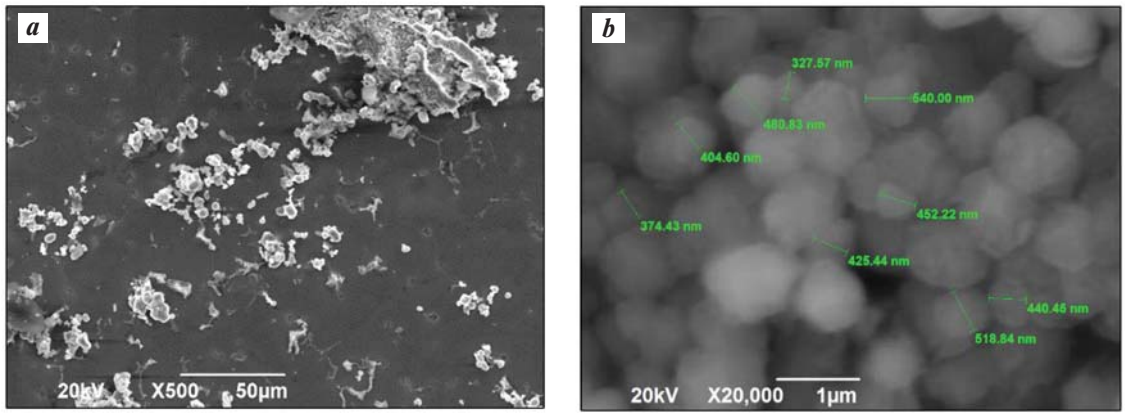

Fig. 12. SEM image of the AMg6–10%TiC composite after additional heating at t = 230 °C for 3 h
a – ×500 magnification, ***b*** – ×20000 magnification

Рис. 12. Микроструктура композиционного материала АМг6–10%TiC после дополнительного нагрева при t = 230 °C в течение 3 ч
a – увеличение ×500, ***b*** – ×20000

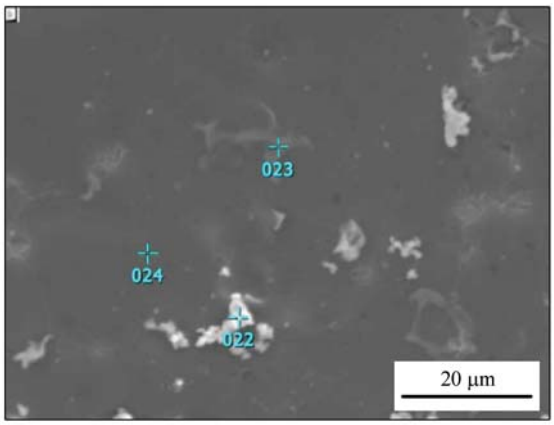

Marker number	Element contents, min., wt.%					
	Al	Ti	C	Mg	Mn	Fe
022	9.92	85.04	3.73	1.31	–	–
023	80.86	–	–	6.75	3.86	8.54
024	93.41	–	–	6.59	–	–

Fig. 13. EDS analysis of the AMg6–10%TiC composite after additional heating at t = 230 °C for 3 h

Рис. 13. Результаты МРСА композиционного материала АМг6–10%TiC после дополнительного нагрева при t = 230 °C в течение 3 ч

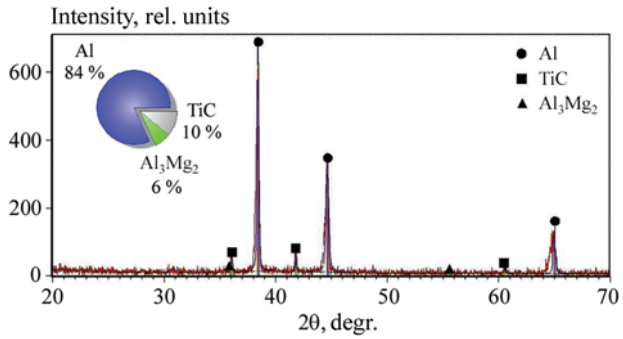

Fig. 14. XRD pattern of the AMg6–10%TiC composite after additional heating at t = 230 °C for 3 h

Рис. 14. Дифрактограмма композиционного материала АМг6–10%TiC после дополнительного нагрева при t = 230 °C в течение 3 ч

perature varied from 130 to 280 °C, and the holding time from 1 to 12 h. The results showed that the formation of homogeneously distributed individual β-phase particles during annealing at t = 230 °C with a 6 h holding time produces a fine-grained structure, and leads to the highest hardness gain.

Considering the above, we selected the following treatment mode for the AMg6—10%TiC composite: heating at t = 230 °C for 1, 3, and 6 h at 310, 320, and 335 °C for 1, 2, and 3 h. Fig. 11 shows the measured hardness values. It indicates that heat treatment in the t = 310÷335 °C range does not increase hardness. Its highest value (999 HB) is achieved after holding at t = 230 °C for 3 and 6 h.

Just like with the first alloy, additional heating at a temperature close to the solubility line contributes to higher hardness.

Figures 12—14 shows the XRD, EDS, and microstructural analysis results of the sample with the highest hardness. XRD analysis showed the presence of not only Al, Ti, C, and Mg, but also Mn and Fe. It may indicate the presence of intermetallic and ceramic phases formed during solidification. However, the primary phase formed after heating is Al_3Mg_2 in the amount of 6 wt.%. It accounts for the hardness increase (Fig. 14).

Properties of AMg2–10%TiC and AMg6–10%TiC composites

We compared the properties of the original cold-hardened alloys with index N, composites without heat treatment (No HT), and composites after additional heating resulting in the highest hardness.

The SHS process is characterized by significant outgassing which can adversely affect the composite properties. For this reason, we initially determined the density (ρ_{test}) and porosity (P) of the samples (Table 1). The ρ_{test} values of the AMCs are slightly higher than those of the original matrix alloys. This confirms the presence of a carbide phase with $\rho = 4.92$ g/cm^3. The reference density (ρ_{ref}) was calculated for the AMCs containing 10 % TiC.

The comparison of the reference and experimental density values indicates that the porosity of the SHS cast samples does not exceed 1%. Heat treatment reduces it to zero, confirming higher adhesive bonding at the phase interfaces.

Then we studied the electrical conductivity. It is an important characteristic of all aluminum alloys (Table 2).

Pan S. et al. [31] reported that only AMCs reinforced with ultra-fine nanophases (such as CNTs, graphene, etc.) can have high electrical conductivity. The possibility of making a conductive material con-

Table 1. **Density and porosity of the original alloys and composites**

Таблица 1. Плотность и пористость сплавов и композиционных материалов

Sample composition	ρ_{test}, g/cm^3	ρ_{ref}, g/cm^3	P, %
AMg2N	2.69	–	–
AMg2—10%TiC (no HT)	2.82	2.797	0.82
AMg2—10%TiC (heating to 150 °C, 2 h)	2.82	2.826	0
AMg6N	2.64	–	–
AMg6—10%TiC (no HT)	2.768	2.739	1
AMg6—10%TiC (heating to 230 °C, 3 h)	2.768	2.768	0
AMg6—10%TiC (heating to 230 °C, 6 h)	2.768	2.768	0

Table 2. **Electrical conductivity of alloys and composites**

Таблица 2. Электропроводность сплавов и композиционных материалов

Sample composition	Electrical conductivity, MSm/m
AMg2N	19.7
AMg2—10%TiC (no HT)	15.4
AMg2—10%TiC (heating to 150 °C, 2 h)	16.6
AMg6N	14.5
AMg6—10%TiC (no HT)	10.57
AMg6—10%TiC (heating to 230 °C, 3 h)	11.2
AMg6—10%TiC (heating to 230 °C, 6 h)	10.98

Table 3. **Mechanical properties and manufacturability of the alloys and composites**

Таблица 3. Механические и технологические свойства сплавов и композиционных материалов

Sample composition	$\sigma_в^*$, MPa	ε^*, %	Hardness, HB	Microhardness, HV	Relative strain,%	Reduction ratio
AMg2N	290	69.19	594	608	32	1.48
AMg2–10%TiC (no HT)	271	59.7	594	736	25	1.33
AMg2–10%TiC (heating to 150 °C, 2 h)	288	61.5	676	745	29	1.41
AMg6N	449	32	830	991	44	1.8
AMg6–10%TiC (no HT)	403	19	909	1020	43	1.62
AMg6–10%TiC (heating to 230 °C, 3 h)	395	14	999	1069	43	1.75

* Uniaxial compression tests.

Table 4. **Corrosion resistance of alloys and composites**

Таблица 4. Коррозионная стойкость сплавов и композиционных материалов

Sample composition	Weight loss, g	Weight loss per unit area, kg/m^2	Sample thickness change, m	Corrosion rate, g/(cm^2·h)	Corrosion depth rate, mm/year
AMg2N	0.6187	0.160	0.058	0.666	0.0021
AMg2–10%TiC (no HT)	0.3686	0.095	0.035	0.416	0.0014
AMg2–10%TiC (heating to 150 °C, 3 h)	0.418	0.108	0.038	0.450	0.0014
AMg6N	0.8935	0.231	0.082	0.962	0.003
AMg6–10%TiC (no HT)	0.5826	0.151	0.057	0.627	0.0021
AMg6–10%TiC (heating to 230 °C, 3 h)	0.8063	0.208	0.075	0.868	0.0027

taining a titanium carbide reinforcing phase is still under study.

The values measured are slightly lower than those of the original alloys due to the presence of the carbide phase. Pan S. et al. [32] confirm this. They reported that an AMC with 3.68 vol.% TiC and aluminum matrix has a higher electrical resistance and, consequently, lower conductivity.

We measured the ultimate strength (σ_B) and relative strain (ε) with the subsequent compression tests (Table 3). It was found that both values for the AMg2—10%TiC composite are slightly lower than the original matrix alloy values. For AMg6—10%TiC the decrease is more significant. This is probably due to the extensive formation of the β-phase in the AMg6 alloy. The accumulation of clusters is more difficult to prevent. Furthermore, magnesium, as a highly active metal, can form compounds with oxygen. At low Mg content, $MgAl_2O_4$ is formed, and at high content, MgO [33].

Rafalsky I. et al. [34] studied the effects of adding 2 wt.% Mg on the structure of Al—1%Ti—10%SiC

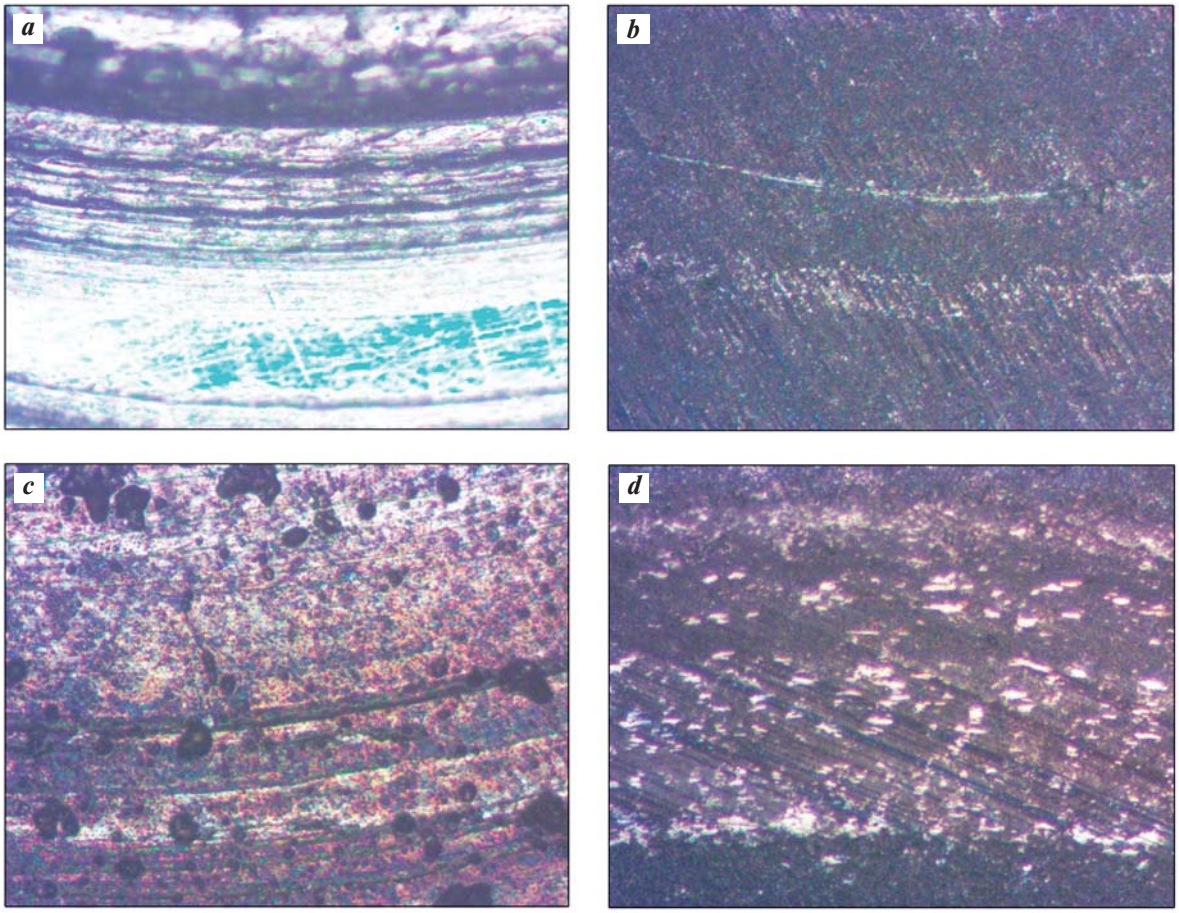

Fig. 15. Friction surface of the AMCs samples
a – AMg2N; ***b*** – AMg2–10%TiC (heating to 150 °C, 3 h); ***c*** – AMg6N; ***d*** – AMg6–10%TiC (heating to 230 °C, 3 h)

Рис. 15. Вид поверхности трения образцов АМКМ
a – АМг2Н; ***b*** – АМг2–10%TiC (нагрев до 150 °C, 3 ч); ***c*** – АМг6Н; ***d*** – АМг6–10%TiC (нагрев до 230 °C, 3 ч)

Table 5. **Tribological tests**

Таблица 5. Результаты сравнительных триботехнических испытаний

Sample composition	Wear rate, μm/h	Friction coefficient	Self-heating temperature, °C
AMg2N	37.6±5.2	up to 0.3	71
AMg2–10%TiC (no HT)	6.4±1.6	0.11–0.12	65
AMg2–10%TiC (heating to 150 °C, 2 h)	4.0±1.3	0.07–0.08	56
AMg6N	15.5±4.1	0.13–0.15	70
AMg6–10%TiC (no HT)	3.5±0.6	0.07–0.09	59
AMg6–10%TiC (heating to 230 °C, 3 h)	4.2±1.2	0.08–0.10	66

composite manufactured by mixing at 850—900 °C. The final material contains individual, extended film-like clusters of $MgAl_2O_4$. The presence of Mg-containing inclusions at the phase interfaces can minimize the effect of higher wettability, and contribute to strength reduction. Mikheev R. et al. [35] also showed that by adding 10 wt.% of TiC 40—100 μm reinforcing particles to the AK12M2MgN, the aluminum alloy decreases compressive strength from 489 to 470 MPa, while the relative strain drops from 17.01 to 12.65 %. Therefore, an insignificant decrease in these properties is expected in composites reinforced with titanium carbide. Furthermore, the hardness values of AMg2—10%TiC and AMg6—10%TiC increase by 12 and 17 %, and the microhardness values increase by 18 and 7 %, respectively.

During the upsetting test (Table 3), we loaded the samples to the maximum. The samples of AMg2 and AMg6 matrix alloys were deformed by 32 and 44 % without cracking. The test was stopped upon cracking. The cracks always occurred not in the sample body, but on its circumference. It was found that the AMCs after heating have better strain and reduction ratio values than the original alloys. These values are almost identical to the matrix alloy values. The ε = 29 and 43 % measured values are assumed to be the strain limits for the AMCs samples. This is a satisfactory result, since in real-life applications magnalium alloys are not subjected to strains exceeding 30 % which leads to a decrease in the plasticity. It can also create instability of mechanical and corrosion resistance properties [26].

High corrosion resistance is one of the key advantages of magnalium alloys. After annealing, the corrosion resistance is 3 points (Perelygin Yu. et al. [36]). We also measured this property (Table 4). All the AMCs samples have a corrosion depth rate of 0.001—0.005 mm/year. It matches that of the matrix alloys and means that the AMCs are highly resistant.

Finally, we compared the tribological properties of the investigated materials. The samples of the original AMg2 matrix alloy showed wear with seizures and abrasive wear. It leads to rapid destruction of the surface layer. The AMg6 sample featured unstable friction torque values, indicating undesirable effects in the friction contact area (Fig. 15, *a*, *b*).

All the AMCs samples showed better tribological properties such as good mechanical conformability, halving the friction coefficient, and up to 88 % wear rate reduction (Fig. 15, *c*, *d* and Table 5).

Conclusion

This study showed that heat treatment of composites based on aluminum-magnesium matrix alloys reinforced with ultra-fine titanium carbide is a promising method of controlling the composite structure and properties, although the original matrix alloys are not-heat-treatable.

It was found that SHS of the AMg2—10%TiC composite with subsequent heating to 150 °C maintains compressive strength, deformability, and corrosion resistance (virtually identical to the original hardened matrix alloy values). Furthermore, hardness is increased by 12 %, and microhardness by 18 %. The friction coefficient is reduced by at least 75 %, and the wear rate by 88 %.

It was found that SHS of the AMg6—10%TiC composite with subsequent heating to 230 °C reduces compressive strength by 12 %, while deformability and corrosion resistance are still acceptable. Hardness is increased by 17 %, and microhardness by 7 %. The friction coefficient is halved and the wear rate is reduced by 72 %.

The liquid matrix SHS process with subsequent heat treatment of aluminum-magnesium alloy composites hardened with ultra-fine titanium carbide can produce light and wear-resistant materials.

References

1. Mikheyev R.S., Chernyshova T.A. Aluminum-matrix composite materials with carbide hardening for solving problems of new technology. Moscow: RFFI, 2013. 353 p. (In Russ.).
   Михеев Р.С., Чернышова Т.А. Алюмоматричные композиционные материалы с карбидным упрочнением для решения задач новой техники. М.: Издание РФФИ, 2013. 353 с.
2. Sethi V. Effect of aging on abrasive wear resistance of silicon carbide particulate reinforced aluminum matrix composite. USA: University of Cincinnaty, 2007. 114 p.
3. Panfilov A.A., Prusov E.S., Kechin V.A. Problems and prospects for the development of production and application of aluminum matrix composite alloys. *Trudy Nizhegorodskogo gosudarstvennogo tekhnicheskogo universiteta imeni R.Ye. Alekseyeva*. 2013;2(99):210—217. (In Russ.).

Панфилов А.А., Прусов Е.С., Кечин В.А. Проблемы и перспективы развития производства и применения алюмоматричных композиционных сплавов. *Труды Нижегородского государственного технического университета им. Р.Е. Алексеева*. 2013; 2(99):210—217.

4. Nath H., Amosov A.P. SHS amidst other new processes for in-situ synthesis of Al-matrix composites: A review. *International Journal of Self-Propagating High-Temperature Synthesis*. 2016;(25):50—58. http://doi.org/10.3103/S106138621601009X
5. Amosov A.P., Luts A.R., Latukhin E.I., Ermoshkin A.A. Application of SHS processes for in situ production of aluminum-matrix composite materials discretely reinforced with nanoscale titanium carbide particles: Overview. *Russian Journal of Non-Ferrous Metals*. 2016;57(2):106—112. http://doi.org/10.3103/S1067821216020024
   Амосов А.П., Луц А.Р., Латухин Е.И., Ермошкин А.А. Применение процессов СВС для получения *in situ* алюмоматричных композиционных материалов, дискретно армированных наноразмерными частицами карбида титана: Обзор. *Известия вузов. Цветная металлургия*. 2016;(1):39—49. http://doi.org/10.17073/0021-3438-2016-1-39-49
6. Pramod S.L., Bakshi S.R., Murty B.S. Aluminum-based cast in situ composites: A review. *Journal of Materials Engineering and Performance*. 2015;24(6):2185—2207. http://doi.org/10.1007/s11665-015-1424-2
7. Pandey U., Purohit R., Agarwal P., Dhakad S.K., Rana R.S. Effect of TiC particles on the mechanical properties of aluminium alloy metal matrix composites (MMCs). *Materials Today: Proceedings*. 2017;4:5452—5460. http://doi.org/10.1016/j.matpr.2017.05.057
8. Chaubey A.K., Prashanth K.G., Ray N., Wang Z. Study on in-situ synthesis of Al—TiC composite by self — propagating high temperature synthesis process. *Materials Science: An Indian Journal*. 2015;12(12): 454—461.
9. Zhou D., Qiu F., Jiang Q. The nano-sized TiC particle reinforced Al—Cu matrix composite with superior tensile ductility. *Materials Science and Engineering:A*. 2015;622:189—193. http://doi.org/10.1016/j.msea.2014.11.006
10. Tian W.S., Zhao Q.L., Zhao C.J., Qiu F., Jiang Q.C. The dry sliding wear properties of nano-sized TiCp/Al—Cu composites at elevated temperatures. *Materials*. 2017;10:939. http://doi.org/10.3390/ma10080939
11. Luts A.R., Amosov A.P., Ermoshkin A.A., Ermoshkin A.A., Nikitin K.V., Timoshkin I.Y. Self-propagating high-temperature synthesis of highly dispersed titanium-carbide phase from powder mixtures in the aluminum melt. *Russian Journal of Non-Ferrous Metals*. 2014;55(6):606—612. http://doi.org/10.3103/S1067821214060169
    Луц А.Р., Амосов А.П., Ермошкин А.А., Ермошкин А.А., Никитин К.В., Тимошкин И.Ю. Самораспространяющийся высокотемпературный синтез высокодисперсной фазы карбида титана из смесей порошков в расплаве алюминия. Известия вузов. *Порошковая металлургия и функциональные покрытия*. 2013;(3):28—35.
12. Luts A.R., Amosov A.P., Latukhin E.I., Rybakov A.D., Novikov V.A., Shipilov S.I. Self-propagating high-temperature synthesis of (Al—2% Mn)—10% TiC and (Al—5% Cu—2% Mn)—10% TiC nanostructured composite alloys doped with manganese powder. *Russian Journal of Non-Ferrous Metals*. 2019;60(4):413—421. http://doi.org/10.3103/S1067821219040072
    Луц А.Р., Амосов А.П., Латухин Е.И., Рыбаков А.Д., Новиков В.А., Шипилов С.И. Самораспространяющийся высокотемпературный синтез наноструктурных композиционных сплавов (Al—2%Mn)—10%TiC и (Al—5%Cu—2%Mn)—10%TiC при легировании порошковым марганцем. *Известия вузов. Порошковая металлургия и функциональные покрытия*. 2018;(3):30—40. http://doi.org/10.17073/1997-308X-2018-3-30-40
13. Sai Chaitanya Kishore D., Prahlada Rao K., Mahamani A. Investigation of cutting force, surface roughness and flank wear in turning of in situ Al6061—TiC metal matrix composite. *Procedia Materials Science*. 2014;6:1040—1050. http://doi.org/10.1016/j.mspro.2014.07.175
14. Kareem A., Qudeiri J.A., Abdudeen A., Ahammed T., Ziout A. A review on AA 6061 metal matrix composites produced by stir casting. *Materials*. 2021;14(1):175. http://doi.org/10.3390/ma14010175
15. Krishna Prasad S., Dayanand S., Rajesh M., Nagaral M., Auradi V., Selvaraj R. Preparation and mechanical characterization of TiC particles reinforced Al7075 alloy. *Advances in Materials Science and Engineering*. 2022;1:1—11. http://doi.org/10.1155/2022/7105189
16. Cho Y.H., Lee J.M., Kim S.H. Al—TiC Composites fabricated by a thermally activated reaction process in an al melt using Al—Ti—C—CuO powder mixtures:

Pt. II. Microstructure control and mechanical properties. *Metallurgical & Materials Transaction*s. 2015;46A:1374—1384. http://doi.org/10.1007/s11661-014-2476-x

17. Ramakoteswara Rao V., Ramanaiah N., Sarcar M.M. Mechanical and tribological properties of AA7075—TiC metal matrix composites under heat treatment (T6) and cast conditions. *Journal of Materials Research and Technology*. 2016;5(4):377—383. http://doi.org/10.1016/j.jmrt.2016.03.011
18. Ramakoteswara Rao V., Ramanaiah N., Sarcar M.M. Dry sliding wear behavior of Al7075 reinforced with titanium carbide (TiC) particulate composites. In: *Proceedings of Int. Conf. on Advances in Materials, Manufacturing and Applications (AMMA 2015)* (2015, April 9—11). P. 39—44. URL: https://www.researchgate.net/publication/279868886_Dry_Sliding_Wear_Behavior_of_Al7075_Reinforced_with_Titanium_Carbide_TiC_Particulate_Composites (accessed: 21.03.2023).
19. Chen C.L., Lin C.H. A Study on the aging behavior of Al6061 composites reinforced with Y_2O_3 and TiC. *Metals*. 2017;7 (11):7—11. http://doi.org/10.3390/met7010011
20. Kurbatkina E.I., Shavnev A.A., Kosolapov D.V., Gololobov A.V. Features of thermal treatment of composite materials with aluminum matrix (Review). *Trudy VIAM*. 2017;11:82—97. URL: http://viam-works.ru/ru/articles?year=2017&num=11 (accessed: 21.03.2023). (In Russ.). http://dx.doi.org/ 10.18577/2307-6046-2017-0-11-9-9
Курбаткина Е.И., Шавнев А.А., Косолапов Д.В., Гололобов А.В. Особенности термической обработки композиционных материалов с алюминиевой матрицей (обзор). *Труды ВИАМ*. 2017;11:82—97. URL: http://viam-works.ru/ru/articles?year=2017&num=11 (дата обращения: 21.03.2023). http://dx.doi.org/ 10.18577/2307-6046-2017-0-11-9-9
21. Kurganova Y.A. Development and applications of dispersion strengthened aluminum matrix composite materials in mechanical engineering: Abstract of dissertation of Dr. Sci. (Eng.). Moscow: IMET RAS, 2008. (In Russ.).
Курганова Ю.А. Разработка и применение дисперсно-упрочненных алюмоматричных композиционных материалов в машиностроении: Автореф. дис. ... д.т.н. М.: ИМЕТ РАН, 2008.
22. Hashim J. The production of cast metal matrix composite by a modified stir casting method. *Jurnal Teknologi*. 2001;35(1):9—20. http:// doi.org/10.11113/jt.v35.588
23. Contreras A., Angeles-Chávez C., Flores O., Perez R. Structural, morphological and interfacial characterization of Al—Mg/TiC composites. *Materials Characterization*. 2007;58:685—693. http://doi.org/10.1016/j.matchar.2006.11.031
24. Shu S., Lu J, Qiu F., Xuan Q., Jiang Q. Effects of alloy elements (Mg, Zn, Sn) on the microstructures and compression properties of high-volume-fraction TiC_x/Al composites. *Scripta Materialia*. 2010;63:1209—1211. http://doi.org/10.1016/j.scriptamat.2010.08.040
25. Gulyayev A.P. Metallovedeniye. Moscow: Metallurgiya, 1986. 544 p. (In Russ.).
Гуляев А.П. Металловедение. М.: Металлургия, 1986. 544 с.
26. Kolachev B.A., Elagin V.I., Livanov V.A. Metal science and heat treatment of non-ferrous metals and alloys. Moscow: MISIS, 2001. 433 p. (In Russ.).
Колачев Б.А., Елагин М.И., Ливанов В.А. Металловедение и термическая обработка цветных металлов и сплавов. М.: МИСИС, 2001. 433 с.
27. Arzamasov B.N., Sidorin I.I., Kosolapov G.F., Makarova V.I., Mukhin G.G., Ryzhov N.M., Silaeva V.I., Ulyanova N.V. Material science. Moscow: Mashinostroenie, 1986. 384 p. (In Russ.).
Арзамасов Б.Н., Сидорин И.И., Косолапов Г.Ф., Макарова В.И., Мухин Г.Г., Рыжов Н.М., Силаева В.И., Ульянова Н.В. Материаловедение. М.: Машиностроение, 1986. 384 с.
28. Lyakishev N.P. (Ed.). State diagrams of binary metallic systems: Reference book. In 3 volumes. Vol. 2. Moscow: Mashinostroenie, 1996. 498 p. (In Russ.).
Диаграммы состояния двойных металлических систем: Справочник. В 3 т. Т. 2. Под общ. ред. Н.П. Лякишева. М.: Машиностроение, 1996. 498 с.
29. Belov N.A. Phase composition of aluminum alloys. Moscow: MISIS, 2009. 234 p. (In Russ.).
Белов Н.А. Фазовый состав алюминиевых сплавов. М.: МИСИС, 2009. 234 с.
30. Kishchik M.S. Formation of a micrograin structure in aluminum alloy 1565ch by thermal and thermomechanical treatment: Abstract of the dissertation of Cand. Sci (Eng.). Moscow: MISIS, 2019. (In Russ.).
Кищик М.С. Формирование микрозеренной структуры в алюминиевом сплаве 1565ч путем термической и термомеханической обработки: Автореф. дис. ... к.т.н. М.: МИСИС, 2019.
31. Pan S., Wang T., Jin K., Cai X. Understanding and

designing metal matrix nanocomposites with high electrical conductivity: A review. *Journal Materials Science*. 2022;57:6487—6523.
http://doi.org/10.1007/s10853-022-07010-4

32. Pan S., Yuan J., Zheng T., She Z., Li X. Interfacial thermal conductance of in situ aluminummatrix nanocomposites. *Journals Materials Science*. 2021;56:13646—13658.
http://doi.org/10.1007/s10853-021-06176-7
33. Mikheev R.S., Chernyshova T.A. Discretely reinforced composite materials of the Al—TiC system (review). *Zagotovitelnye proizvodstva v mashinostroenii*. 2008; (11):44—53. (In Russ.).
Михеев Р.С., Чернышова Т.А. Дискретно армированные композиционные материалы системы Al—TiC (обзор). *Заготовительные производства в машиностроении*. 2008;11:44—53.
34. Rafalsky I.V. Resource-saving synthesis of aluminum-based alloys using dispersed non-metallic materials and intelligent methods for controlling metallurgical processes for their production. Minsk: BNTU, 2016. 309 p. (In Russ.).
Рафальский И.В. Ресурсосберегающий синтез сплавов на основе алюминия с использованием дисперсных неметаллических материалов и интеллектуальные методы контроля металлургических процессов их получения. Минск: БНТУ, 2016. 309 с.
35. Mikheev R.S. Promising coatings with improved tribotechnical characteristics from composite materials based on non-ferrous alloys. Abstract of the dissertation of Dr. Sci. (Eng.). Moscow: IMET RAS, 2018. (In Russ.).
Михеев Р.С. Перспективные покрытия с повышенными триботехническими характеристиками из композиционных материалов на основе цветных сплавов: Автореф. дис....д.т.н. М.: ИМЕТ РАН, 2018.
36. Perelygin Yu. P., Los I. S., Kireev Yu. S. Corrosion and protection of metals from corrosion. Penza: PGU, 2015. 88 p. URL: https://elib.pnzgu.ru/files/eb/u36mWX4yGz0I.pdf (accessed: 21.03.2023). (In Russ).
Перелыгин Ю. П., Лось И.С., Киреев С.Ю. Коррозия и защита металлов от коррозии. Пенза: Изд-во ПГУ, 2015. 88 с. URL: https://elib.pnzgu.ru/files/eb/u36mWX4yGz0I.pdf (дата обращения: 21.03.2023). (In Russ.).

Information about the authors

Alfiya R. Luts – Cand. Sci. (Eng.), Assistent Prof., Department of Metal Science, Powder Metallurgy, Nanomaterials (MPMN), Samara State Technical University (SamSTU).
http://orcid.org/0000-0001-7889-9931
E-mail: alya_luts@mail.ru

Yuliya V. Sherina – Post-graduate Student, Department of MPMN, SamSTU.
http://orcid.org/0000-0002-5451-7107
E-mail: yulya.makhonina.97@inbox.ru

Alexander P. Amosov – Dr. Sci. (Phys.-Math.), Head of the Department of MPMN, SamSTU.
http://orcid.org/0000-0003-1994-5672
E-mail: egundor@yandex.ru

Andrey D. Kachura – Master's Student, Department of MPMN, SamSTU.
http://orcid.org/0000-0001-9246-5638
E-mail: ruw223@mail.ru

Информация об авторах

Альфия Расимовна Луц – к.т.н., доцент кафедры металловедения, порошковой металлургии, наноматериалов (МПМН), Самарский государственный технический университет (СамГТУ).
http://orcid.org/0000-0001-7889-9931
E-mail: alya_luts@mail.ru

Юлия Владимировна Шерина – аспирант кафедры МПМН, СамГТУ.
http://orcid.org/0000-0002-5451-7107
E-mail: yulya.makhonina.97@inbox.ru

Александр Петрович Амосов – д.ф.-м.н., профессор, зав. кафедрой МПМН, СамГТУ.
http://orcid.org/0000-0003-1994-5672
E-mail: egundor@yandex.ru

Андрей Дмитриевич Качура – магистр кафедры МПМН, СамГТУ.
http://orcid.org/0000-0001-9246-5638
E-mail: ruw223@mail.ru

Contribution of the authors

A.R. Luts – concept, problem statement, analysis of the test results, paper authoring.

Yu.V. Sherina – heat treatment and testing of the samples, analysis of the test results, paper authoring.

A.P. Amosov – supervision, paper proofreading, conclusions editing.

A.D. Kachura – sample manufacturing, microstructural analysis, conclusions.

Вклад авторов

А.Р. Луц – формирование основной концепции, постановка цели и задачи исследования, анализ результатов, подготовка текста статьи.

Ю.В. Шерина – проведение термической обработки и испытаний образцов, анализ результатов, подготовка текста статьи.

А.П. Амосов – научное руководство, корректировка текста, корректировка выводов.

А.Д. Качура – синтез литых образцов, микроструктурный анализ, формулировка выводов.

The article was submitted 16.03.2023, revised 08.06.2023, accepted for publication 16.06.2023

Статья поступила в редакцию 16.03.2023, доработана 08.06.2023, подписана в печать 16.06.2023